Acidification and CO_2-Driven Conditions in the Estuary and Gulf of St. Lawrence During 2024

Martine Lizotte[1], Marjolaine Blais[1], Joël Chassé[2], Peter S. Galbraith[1], Anne-Josée Hébert[1], and Michel Starr[1]

[1]Regional Sciences Branch, Quebec region
Pelagic and Ecosystemic Sciences Division
Fisheries and Oceans Canada
Maurice Lamontagne Institute
850, Route de la Mer
Mont-Joli, QC
G5H 3Z4

[2]Regional Sciences Branch, Gulf region
Gulf Fisheries Centre
Fisheries and Oceans Canada
P.O. Box 5030
Moncton, NB
E1C 9B6

2026

Canadian Technical Report of
Hydrography and Ocean Sciences 410

Fisheries and Oceans Canada | Pêches et Océans Canada

Canada

Canadian Technical Report of Hydrography and Ocean Sciences

Technical reports contain scientific and technical information of a type that represents a contribution to existing knowledge but which is not normally found in the primary literature. The subject matter is generally related to programs and interests of the Oceans and Science sectors of Fisheries and Oceans Canada.

Technical reports may be cited as full publications. The correct citation appears above the abstract of each report. Each report is abstracted in the data base *Aquatic Sciences and Fisheries Abstracts.*

Technical reports are produced regionally but are numbered nationally. Requests for individual reports will be filled by the issuing establishment listed on the front cover and title page.

Regional and headquarters establishments of Ocean Science and Surveys ceased publication of their various report series as of December 1981. A complete listing of these publications and the last number issued under each title are published in the *Canadian Journal of Fisheries and Aquatic Sciences*, Volume 38: Index to Publications 1981. The current series began with Report Number 1 in January 1982.

Rapport technique canadien sur l'hydrographie et les sciences océaniques

Les rapports techniques contiennent des renseignements scientifiques et techniques qui constituent une contribution aux connaissances actuelles mais que l'on ne trouve pas normalement dans les revues scientifiques. Le sujet est généralement rattaché aux programmes et intérêts des secteurs des Océans et des Sciences de Pêches et Océans Canada.

Les rapports techniques peuvent être cités comme des publications à part entière. Le titre exact figure au-dessus du résumé de chaque rapport. Les rapports techniques sont résumés dans la base de données *Résumés des sciences aquatiques et halieutiques*.

Les rapports techniques sont produits à l'échelon régional, mais numérotés à l'échelon national. Les demandes de rapports seront satisfaites par l'établissement auteur dont le nom figure sur la couverture et la page de titre.

Les établissements de l’ancien secteur des Sciences et Levés océaniques dans les régions et à l'administration centrale ont cessé de publier leurs diverses séries de rapports en décembre 1981. Vous trouverez dans l'index des publications du volume 38 du *Journal canadien des sciences halieutiques et aquatiques*, la liste de ces publications ainsi que le dernier numéro paru dans chaque catégorie. La nouvelle série a commencé avec la publication du rapport numéro 1 en janvier 1982.

Canadian Technical Report
of Hydrography and Ocean Sciences 410

2026

Acidification and CO_2-Driven Conditions in the Estuary and Gulf of St. Lawrence During 2024

[1]Martine Lizotte, [1]Marjolaine Blais, [2]Joël Chassé, [1]Peter S. Galbraith, [1]Anne-Josée Hébert, and [1]Michel Starr

[1]Regional Sciences Branch
Quebec region
Pelagic and Ecosystemic Sciences Division
Fisheries and Oceans Canada
Maurice Lamontagne Institute
850, Route de la Mer
Mont-Joli, QC
G5H 3Z4

[2]Regional Sciences Branch
Gulf region
Gulf Fisheries Centre
Fisheries and Oceans Canada
P.O. Box 5030
Moncton, NB
E1C 9B6

Cat. No. Fs 97-18/410E-PDF ISBN 978-0-660-97987-8 ISSN 1488-5417
https://doi.org/10.60825/rj0q-3t94

Correct citation for this publication:

Lizotte, M., Blais, M., Chassé, J., Galbraith, P. S., Hébert, A.-J., Starr, M. 2026. Acidification and CO_2-Driven Conditions in the Estuary and Gulf of St. Lawrence During 2024. Can. Tech. Rep. Hydrogr. Ocean. Sci. 410 : vi + 71 p. https://doi.org/10.60825/rj0q-3t94

TABLE OF CONTENTS

ABSTRACT

Lizotte, M., Blais, M., Chassé, J., Galbraith, P. S., Hébert, A.-J., Starr, M. 2026. Acidification and CO_2-Driven Conditions in the Estuary and Gulf of St. Lawrence During 2024. Can. Tech. Rep. Hydrogr. Ocean. Sci. 410 : vi + 71 p. https://doi.org/10.60825/rj0q-3t94

This report presents an overview of marine acidification and CO_2-driven conditions in the Estuary and Gulf of St. Lawrence for 2024, based on data collected through the Atlantic Zone Monitoring Program and the Aquatic Climate Change Adaptation Services Program, led by Fisheries and Oceans Canada. Regional observations are compared against climatological means to assess anomalies and trends of the carbonate system. In 2024, key indicators, including pH_T, the carbonate system vulnerability index (CSVI), partial pressure of CO_2 (pCO_2), saturation states of aragonite (Ω_A) and calcite (Ω_C), and the substrate-inhibitor ratio (SIR), reveal widespread and depth-dependent stressor patterns across the region. From 2020 and continuing into 2024, the 200 m depth horizon stands out as a zone of sustained vulnerability, with multiple indicators exceeding established stress thresholds and record-setting anomalies in several regions. Hypercapnia is observed at this depth in all deep regions except the Centre Gulf, indicating elevated CO_2 levels that may impair physiological function in marine organisms. The upward shoaling of proxies for calcium carbonate formation (SIR) and dissolution (Ω_A and Ω_C) may compress optimal habitat for calcifiers, with the Northwest Gulf and the Estuary emerging as hotspots of reduced buffering capacity and heightened sensitivity to CO_2-driven conditions.

RÉSUMÉ

Lizotte, M., Blais, M., Chassé, J., Galbraith, P. S., Hébert, A.-J., Starr, M. 2026. Acidification and CO_2-Driven Conditions in the Estuary and Gulf of St. Lawrence During 2024. Can. Tech. Rep. Hydrogr. Ocean. Sci. 410 : vi + 71 p. https://doi.org/10.60825/rj0q-3t94

Ce rapport présente un aperçu des conditions liées à l'acidification marine et à l'accumulation de CO_2 dans l'estuaire et le golfe du Saint-Laurent pour l'année 2024, à partir de données recueillies dans le cadre du Programme de monitorage de la zone atlantique et du Programme de services d'adaptation aux changements climatiques aquatiques, menés par Pêches et Océans Canada. Les observations régionales sont comparées aux moyennes climatologiques afin d'évaluer les anomalies et les tendances du système des carbonates. En 2024, les indicateurs, incluant le pH_T, l'indice de vulnérabilité du système des carbonates (CSVI), la pression partielle de CO_2 (pCO_2), les états de saturation de l'aragonite (Ω_A) et de la calcite (Ω_C), ainsi que le ratio substrat-inhibiteur (SIR), révèlent des patrons de stress dépendants de la profondeur dans l'ensemble de la région. Depuis 2020 et jusqu'en 2024, l'horizon de 200 m de profondeur se distingue comme une zone de vulnérabilité persistante, avec des dépassements de plusieurs seuils de stress et des anomalies records dans plusieurs sous-régions. Des conditions hypercapniques sont observées à cette profondeur dans toutes les régions profondes, à l'exception du centre du golfe, indiquant des niveaux élevés de CO_2 susceptibles d'affecter les fonctions physiologiques des organismes marins. La remontée verticale des seuils d'indicateurs de formation (SIR) et de dissolution (Ω_A et Ω_C) du carbonate de calcium pourrait comprimer l'habitat optimal des organismes calcifiants, tandis que les gradients régionaux mettent en évidence le nord-ouest du golfe et l'estuaire comme des zones critiques à faible capacité tampon et à sensibilité accrue aux conditions associées à l'accumulation de CO_2.

1. INTRODUCTION

The acidification of seawater, commonly referred to as “ocean acidification” (OA), is a well-documented consequence of the accumulation of anthropogenic carbon dioxide (CO_2) in the atmosphere (Caldeira and Wickett 2003, Gattuso and Hansson 2020). Rising CO_2 levels lower surface seawater pH, which has declined by about 0.002 units annually across much of the global open ocean since the 1980s, with only minor decadal fluctuations (Doney et al. 2009, Bates et al. 2014, Lauvset et al. 2015). Although seemingly modest, this decline is part of a long-term trend in which seawater acidity is increasing at a rate 10 times faster than during any period of the past 300 million years (Hönisch et al. 2012). Overall, global ocean acidity has risen by roughly 40% since the pre-industrial Holocene epoch, reflecting a seemingly small pH drop, from ~8.18 (pre-industrial) to 8.04 (in 2024), that has significant consequences on global ocean chemistry (EEA 2024, NOAA 2024). Recently, OA has been formally recognized as a transgressed planetary boundary (Findlay et al. 2025, Sakschewski et al. 2025) underscoring its significance as a threat to Earth system stability.

Unlike the steady pH decline at the surface of the open ocean, pH conditions in estuarine, coastal, nearshore and marginal sea systems show complex trends driven by local and regional processes (Cai et al. 2021, Hall et al. 2023, Li et al. 2025). Changes vary with depth, with some areas acidifying while others become more alkaline (Carstensen and Duarte 2019). In these environments, variability in pH may reflect not only atmospheric CO_2 uptake (Caldeira and Wickett 2003) but also the combined influence of external inputs, such as nutrient enrichment, watershed weathering, river discharge, and groundwater flow, as well as internal processes including water mass mixing, organic matter cycling, carbonate mineral reactions, and seasonal ice dynamics (Gruber et al. 2019, Chen et al. 2023, Middelburg et al. 2020, Cai et al. 2021). In many regions, the downward transport of anthropogenic inorganic carbon, combined with intensified respiration-driven metabolic carbon accumulation, leads to a faster rate of acidification below the pycnocline than in surface waters, a phenomenon termed “enhanced ocean acidification” (Cai et al. 2011, Lauvset et al. 2020, Fassbender et al. 2023, Findlay et al. 2025).

Anthropogenic and metabolic CO_2 interact with seawater to alter the carbonate system, changing the partial pressure of carbon dioxide (pCO_2), and concentrations of bicarbonate [HCO_3^-], carbonate [CO_3^{2-}], and hydrogen [H^+] ions (Doney et al. 2020). These shifts may affect organism physiology, growth, calcification, and reproduction by disturbing the organism’s acid–base regulation and energy budget (Stumpp et al. 2012, Dixson et al. 2015, Melzner et al. 2020, Figuerola et al. 2021, Leung et al. 2022, Padilla-Gamino et al. 2022, Shi and Li 2024). Declining saturation states for calcite (Ω_C) and aragonite (Ω_A) increase the energetic cost of maintaining calcium carbonate structures for calcifying organisms including coccolithophores, foraminifera, pteropods, mollusks, crustaceans, echinoderms, and corals (Fabry et al. 2008, Ries et al. 2009, Kroeker et al. 2010, Jokiel 2011, Thomsen et al. 2015, Clements and Hunt 2015, Toyofuku et al. 2017, Pousse et al. 2020). Increasing exposure to water masses with pCO_2 >1000 µatm, a condition termed “ocean hypercapnia”, may further impair respiration and acid–base regulation, with demonstrated consequences for behavior and neural function (Perry and Gilmour 2006, Nilsson et al. 2012, McNeil and Sasse 2016, Pimentel et al. 2016, Feely et al. 2018). Developing a thorough understanding of the carbonate system in Canadian waters is thus fundamental for guiding ecosystem-based fisheries management and climate vulnerability assessments.

Systematic measurements of OA parameters in the Estuary and Gulf of St. Lawrence (EGSL) have been ongoing since fall 2014 as part of the Atlantic Zone Monitoring Program (AZMP, see Therriault et al. 1998) and the Aquatic Climate Change Adaptation Services Program (ACCASP) of Fisheries and Oceans Canada (DFO) (Gibb et al. 2023, Blais et al. 2024, Galbraith et al. 2024, Galbraith et al. 2025a). Although some historical data on acidification in the Atlantic Zone exists (e.g., Mucci et al. 2011), DFO programs have provided continuous and detailed monitoring, building on the foundation of these earlier, more sporadic measurements. This fundamentally important monitoring has strengthened DFO's capacity to characterize and forecast marine ecosystem conditions, quantify climate-related changes, and identify emerging vulnerabilities. This document outlines chemical conditions associated with multifaceted CO_2-driven conditions in the EGSL, with a focus on the spatiotemporal variability of several key CO_2-carbonate system indices. The chemical environment of this dynamic estuarine and semi-enclosed sea reflects the complex interplay of physical and biological processes. For a comprehensive description of the 2024 physical and biogeochemical conditions in the EGSL, readers should consult Galbraith et al. (2025b) and Blais et al. (2025), respectively.

2. METHODS

2.1 SAMPLING

To ensure the highest standards of data quality, all sampling and processing procedures followed the Guide to Best Practices for Ocean CO_2 Measurements (Dickson et al. 2007), and the AZMP protocols (Mitchell et al. 2002). The field measurements presented in this report were gathered during dedicated AZMP surveys conducted in early summer and fall each year, as well as at one high-frequency monitoring station (Figure 1, and Table 1). Additional oceanographic data from multidisciplinary surveys, typically carried out in summer (Chamberland et al. 2025), and from the mackerel egg survey were included for all years (2014–2024) for which these data are available (Table 1). In this document, sampling stations were grouped into five main regions for which carbonate system indices are presented (Figure 1):

- Estuary: The lower St. Lawrence Estuary is a transitional zone where freshwater from the St. Lawrence River mixes with incoming marine waters. Circulation and mixing in this region are also shaped, among other factors, by tidal dynamics, winds and bathymetric features. A defining characteristic of the zone is the Laurentian Channel, a submerged valley that typically reaches depths exceeding 200 meters.

- Northwest Gulf: This area is typically deep (over 200 m). It is heavily influenced by freshwater runoff from the St. Lawrence River at the surface, and by dense waters flowing along the Laurentian Channel at greater depths.

- Centre Gulf and Cabot Strait: Generally deep (over 200 m), this region is directly affected by deep water mixing at the continental slope. It receives a mixture of warm North Atlantic Central Water (NACW) with a Gulf Stream signature and cold Labrador Current water (LCW) through Cabot Strait. For the sake of brevity, this region is referenced as Centre Gulf throughout the text.

- Northeast Gulf: Characterized by deep channels and a relatively wide shelf (less than 100 m deep), this region has high surface salinity. It encompasses the Anticosti and Esquiman subregions.

- Magdalen Shallows: This shallow region (~100 m and less) is typically warm at the surface during summer and is significantly influenced by the Gaspé Current. Chaleur Bay is included within this region.

These regional designations are consistent with those used in DFO's Ecosystem Approach to Fisheries and Management for the Gulf of St. Lawrence. Due to limited chemical data availability in Mécatina Trough, and Northumberland Strait (Figure 1), acidification indices are not included in the annual scorecards but are still visible on the spatial maps.

Details about the 2024 sampling surveys are provided in Table 1, while Figures 1 and 2 summarize the sampling effort during the seasonal surveys and at the high-frequency monitoring station, respectively. Rimouski Station (depth 320 m) is a high-frequency monitoring station and has been sampled for CO_2-carbonate system parameters since 2014. Sampling at this station occurs approximately weekly during the summer, once or twice a month from early spring to late fall, and rarely in winter (except during the AZMP wintertime survey of the Gulf of St. Lawrence water (Galbraith 2006), but no acidification parameters are measured then) due to the presence of sea ice. It is representative of the conditions in the Estuary. In 2024, Rimouski Station was visited on 22 occasions that included the collection of carbonate system parameters.

Sampling along the oceanographic sections and at the high-frequency monitoring station includes a Conductivity-Temperature-Depth profile (CTD; temperature, salinity, fluorescence, dissolved oxygen) and water collection using Niskin bottles (2 m, 10 m, 15 m, 25 m, 50 m, 100 m, 200 m, 300 m, 400 m, bottom). In this report, the term "surface" refers to the uppermost sampled layer (top 10 m). Water collected from Niskin bottles is typically analyzed for seawater pH on the total scale (pH_T), total alkalinity (TA), and dissolved inorganic carbon (DIC). From these measurements, key ocean acidification metrics, including calcium carbonate saturation states for calcite (Ω_C) and aragonite (Ω_A), partial pressure of carbon dioxide (pCO_2), and substrate-inhibitor ratio (SIR), are derived using TA–pH_T pairs when available (see section 2.3.2 for further details). The carbonate system vulnerability index (CSVI), used to assess buffering capacity, is calculated from the difference between TA and DIC.

2.2 BACKGROUND ON CARBONATE CHEMISTRY METRICS

Total alkalinity, dissolved inorganic carbon, and carbonate system vulnerability index

Total alkalinity, expressed in µmol kg^{-1} of seawater, is operationally defined as the excess of proton acceptors over proton donors. Monitoring TA variability can provide insights on the seawater's buffering capacity against acidification. Higher TA levels generally indicate a greater capacity to neutralize acidity, which plays a critical role in maintaining stable pH conditions under rising concentrations of DIC from both anthropogenic and metabolic sources. It is important to note that this report does not distinguish between organic and inorganic contributions to TA, a known source of uncertainty in carbonate system assessments, particularly in coastal and high-dissolved organic matter (DOM) environments (Hu 2020, Kerr et al. 2021). Dissolved inorganic carbon, also expressed in µmol kg^{-1} of seawater, is the sum of all dissolved inorganic carbon species (aqueous [$CO_{2(aq)}$], carbonic acid [H_2CO_3], [HCO_3^-], and [CO_3^{2-}]). Monitoring DIC provides insights into carbon transport, storage, and transformation

across the EGSL and helps identify changes in freshwater inflows, nutrient loading, and organic matter decomposition, among other processes.

In this report, TA and DIC are presented as distinct parameters; however, we emphasize their differential ([TA] – [DIC]) as a combined diagnostic metric to better highlight areas of heightened carbonate system vulnerability. This framing supports a more integrated assessment of buffering capacity and acidification potential, particularly in regions subject to multiple interacting stressors. The difference between TA and DIC ([TA] – [DIC]), hereby referred to as the Carbonate System Vulnerability Index, is a fundamental quantity of ocean water (Xue and Cai 2020) and can be used as a simple baseline indicator of buffering capacity. When CSVI values are positive, TA exceeds DIC and buffering capacity is high. When TA and DIC approach equivalence ([TA] – [DIC] = 0), even small increases in CO_2 concentration can trigger disproportionately large declines in pH. At this critical juncture, the buffering capacity of the carbonate system becomes substantially weakened (Frankignoulle et al. 1994, Egleston et al. 2010), resulting in non-linear and amplified pH responses to incremental CO_2 inputs. Negative CSVI values, where DIC exceeds TA, may indicate reduced buffering capacity and enhanced vulnerability to acidification. These conditions often reflect zones of intense organic matter degradation and CO_2 accumulation (see examples in Martínez-Trejo et al. 2024). CSVI is favored over the [TA] / [DIC] ratio used elsewhere (e.g., Wang et al. 2013) because the [TA] – [DIC] difference behaves more conservatively under ocean mixing, is less affected by non-linear changes during mixing and variations in physical conditions, and more directly reflects biogeochemical influences on acidification. Consequently, CSVI provides a robust, interpretable and scalable metric for tracking OA processes across diverse marine environments (Xue and Cai 2020, Martínez-Trejo et al. 2024, Reimer et al. 2024).

Potential of hydrogen

The pH of seawater quantifies the activity of hydrogen ions and therefore its “acidity”, expressed on a logarithmic scale as $-\log_{10}([H^+])$ (Caldeira and Wickett 2003, Feely et al. 2004, Feely et al. 2008). In this report, terms such as “more acidic” or “acidification” are used to describe the trend of increasing acidity levels (increasing H^+). Oceanic waters are typically mildly alkaline with a pH > 7.0 (genuinely acidic conditions, referring to water with a pH < 7.0, are unlikely to be encountered in marine systems). Unless noted otherwise, pH values in this report are expressed on the total hydrogen-ion scale (pH_T). Exceptions include the substrate-inhibitor ratio (see section 3.4) which uses H^+ on the free scale.

Partial pressure of CO_2

Partial pressure of CO_2 refers to the portion of the total pressure exerted by CO_2 in a mixture of gases dissolved in seawater (Emerson and Hedges 2008). Over the global ocean, pCO_2 typically varies from about 100 µatm to 1000 µatm (1 µatm = 10^{-6} atm = 0.101325 Pascal) (Takahashi et al. 2017). However, hypercapnic conditions (pCO_2 > 1000 µatm) are observed in contemporary oceanic environments (Feely et al. 2018) and often co-occur with hypoxia (Arroyo et al. 2022). Subsurface remineralization inherently links high pCO_2 (hypercapnia), low pH (acidification), and low dissolved oxygen values (hypoxia), which can be intensified on continental shelves, estuarine and semi-enclosed oceanic environments by locally driven processes (Cai et al. 2011, Feely et al. 2016, Cai et al. 2017, Chan et al. 2017, Feely et al. 2018, Chan et al. 2019, Cai et al. 2021). While direct pCO_2 measurements are the most accurate means to characterize these conditions, pCO_2 estimates derived from other CO_2-carbonate system variables (pH_T and TA as used in this report) remain highly valuable, though they come with a higher degree of uncertainty, especially for depths below 100 m (Weiss 1974,

Orr et al. 2015). Seacarb is currently one of the few packages that compute ocean carbonate chemistry while accounting for hydrostatic pressure effects on pCO_2, potentially reducing some of the associated uncertainties (Orr et al. 2015, Gattuso et al. 2024).

Indices of calcium carbonate mineral formation and dissolution

The saturation state of $CaCO_3$ minerals (Ω_{CaCO_3}) is a dimensionless ratio that compares the concentration of dissolved calcium (Ca^{2+}) and CO_3^{2-} ions in seawater to their saturation concentrations. It is a fundamental metric of the thermodynamic potential of $CaCO_3$ dissolution: $\Omega < 1$ indicates that dissolution is favored (Morse et al. 2007). Biogenic $CaCO_3$ primarily exists as either calcite or aragonite, each with distinct crystal structures and solubilities (Mann 2001). Calcite is mainly produced by coccolithophores, foraminifera, and some crustaceans, whereas aragonite is typically found in scleractinian corals and pteropods. Mollusks can form both calcite and aragonite, and echinoderms form calcite that includes a significant amount of magnesium (Mg) within the crystal lattice (Mann 2001, Bach 2015). Because aragonite is more soluble than calcite (Mucci 1983), aragonite-secreting organisms, particularly those with unprotected $CaCO_3$ structures, are generally more susceptible to dissolution under acidifying conditions. Calcifying marine organisms may experience acute or chronic stress responses well before carbonate undersaturation occurs, often when the saturation state of $CaCO_3$ minerals falls within the range of 1 to 2. This document focuses on two critical thresholds: 1) $\Omega = 1$, the thermodynamic dissolution boundary for $CaCO_3$ (Morse et al. 2007); and 2) a conservative biological threshold of $\Omega = 1.5$, deemed suboptimal for marine life, as it is associated with measurable physiological impacts and considered an early warning level for adverse biological effects (Dixson et al. 2010, Keppel et al. 2012, Gazeau et al. 2013, Waldbusser and Salisbury 2014, Long et al. 2016, Rodriguez-Dominguez et al. 2018, Bednaršek et al. 2019, Siedlecki et al. 2021).

While acidification-driven dissolution is primarily an inorganic process governed by undersaturation states of $CaCO_3$ minerals, marine calcification is biologically mediated and therefore more complex. Biocalcification typically involves uptake of Ca^{2+} and HCO_3^- as substrates (Mann 2001, Allemand et al. 2004, Mackinder et al. 2010, Stumpp et al. 2012, Cyronak et al. 2016, Kahil et al. 2021). The specific pathways of biocalcification vary widely among taxa, involving different modes of inorganic carbon acquisition and sensitivity to proton (H^+) concentrations (Mann 2001). This physiological and taxonomic diversity makes it difficult to predict the net response of marine calcifiers based solely on variability in the Ω metric (Bach 2015, Ninokawa et al. 2024).

The substrate-inhibitor ratio, defined as the ratio of the substrate ($[HCO_3^-]$) to the waste product ($[H^+]$), has been proposed as an additional metric to assess the influence of changing carbonate chemistry on biocalcification (Bach 2015). A higher SIR ($[HCO_3^-]/[H^+]$ in mol μmol^{-1}) indicates more favorable conditions for calcification, emphasizing the importance of HCO_3^- as a calcification substrate (e.g., Jokiel 2011, Jokiel et al. 2013, Bach 2015, Cyronak et al. 2016). It also acknowledges the need for organisms to overcome biochemical inhibition from waste protons, as H^+ must be expelled when HCO_3^- is used to form $CaCO_3$ (Roleda et al. 2012, Cyronak et al. 2016). Under elevated OA conditions, the exchange of H^+ between internal cellular compartments and external seawater becomes increasingly difficult, thereby raising the energetic cost of maintaining internal pH homeostasis (Toyofuku et al. 2017). As noted earlier, while pH is typically presented on the total scale, the hydrogen ion concentrations in the ratio $[HCO_3^-]/[H^+]$ (in mol μmol^{-1}) are expressed on the free scale. This distinction is biologically relevant, as marine calcifiers interact directly with free ions in their environment. Although the SIR provides a straightforward numerical measure to conceptualize $CaCO_3$ production and enhance our understanding of how changing chemical conditions affect calcifying organisms, it

does not fully encompass the intricate relationships among carbonate system variables that are believed to drive calcification, as noted by others (Ninokawa et al. 2024).

2.3 ANALYSES

2.3.1 CO_2-carbonate system laboratory analyses

The marine CO_2-carbonate system regulates seawater acidity and modulates atmospheric CO_2 exchange (Emerson and Hedges 2008). Over the past two centuries, the ocean has absorbed a substantial fraction of anthropogenic carbon emissions, thereby mitigating climate change (Khatiwala et al. 2009, DeVries 2014, Gruber et al. 2023). However, its buffering capacity is declining, raising concerns about ecosystem impacts. In this report, water column profiles of TA, DIC, and pH_T are determined directly from seawater samples and used to calculate the full suite of seawater carbonate chemistry parameters. These are then used to identify conditions such as hypercapnia (pCO_2 > 1000 µatm) and calcium carbonate ($CaCO_3$) undersaturation ($\Omega_{CaCO_3} < 1$).

Seawater pH_T is determined spectrophotometrically using the dye perturbation method (Clayton and Byrne 1993, Dickson 2010). A volume of 40 µl of purified 2 mM m-cresol purple solution (University of South Florida) is added to approximately 28 ml of seawater sample held at 25 ± 0.5 °C in a 10 cm cylindrical quartz cell (100 mm length), and thoroughly mixed. Absorbances at 434, 578, and 730 nm are recorded with a temperature-controlled Agilent Technologies Cary 60 spectrophotometer, and blank-corrected ratios are used to calculate pH_T. While pH measurements are not corrected for dye perturbation, the m-cresol purple dye solution is visually inspected daily, and measurements are conducted to ensure its stability over time. Analytical precision and accuracy are evaluated daily by comparing measurements of a tris(hydroxymethyl)aminomethane (TRIS) buffer solution prepared at a salinity of 30 (Millero 1986). Both TRIS buffer and m-cresol purple reference solutions are verified every two days to ensure the reliability of calibration standards. Typical precision and accuracy are ± 0.003 pH units or better.

Total alkalinity is determined using open-cell potentiometric titration (Mintrop et al. 2000, Dickson 2010) with an automated sampling system. Each 104 mL seawater sample is warmed to 25 ± 0.5 °C and titrated with 0.1 M hydrochloric acid to the Gran equivalence point using a computer-controlled Dosimat (Metrohm AG, USA) dispenser coupled with a combination glass electrode. Certified Reference Materials (CRM, Dickson) are analyzed regularly (every 2 days) and used to adjust titrant concentration, providing a correction factor applied to all sample alkalinity calculations. TA analytical precision, determined from repeated analyses of bulk seawater, is reported as < 1.5 µmol kg^{-1}.

Total dissolved inorganic carbon is quantified using an automated sampling and gas extraction system coupled to a coulometric analyzer (Johnson et al. 1993). A measured aliquot of 17.5 mL seawater, equilibrated at 25 ± 0.5 °C, is transferred into a stripping chamber containing 1 mL of phosphoric acid (8.5 %). Acidification liberates CO_2, which is purged from the sample by ultrahigh-purity (UHP) nitrogen gas and directed to a coulometric cell for titration and photometric quantification. Dickson CRM is analyzed daily to calibrate the coulometer prior to sample measurements. Analytical precision for DIC is < 2 µmol kg^{-1}.

2.3.2 CO_2-carbonate system calculations and data visualization

Various seawater CO_2-carbonate system parameters, including pCO_2, Ω_A, Ω_C, CSVI, and SIR are calculated using in situ values of salinity (S), temperature (T), pH (typically on the total scale unless otherwise specified, e.g., for the SIR which reports H^+ on the free scale), total alkalinity (TA), and dissolved inorganic carbon (DIC) data with the Seacarb package (version 3.3.3) for R (Gattuso et al. 2024). Salinity and temperature values are extracted from CTD profiles at depths corresponding to the sampled bottles (e.g., Figure 2). The following constants are applied according to best-practice recommendations (Orr et al. 2015): the first and second dissociation constants for carbonic acid, K_1 and K_2 computed on the total scale (Lueker et al. 2000), the hydrogen sulfate constant K_{HSO_4} (Dickson 1990), the hydrogen fluoride constant K_f (Perez and Fraga 1987) is used as the default unless temperature or salinity are outside specified ranges, then Dickson and Riley (1979) is used, and total boron following Lee et al. (2010). When possible, the measured TA-pH_T pair is used to determine pCO_2, Ω_A, and Ω_C, SIR, and other OA metrics as this pair provides the best consistency in this region (Raimondi et al. 2019, Gibb et al. 2023). Data visualization is performed using R software (R version 4.4.2 - “Pile of Leaves”). Temporal data interpolation for the vertical water column plots at Rimouski Station is conducted using the non-parametric Locally Estimated Scatterplot Smoothing (Loess) method, which effectively handles noisy data, provides a robust fit, and assists in capturing underlying trends (Moraga 2023). Temporal trends at Rimouski Station are further assessed with linear regression models, followed by post-estimation diagnostics to evaluate the residual normality, autocorrelation, and heteroscedasticity. Spatial data interpolation for regional maps is conducted using Inverse Distance Weighting (IDW), while interpolation for channel transects is conducted using the Radial Basis Function (RBF) smoothing method, an approximation technique well suited for handling sparse and scattered data (Majdisova and Skala 2017).

2.4 ANNUAL ANOMALY SCORECARDS

Normalized anomalies for the indices presented in scorecards are computed for both Rimouski Station and EGSL regions. Each anomaly is calculated as the difference between a variable’s annual average and its climatological mean (reference period 2014–2020), divided by the standard deviation (SD) over the climatological period. For the Northumberland Strait region, the spatial climatology is presently based on observations from 2017 to 2020 due to the absence of data in earlier years. A caveat of using short climatologies for carbonate chemistry dynamics is that these reference periods may already incorporate some degree of anthropogenic acidification and other CO_2-driven changes, potentially biasing recent anomaly estimates toward smaller magnitudes. Temporally extending the baseline to include earlier years could yield more pronounced recent anomalies and provide a more robust representation of cumulative changes in pH and other carbonate system parameters over time.

Anomalies are displayed as scorecards, where above-normal anomalies are shown in shades of red, and below-normal anomalies in shades of blue, with increasing color intensity corresponding to greater deviations from the mean. White cells represent anomalies within ± 1/2 SD and are considered normal conditions (i.e., similar to climatology). Grey cells indicate insufficient or missing data. To depict environmental variation patterns across the Northwest Atlantic shelf, zonal scorecards summarizing anomalies in TA, DIC, pH_T, SIR, pCO_2, Ω_C, and Ω_A from all AZMP regions are presented in Galbraith et al. (2025a).

Annual anomalies of CO_2–carbonate system indices are derived from mean annual values estimated at the high-frequency monitoring station and across the five EGSL regions shown in Figure 1. These estimates are generated using Gaussian General Linear Models (GLMs), a statistical approach frequently applied within the AZMP framework (e.g., Blais et al. 2025). Because chemical oceanographic datasets often exhibit uneven sampling and sparse observations, GLMs provide a robust framework for adjusting seasonal and spatial imbalances, reducing bias from irregular data coverage. The models applied were as follows:

For the high-frequency monitoring station:
$\log_{10}(y) = \alpha + \beta_{Year} + \delta_{Month} + \varepsilon$

For the regional analyses:
$\log_{10}(y) = \alpha + \beta_{Year} + \delta_{Season} + \gamma_{Station} + \varepsilon$

where y is the response variable, α is the intercept, and ε is the error. The GLM is applied to each region separately. For Rimouski Station, β and δ are the categorical effects for year and month, respectively. For the EGSL regions, β, δ, and γ are the categorical effects of year, season, and station, respectively. Prior to model fitting, values are $\log_{10}$ transformed to account for the skewed distribution of observations. Least-square means computed using type III sums of squares, are used as standardized annual estimates to account for uneven seasonal and spatial sampling. Although adjusted R^2 values are generally low and categorical effects sometimes non-significant, GLMs remain appropriate for generating standardized annual means that are more robust than simple arithmetic averages when data coverage is uneven. Detailed GLM outputs (significance of each factor and adjusted R^2) are presented in Appendices 1 and 2.

While comparing 2024 carbonate-system data against a relatively short climatological baseline (2014–2020) has limitations, such as reduced ability to capture long-term variability and potential bias from short-term anomalies, the approach remains valuable for current assessments. This is especially true in deeper waters, where limited ventilation allows CO_2 to accumulate, leading to clearer ocean acidification signals even when using a relatively short climatological baseline. Although the short reference period may be less informative for surface waters, it can still reveal meaningful changes and help identify emerging patterns when interpreted with appropriate context and caution. Confidence in the assessment of the surface reference state and in the identified long-term trends will increase as these measurements are repeated and longer time series become available for analysis.

3. RESULTS

Dynamic estuarine and semi-enclosed oceanic environments, like the St. Lawrence marine system, exhibit substantial variability in their chemical properties, shaped by complex physical and biological interactions. While this report provides details about acidification and other CO_2-driven conditions, comprehensive descriptions of the 2024 physical and biogeochemical conditions in the EGSL are provided in Galbraith et al. (2025b) and Blais et al. (2025), respectively.

3.1 INORGANIC CARBON STATE VARIABLES

3.1.1 High-frequency monitoring station

Vertical profiles of CSVI values at Rimouski Station (Figure 3) illustrate the seasonal and depth-dependent variability of carbonate buffering conditions, comparing 2024 observations with the climatological mean and normalized anomalies. Vertical CSVI patterns typically show a broad decreasing trend with increasing depth. In the climatology, CSVI values remain relatively stable within the Cold Intermediate Layer (CIL : typically 50–100 m; Galbraith et al. 2025b), while the upper-water values display greater seasonal variability, reflecting stronger influences from surface processes. Beyond 200 m, climatological CSVI values remain below 0 µmol kg^{-1} for most of the year, with a small pocket dropping below −10 µmol kg^{-1} in December. During the 2024 summer months (July to September), the CSVI = 0 threshold shoaled, reaching the lower boundary of the CIL, near 150 m. Additionally, waters below 200 m exhibited CSVI values ranging between -10 and -25 µmol kg^{-1} from May to November in 2024, a feature absent in the climatology. Anomalies of CSVI in 2024 were mostly below normal throughout the water column with some above-normal values in the surface layer, as well as near-normal anomalies (surface to ca. 150 m) during October and November.

3.1.2 EGSL regions

The CSVI scorecard analysis provides an overview of annual regional averages, highlighting spatial and temporal variability in carbonate system vulnerability and emerging signs of reduced buffering capacity, particularly at depth (Figure 4). Complementary scorecards for DIC and TA (Figure 5) reveal annual anomalies that contextualize these carbonate chemistry trends. Spatial maps of CSVI (Figure 6), together with TA (Figure 7) and DIC (Figure 8) distributions, show the full range of values and anomalies across stations and depths, enabling finer-scale interpretation of carbonate system variability and biogeochemical stress. These patterns are most pronounced at intermediate and deep horizons (200 m, 300 m, and near-bottom), where signals intensify and spread.

Across all five EGSL regions, CSVI annual averages generally exhibit a vertical gradient, decreasing from surface to deeper waters, reflecting a broad-scale decline in buffering capacity with depth (Figure 4). Surface waters exhibit the highest CSVI climatological values. At 50 m, buffering capacity begins to decline, and by 100 m, a marked drop in CSVI is observed across all regions. At 200–300 m, several sites, including Rimouski Station and the Estuary, exhibit low, near-zero, or negative climatological average CSVI values, indicating a critical loss of buffering capacity. While the declining trend in average CSVI values is evident from the surface through the mid-water column, and in many cases extends into deep waters, all regions except Rimouski Station show a tendency for localized increases in climatological CSVI values near the bottom. Although these increases are generally within the variability of the adjacent depth horizon, this suggests more complex carbonate system dynamics closer to the seafloor. These near-bottom anomalies coincide with mixed TA and DIC signals (Figure 5) likely shaped by local physical, chemical, and biological processes, suggesting the potential for benthic–pelagic coupling in carbonate system behavior.

Temporal analysis indicates a deterioration in buffering capacity over the past decade. The reference period (2014–2020) is generally characterized by relatively stable CSVI conditions and fewer extreme anomalies (Figure 4). However, from 2020–2021 onward, vulnerability expands spatially and intensifies at depth. Vulnerable sites such as Rimouski Station and the

Estuary show temporal clustering of below-normal anomalies, suggesting potential shifts in deeper carbonate system dynamics. Since 2019, deep waters (200–300 m) of the Estuary have consistently remained below the CSVI threshold of zero, indicating sustained carbonate system vulnerability. More recently, the Northwest Gulf has approached this threshold, with near-zero to negative CSVI values emerging in 2023. The years 2023–2024 mark a notable period of system instability characterized by widespread below-normal CSVI anomalies and persistent signs of carbonate system weakening across multiple regions. Time series CSVI record lows were observed in 2024 at 200 m at Rimouski Station (-11 µmol kg^{-1}), in the Estuary (-11 µmol kg^{-1}), Northeast Gulf (27 µmol kg^{-1}), and Centre Gulf (36 µmol kg^{-1}).

Spatial distributions of climatological CSVI values at 200 and 300 m (Figure 6) display a channel-oriented gradient. Buffering capacity decreases from mouth to head in the Laurentian and Anticosti Channels, while the pattern is less distinct in the Esquiman Channel (see Figure 1 for geographic landmarks). Most regions maintain positive climatological CSVI values, but values approach zero in the Estuary and parts of the Northwest Gulf. In 2024, buffering capacity was broadly weaker than during the 2014–2020 climatological period, with CSVI values declining across the EGSL and near-zero or negative values in the Estuary and parts of the Northwest Gulf. The expansion of the CSVI threshold contour in 2024 marked a growing zone of carbonate stress at 200 m. Anomalies were predominantly below normal (Figure 6), indicating broad buffering capacity decrease at this depth. This decrease was likely driven by DIC accumulation (Figure 8), with additional influence from localized below-normal TA anomalies (Figure 7). Anomalies at 300 m in 2024 were broadly near-normal in Centre Gulf with below-normal anomalies in the Estuary and parts of the Northwest Gulf. Near-bottom waters show mixed buffering conditions in 2024. Most regions exhibit positive values, but climatological CSVI values are already negative in parts of the lower Estuary. In contrast, strong buffering persists in Northumberland Strait, likely maintained by lower DIC concentrations (Figure 8), which help sustain carbonate stability despite low TA (Figure 7). In 2024, near-bottom CSVI values declined further. Negative CSVI values expanded eastward, appearing in pockets west of the Magdalen Islands and underscoring the growing vulnerability of the carbonate system across the EGSL.

3.2 POTENTIAL OF HYDROGEN

3.2.1 High-frequency monitoring station

Vertical bottle profiles at Rimouski Station provide an integrated view of pH_T conditions across the water column (Figure 9). These profiles compare 2024 observations with the climatological mean and normalized anomalies, highlighting departures from expected seasonal ranges. Figure 10 offers a closer examination of temporal dynamics at two depth ranges surface waters (0–15 m) and near-bottom waters (270–320 m). It is worth noting that in these time series, the relatively short time frame of the climatology, along with occasionally sparse data, may contribute to its somewhat noisy appearance (Figure 10).

Vertical pH_T climatological values show a consistent reduction with increasing depth, with waters below 100 m remaining relatively well stratified during the seasonal cycle (Figure 9). Surface climatological pH_T shows greater seasonal variability, driven by dynamic physical and biogeochemical processes. The highest pH_T (and lowest pCO_2 values; Figure 9) are observed in the euphotic layer during summer, coinciding with the activity of photosynthetic phytoplankton

communities and warmer surface waters, both of which contribute to the reduction of CO_2 content (Borges and Gypens 2010, Hall et al. 2023). In 2024, seasonal pH_T values decreased notably below 50 m, with near-bottom waters dropping below 7.5 in early summer (June–July). Corresponding 2024 anomalies were mostly below normal at depth, with occasional above-normal features in surface layers (Figure 9).

The 2024 anomaly patterns at depth occur against a backdrop of accelerating trends: monthly near-bottom pH_T values have diverged from the climatological mean since 2020 at Rimouski Station (Figure 10). The overall rate of decline in near-bottom pH_T was −0.0057 units yr^{-1} between 2014 and 2024 ($p < 0.001$) but accelerated to −0.0107 units yr^{-1} during 2019–2024 ($p < 0.001$), indicating a significant but non-monotonic decrease in pH_T. This represents a near-doubling of the rate of acidification, translating into annual acidity increases of 1.3% and 2.5%, respectively. Such acceleration signals an amplification of OA in near-bottom waters over the past five years, although conditions remained relatively stable in 2024 compared with 2023. The reduction in pH_T is in lockstep with declining buffering capacity, evidenced by persistently negative CSVI values (Figure 3), highlighting intensifying stress within the local carbonate system.

3.2.2 EGSL regions

Annual pH_T values (Figure 11), spatial distributions (Figure 12), and corresponding anomalies indicate a vertically stratified pH_T pattern and increasing acidification signals in deep waters of the EGSL, consistent with other carbonate system parameters (e.g., Figures 4 and 6).

The pH_T scorecards show a depth-dependent gradient across EGSL regions (Figure 11). Surface waters show the highest values, with 2014–2020 pH_T means from 7.93 in the Estuary to 8.02 in the other regions. Climatological pH_T averages decline with depth, likely reflecting organic matter remineralization and limited CO_2 ventilation. At 100 m, climatological values drop by 0.1–0.2 units as compared to the surface. The lowest climatological pH_T values occur near 300 m, reaching 7.56 in the Estuary and 7.74 in the Centre Gulf. Near-bottom waters exhibit slightly higher climatological average pH_T than at 300 m (or at 100 m in the Magdalen Shallows), since average bottom depth is generally shallower than 300 m, but they remained more acidified than surface layers.

Temporal analysis indicates an intensification of acidification over the past decade (Figures 11 and 12). The reference period (2014–2020) is characterized by relatively few extreme anomalies. The year 2020 marks the beginning of multiple below normal pH_T anomalies across several EGSL regions, particularly in 100 m waters and deeper. A clear and consistent trend of below normal pH_T anomalies is observed at 200 m across all deep regions since 2020 (Figure 11), pointing to broad-scale intensification of acidification at this intermediate depth. This trend continued in 2024 with predominantly below-normal spatial pH_T anomalies at 200 m (Figure 12). The spatial 2024 pH_T anomalies at 300 m were mostly below normal in the Estuary and part of the Northwest Gulf, while they are mostly near normal in the Centre Gulf (Figure 12). In 2024, time series record-low pH_T annual means were observed at Rimouski Station (7.85 at 50 m and 7.55 at 200 m) and in the Estuary (7.55 at 200 m). Several 2024 record-low pH_T values matched earlier extremes observed between 2020 and 2023, including 7.85 at 50 m and 7.54 near-bottom in the Estuary, 7.87 at 100 m in the Northeast Gulf, and 7.70 at 200 m in the Centre Gulf. Together, these patterns document a decade-long progression toward increasing acidified deep and intermediate waters across the EGSL.

Spatial maps indicate that pH_T distributions at 200 m and 300 m during 2014–2020 (Figure 12) closely follow the channel-oriented gradient observed in the climatological CSVI (Figure 6). Acidification strengthens from mouth to head in the Laurentian and Anticosti Channels, while the Esquiman Channel shows a relatively more uniform spatial pattern. Climatological pH_T distributions are more spatially complex in near-bottom waters reflecting localized processes across wide-ranging bottom relief. Highest near bottom climatological pH_T values are found in shallow near-coastal waters of the Magdalen Shallows and Northeast Gulf regions. The lowest near-bottom pH_T values are concentrated in the Lower St. Lawrence Estuary, particularly in the downstream reaches of the deep Laurentian Channel.

3.3 PARTIAL PRESSURE OF CO_2

3.3.1 High-frequency monitoring station

Profiles at Rimouski Station illustrate vertical pCO_2 structure across the water column (Figures 9 and 10). They contrast 2024 measurements with climatological means and normalized anomalies to identify departures from expected seasonal trends. Details on the temporal variability in pCO_2 monthly means over the past decade are presented at two depth ranges: surface (0–15 m) and near-bottom (270–320 m) (Figure 10).

The climatological vertical and seasonal distribution of pCO_2 at Rimouski Station reveals a well-defined stratification of pCO_2 throughout the year (Figures 9 and 10). Surface waters down to ca. 150 m show variability, generally oscillating between ~400 to 800 µatm, with values fluctuating seasonally. Minimum pCO_2 values occur in spring and early summer, reflecting biological CO_2 drawdown during the spring, followed by a progressive increase through late summer and fall. This seasonal rise likely reflects reduced CO_2 uptake later in the phytoplankton growth season and the influence of accumulated respiratory CO_2 produced through organic-matter remineralization. The fall deepening of the CIL (Galbraith et al. 2025b, Fig.66) likely also contributes to elevated subsurface CO_2 during this period. At greater depths, pCO_2 levels are consistently elevated. The 1000 µatm threshold, marking hypercapnic conditions, is positioned below the CIL, at approximately 150 m, and remains relatively vertically stable throughout the seasonal survey period of the climatology (2014–2020). Below this depth, climatological pCO_2 values increase further, reaching 1300–1400 µatm in near-bottom waters (Figures 9 and 10), indicating a hypercapnic state at Rimouski Station since measurements began in 2014.

In 2024, pCO_2 values were elevated across much of the water column compared to the climatological baseline (Figure 9). The hypercapnic threshold shoaled into shallower waters in 2024, approaching the ~100 m depth during the summer months (July to September). The anomaly pattern revealed a broad above-normal signal throughout much of the water column. The strongest above-normal 2024 anomalies were observed in deeper waters (below 150 m) during spring and early summer (May to July). While no temporal trend is observed in surface pCO_2, temporal patterns in monthly averaged pH_T values reveal a clear departure from the climatology since 2020 in near-bottom waters, with values approaching 1600 µatm (Figure 10).

3.3.2 EGSL regions

Time series of annual anomaly scorecards (Figure 11) summarize temporal pCO_2 patterns from 2014 to 2024 at six depths across the EGSL, contrasting 2024 observations with climatological

means and highlighting departures from expected ranges. Spatial distributions in Figure 13 show annual averages, climatology, and anomalies for 200 m, 300 m, and near-bottom waters, with hypercapnic zones (pCO_2 ≥ 1000 µatm) delineated by contour lines. Vertical sections in Figures 14, 15, and 16 detail gradients along the Laurentian, Anticosti, and Esquiman Channels, respectively, illustrating how pCO_2 structure and anomaly intensity vary from Cabot Strait to channel heads.

The pCO_2 scorecards show a strong vertical gradient across all EGSL regions, inversely mirroring pH_T (Figure 11). Surface waters have the lowest pCO_2, with climatological means (2014–2020) from 395 to 494 µatm across the EGSL. These values globally track annual atmospheric CO_2, which rose from ~398 µatm in 2014 to 414 µatm in 2020 (NOAA/GML, Lan and Keeling, last accessed in September 2025). Most surface waters fluctuate around atmospheric equilibrium, alternating between undersaturation and supersaturation relative to air due to seasonal and interannual variability. Annual pCO_2 values increase with depth across all regions. At 100 m, climatological values range from ~500 µatm (Centre Gulf) to ~700 µatm (Estuary). At 200 m, most regions reach ~800–1200 µatm, with hypercapnia (>1000 µatm) occurring in the Estuary and Northwest Gulf. The highest climatological pCO_2 values generally occur at 300 m.

Temporal analysis shows that pCO_2 trends mirror pH_T patterns but with opposite direction, reflecting intensified carbon accumulation since 2020 (Figure 11). This mirroring is expected, as pCO_2 is derived from pH and other carbonate system parameters (TA in this document), underscoring the coupled nature of these changes across the EGSL. During the reference period (2014–2020), anomalies are variable and generally moderate. From 2020 onward, above-normal anomalies tend to dominate at intermediate and deep layers (100 m to 300 m), indicating a shift toward higher pCO_2. In 2024, the pCO_2 scorecards revealed a general continuation of the post-2020 trend toward elevated pCO_2, with pronounced increases observed beneath the CIL and extending into near-bottom waters across most deeper regions (Figure 11). Exceptions to this overall pattern in 2024 were evident in the Centre Gulf and Northeast Gulf, where pCO_2 conditions at 300 m and near the bottom remained near normal. In 2024, the Magdalen Shallows region remained vertically more variable, showing a mix of normal, below-, and above-normal anomalies, along with lower annual pCO_2 values overall (maximum of 677 µatm at 100 m). Hypercapnic conditions were observed at 200 m in all deep regions except the Centre Gulf, which nonetheless approached the threshold with a value of 940 µatm in 2024. Hypercapnia was also present in 2024 at 300 m and in near-bottom waters of the Estuary (including Rimouski Station) and the Northwest Gulf, reflecting subsurface CO_2 accumulation along the deep waters of the Laurentian Channel. In 2024, time series record-high pCO_2 annual means were observed at 50 m (Estuary: 613 µatm, Rimouski Station: 605 µatm) and at 200 m (Estuary: 1357 µatm, Rimouski Station: 1359 µatm).

Spatial pCO_2 patterns in deep and near-bottom waters (Figure 13) are consistent with overall patterns of CSVI (Figure 6), DIC (Figure 8), and pH_T (Figure 12), with a distinctive channel-oriented gradient. At 200 and 300 m depth, lowest climatological pCO_2 values occur in the Northeast Gulf and Centre Gulf near Cabot Strait, reflecting Atlantic water influence. On the other end of the spectrum, the highest climatological pCO_2 spatial values are found in the Estuary and Northwest Gulf regions. These gradients highlight the role of water mass origin and residence time in shaping mid-depth inorganic carbon as can be seen in channel transects (Figures 14, 15, and 16) that reveal these longitudinal shifts.

In the Laurentian Channel, hypercapnia shoaled substantially, rising from depths below ~200 m in the climatology to ~100 m in 2024 and extended farther downstream from the channel head (Figure 14). It formed a tongue-like structure that skirted Anticosti Island to the south, stretching ~600 km toward Cabot Strait and closely mirroring the 30 % oxygen saturation contour shown in Figure 10 of Blais et al. (2025). Positive pCO_2 anomalies along the Laurentian Channel transect in 2024 were evident, particularly around the 200 m horizon. The Anticosti Channel also showed an upward expansion of hypercapnic conditions, shoaling from ~250 m in the climatology to ~200 m in 2024 (Figure 15). The 2024 anomaly patterns in Anticosti Channel were broadly dominated by above-normal conditions, particularly near Anticosti Island, except for a localized pocket of below-normal anomalies in the deep waters (deeper than 300 m) at the mouth of the channel. Localized hypercapnic conditions were also found below 250 m in the Esquiman Channel with little variation between 2024 and the climatological period (Figure 16). However, in 2024, partial pressures of CO_2 broadly increased in subsurface layers of the Esquiman Channel, particularly between the surface and ~200 m depth as indicated by the predominance of above-normal anomalies at these depths (Figure 16). Near-bottom waters of the EGSL show greater spatial variability in pCO_2 (Figure 13) reflecting a diverse near-seafloor environment shaped by both depth and proximity to coastal and shelf areas. Climatological values reveal a clear gradient, with the highest pCO_2 near the Laurentian Channel head and lower but still elevated levels near the Anticosti and Esquiman Channel heads. Climatological partial pressures of CO_2 in shallow areas such as the Magdalen Shallows largely remain lower due to stronger mixing and ventilation. In 2024, hypercapnic conditions intensified in the near-bottom waters of the Northwest Gulf, while new pockets emerged near Anticosti Island, in the Strait of Belle Isle, and the Magdalen Shallows, indicating localized intensification of CO_2 accumulation. These patterns are visible on the near-bottom spatial anomaly map (Figure 13), which shows a patchy distribution of above-normal anomalies interspersed with localized near- and below-normal features, with the strongest above-normal anomalies occurring in the new hypercapnic patch of the Magdalen Shallows.

3.4 INDICES OF BIOGENIC CARBONATE CALCIUM FORMATION AND DISSOLUTION

3.4.1 High-frequency monitoring station

The climatological vertical and seasonal distribution of Ω_A and Ω_C (Figure 17), and the SIR (Figure 18) at Rimouski Station can be interpreted in terms of water column stratification and of the seasonal cycle.

Surface waters are generally supersaturated during the summer months with respect to climatological aragonite ($\Omega_A \geq 1$), whereas the shoulder seasons, spring and fall into winter, show periods of surface undersaturation, as indicated by the upward intrusion of the $\Omega_A = 1$ contour. Climatological depth contours of Ω_A suggest that intermediate to near-bottom waters (below ~100 m) at Rimouski Station remain chronically undersaturated with respect to aragonite throughout the year, posing persistent challenges for calcifying organisms inhabiting these deeper layers.

The climatological distribution of Ω_C at Rimouski Station shows a broadly similar structure to Ω_A, but with key differences in magnitude and depth of undersaturation (Figure 17). Surface waters remain consistently supersaturated ($\Omega_C \geq 1$) throughout the year, with values typically exceeding

1.5. Unlike Ω_A, values of Ω_C do not fall below 1 in the upper 100 m during the climatological period. Undersaturation occurs only below ~200 m, reflecting calcite's greater stability due to its lower solubility (Mucci 1983) and more compact crystal structure (Morse and Mackenzie 1990). Consequently, calcite remains supersaturated under more acidic conditions and at greater depths, making it less prone to early undersaturation than other carbonate minerals.

At Rimouski Station, climatological SIR values in the upper 100 m show high values (>0.160 mol μmol^{-1}) from April through December, with the highest value in June-July in surface waters (>0.220 mol μmol^{-1}, Figure 18), indicating favorable conditions for calcification. Values of SIR decrease with depth, reaching ~0.100–0.160 mol μmol^{-1} between 100 and 200 m as $[H^+]$ rises with CO_2 accumulation. Below ~200 m, values fall under 0.100 mol μmol^{-1}, a level linked to metabolic stress in calcifiers (Thomsen et al. 2015), implying increased potential for sustained energetic constraints for organisms inhabiting these depths.

In 2024, values of all three $CaCO_3$-related indices (Ω_A, Ω_C, SIR) were notably lower across much of the water column compared to the climatological baseline (Figures 17 and 18). For aragonite, surface supersaturation during spring and summer remained similar to climatology, but the zone with values between ~0.70 and 1.00 was vertically compressed, with the 0.70 isoline reaching 100 m in summer whereas in the climatology it was centered at ~150 m. Calcite and SIR followed the same trend of vertical compression, yet with different threshold depths: the $\Omega_C = 1$ and SIR = 0.100 mol μmol^{-1} contours shoaled to ~100 m by early summer reducing the depth range of favorable $CaCO_3$-related conditions in 2024 as compared to the climatology. This 2024 vertical contraction in Ω_A, Ω_C, SIR aligned with anomaly patterns, which showed extensive below-normal conditions from mid-depth to near-bottom throughout the survey period. The only exception occurred in the upper ~50 m, where above-normal anomalies were present.

3.4.2 EGSL regions

Annual anomaly scorecards (Figures 19 and 20) track changes in Ω_A, Ω_C, and SIR from 2014 to 2024 at six depths across the EGSL, contrasting 2024 conditions with climatological means and identifying departures from expected ranges. Figure 21 complements these time series by showing boxplots of aragonite and calcite undersaturation depth distributions for the reference period (2014–2020) and 2024. Spatial patterns for 200 m, 300 m, and near-bottom waters, showing annual averages, climatology, anomalies, and contour lines marking critical thresholds are presented for Ω_A (Figure 22), Ω_C (Figure 23), and SIR (Figure 24).

Across the EGSL, a consistent depth-dependent decline in climatological Ω_A and Ω_C (Figure 19), and SIR (Figure 20) is evident. Surface waters of the Northwest Gulf and the Estuary, including Rimouski Station, fall below the biological threshold of $\Omega_A = 1.5$, a key benchmark for calcifying organisms (Figure 19). All other EGSL regions maintain surface Ω_A climatological averages above this limit of 1.5. At 50 m, the $\Omega_A = 1$ critical threshold is crossed in the Estuary and approaches this value in the Magdalen Shallows (1.01) and Northwest Gulf (1.07). At 200 m, 300 m, and in near-bottom waters, Ω_A climatological averages are consistently ≤ 1 across all EGSL regions. Calcite scorecards reveal the same depth-dependent pattern observed for climatological aragonite, but the Ω_C thresholds are crossed at greater depths, consistent with calcite's lower solubility (Figure 19). Unlike aragonite, surface and 50 m waters remain above the biological benchmark of $\Omega_C = 1.5$ across all EGSL regions, but this limit is crossed at 100 m in all regions except the Centre Gulf and Northeast Gulf, where climatological averages stay above 1.5. While Ω_C remains slightly above 1 at 200 m in the Estuary (1.02), it falls below this threshold at 300 m, whereas all other EGSL regions maintain supersaturation ($\Omega_C \geq 1$) throughout the water column during the reference period (2014–2020). Climatological SIR

follows the same vertical pattern as carbonate minerals, with critical values (SIR ≤ 0.100 mol µmol^{-1}) emerging at 200 m, 300 m, and near-bottom in the Estuary (Figure 20). All other EGSL regions show depth-related reductions in climatological SIR but remain above the 0.100 threshold throughout the water column.

Temporal variability in surface waters shows a dominance of above-normal anomalies for Ω_A and Ω_C since ~2021, marked by frequent, spatially coherent above-normal conditions (Figure 19). In 2024, time series record-high Ω_A and Ω_C annual means are observed at the surface for the Northwest Gulf, the Centre Gulf and the Northeast Gulf. Values of SIR diverge from this pattern: below-normal anomalies have become more common since 2020, particularly in surface waters of the Magdalen Shallows, Centre Gulf, and Northeast Gulf (Figure 20). The anomaly scorecards for subsurface, deep, and near-bottom layers reveal two distinct temporal regimes across the EGSL: ~2014–2019 and ~2020–2024 (Figures 19 and 20). During the first half of the record, anomalies were irregularly distributed across regions and years. Beginning around 2020, subsurface, deep, and near-bottom layers exhibit a shift toward below-normal Ω_A, Ω_C, and SIR anomalies in most EGSL regions. At 100 m and deeper, Ω_A, Ω_C and SIR anomalies cluster into mostly below-normal values, with the trend most pronounced at 200 m, where nearly all annual averages fall below climatological norms except for a single near-normal year in the Northwest Gulf (2022). The Magdalen Shallows exhibit greater variability in anomalies at different depth horizons with a persistent signal of above-normal Ω_A, Ω_C and SIR anomalies at 100 m since 2021. In 2024, anomalies at 200 m and deeper were predominantly below normal across deep-channel systems such as the Laurentian, Esquiman, and Anticosti Channels, with only a few instances of near-normal anomalies in the Centre Gulf and Northeast Gulf. Time series record lows in the 2024 annual means of Ω_A, Ω_C and SIR were noted at 200 m for all EGSL regions except the Northwest Gulf.

While these climatological profiles define the average annual vertical positioning of corrosive conditions, they do not capture the full range of variability across the multi-season sampling period. Boxplots provide a complementary view of mineral-specific depth distributions of aragonite ($\Omega_A < 1$) and calcite ($\Omega_C < 1$) undersaturation across the EGSL (Figure 21). Median depths of $\Omega_A < 1$ remain relatively stable across most regions between 2014–2020 and 2024, but in the Northeast Gulf the entire interquartile range shifts upward, indicating shoaling of corrosive conditions toward the surface and greater exposure of upper- and mid-depth ecosystems to acidification stress. Calcite undersaturation remains largely confined to the Estuary, Northwest Gulf, and Magdalen Shallows (Figure 21). In the Estuary, the median $\Omega_C < 1$ depth shoals from ~300 m in 2014–2020 to ~225 m by 2024. In the Northwest Gulf, the 2024 distribution shows a narrower interquartile range (IQR) and slight upward shift, indicating reduced variability and more uniform exposure to corrosive conditions.

The vertical perspectives presented in Figures 19 and 20 frame the spatial imprint of carbonate mineral stability and calcification potential across key depth layers (Figures 22, 23, and 24). At 200 m, climatological Ω_A values are below 1 in most regions, with the Estuary and Northwest Gulf most heavily undersaturated (Figure 22). In 2024, Ω_A declined further, leaving only a narrow supersaturated (≥ 1) zone near Cabot Strait. Patterns of climatological Ω_C (Figure 23) differ in magnitude but follow the same spatial progression: highest supersaturation near Cabot Strait and lowest in the Estuary and Northwest Gulf. By 2024, Ω_C decreased across all regions at 200 m. Spatial patterns in SIR values at 200 m echo these shifts (Figure 24). The climatology indicates favorable conditions (>0.100) in most areas, highest near Cabot Strait, lowest in the Estuary and Northwest Gulf. In 2024, SIR values declined everywhere at 200 m, with sharp reductions in the Estuary and Northwest Gulf. Across all three metrics, the 2024 pattern at 200 m was clear: below-normal anomalies confirmed widespread reduction in Ω_A, Ω_C and SIR.

At 300 m, climatological Ω_A remains below 1 across most regions, with small pockets of supersaturated values (≥ 1) in the Centre Gulf near Cabot Strait (Figure 22). In 2024, near-normal anomalies dominated in the Centre Gulf, while below-normal anomalies were present in the Estuary and parts of the Northwest Gulf. Spatial climatological Ω_C patterns mirror Ω_A but with higher absolute values (Figure 23). The climatology indicates widespread supersaturation, with strongest values in the Centre Gulf and Northeast Gulf and weakest in the Estuary and Northwest Gulf. In 2024, the anomaly pattern for Ω_C at 300 m mirrored that observed for Ω_A. Climatological SIR values remain above 0.100 mol μmol^{-1} in most areas, with highest values near Cabot Strait, lowest in the Estuary and Northwest Gulf (Figure 24). However, localized zones of SIR ≤ 0.100 mol μmol^{-1} are present near the head of the Laurentian Channel in the Estuary, and in 2024, unfavorable SIR zones expanded eastward towards the Northwest Gulf. In 2024, near-normal SIR anomalies dominated in the Centre Gulf, while below-normal anomalies were present in the Estuary and parts of the Northwest Gulf.

At near-bottom depths, carbonate indicators predominantly show intensified stress with irregular spatial patterns shaped by bathymetry and coastal proximity. Climatological Ω_A values are below 1 in many regions including the Estuary, Northwest Gulf and parts of the Magdalen Shallows and Northeast Gulf (Figure 22). In 2024, Ω_A declined further in near-bottom waters, expanding existing undersaturation zones and creating new pockets particularly in the Centre Gulf and Northeast Gulf. Climatological Ω_C (Figure 23) and SIR (Figure 24) show similar spatial patterns, with critical threshold crossings (Ω_C < 1; SIR < 0.100) concentrated in near-bottom waters at the head of the channel in the Estuary. In 2024, conditions in Ω_C and SIR deteriorated across several areas of the EGSL, with below threshold zones enlarging in the Estuary and emerging near Anticosti Island. Across all three metrics (Ω_A, Ω_C, and SIR), 2024 bottom-layer anomalies formed a fragmented pattern of mostly below-normal conditions, interspersed with near-normal areas.

4. DISCUSSION

4.1 SURFACE TO SEAFLOOR: ENVIRONMENTAL GRADIENTS IN CO_2-DRIVEN CONDITIONS

Unlike the open ocean, where acidification is primarily driven by atmospheric CO_2 uptake, estuaries and semi-enclosed oceanic environments are shaped by a more intricate suite of local processes (Cai et al. 2011, Mucci et al. 2011, Cai et al. 2017, Mucci et al. 2017, Cai et al. 2021, Gibb et al. 2023). Variable riverine inputs, complex circulation patterns, and intense biogeochemical cycling create highly dynamic environments where biological processing and carbonate chemistry are tightly coupled (Cai et al. 2021, Chen et al. 2023, Li et al. 2023). These regional factors can substantially alter the trajectory and expression of acidification, sometimes amplifying, modulating, or masking the direct influence of rising atmospheric CO_2 on seawater pH and other carbonate system parameters.

The EGSL marine system exemplifies these dynamics with its structure dominated by the Laurentian Channel, a submarine valley 250–500 m deep and 1240 km long that extends from the continental shelf to the Saguenay Fjord confluence (El-Sabh and Silverberg 1990). Estuarine circulation prevails, with buoyant surface waters flowing seaward and dense deep waters moving landward, driven by freshwater runoff from the Great Lakes and rivers draining Northern Quebec and Labrador (Chabot and Gilbert 2013). Freshwater inputs strongly influence surface carbonate variability and buffering capacity (Mucci et al. 2011). Seasonal changes in

temperature and salinity under atmospheric forcing further shape stratification, mixing, and nutrient supply, which in turn affect ecosystem productivity and CO_2-carbonate system fluctuations (Gilbert and Pettigrew 1997, Galbraith 2006, Lavoie et al. 2020, Lavoie et al. 2021, Gibb et al. 2023, Blais et al. 2025, Galbraith et al. 2025b).

Understanding these regional dynamics requires close attention to water mass structure and movement. In the EGSL, physical processes shape carbonate chemistry by controlling source-water delivery, vertical mixing, and the residence time of biogeochemical properties. Stratification, convection, and circulation patterns influence nutrient distributions and associated biological activities such as photosynthesis, respiration, and organic matter degradation. These processes drive carbon uptake and release, altering CO_2 conditions and interacting with physical drivers to produce short-term and seasonal variability in the carbonate system (Cai et al. 2021, Chen et al. 2023, Li et al. 2023). Shoaling of saturation horizons and other chemical boundaries can compress viable habitat for calcifying or CO_2-sensitive species (Findlay et al. 2025). A depth-resolved approach is essential for capturing the environmental envelope within which species exist (IPBES 2019) and for assessing how shifts in carbonate chemistry may compress that envelope over time. As such, interpreting acidification trends in these environments demands an integrated view of chemical, physical, and biological drivers, each contributing to the complex mosaic of carbonate system vulnerability in the EGSL. Though this report does not present a fully integrated analysis, it offers interpretive insights.

The vertical structure of the carbonate system in the EGSL reveals striking contrasts. In 2024, surface waters maintained broadly favorable chemical conditions, while deeper layers exhibited intensified vulnerability. This differentiation reflects in large part differences in ventilation and air–sea exchange shaped by the estuarine circulation, with surface layers strongly coupled to the atmosphere, while deep waters remain largely isolated. The Laurentian Channel bottom waters consist of Labrador Current waters (LCW) and North Atlantic Central waters (NACW), with proportions varying over decades (Bugden 1991, Gilbert et al. 2005, Jutras et al. 2023). Bottom waters in the Laurentian Channel are already preconditioned by anthropogenic CO_2 absorbed during their last surface residence (Gattuso et al. 1998, Orr et al. 2005, Gattuso and Hansson 2011, Mucci et al. 2011). Over the past century, this baseline has been compounded by shifts in mixing ratios between LCW and NACW entering the channel (Gilbert et al. 2005, Jutras et al. 2023), along with rising bottom-water temperatures (Galbraith et al. 2025b) and microbial degradation of organic matter (Thibodeau et al. 2006, Thibodeau et al. 2010, Genovesi et al. 2011). These processes can drive gradual deoxygenation and intensify acidification (Cai et al. 2011, Gehlen et al. 2011, Mucci et al. 2011, Mucci et al. 2017, Gibb et al. 2023, Blais et al. 2025, Galbraith et al. 2025a).

To reflect these contrasting regimes, the following discussion is organized into two parts: surface waters in contact with the atmosphere and deeper subsurface layers below the CIL, where carbonate dynamics are shaped by longer-term physical and biogeochemical processes.

4.1.1 Surface and upper waters: atmosphere-influenced and CIL-conditioned carbonate dynamics

This section focuses on the upper marine layers, where carbonate chemistry responds most directly to seasonal physical forcing and biological activity. Surface waters are inherently more variable than deeper layers, with chemical conditions shaped by short-term fluctuations in stratification, mixing, ice dynamics, riverine input, photosynthesis, air-sea CO_2 exchange, and

other local processes (Cai et al. 2021). Modifications in biogeochemical processes are key drivers of changes in seawater chemistry, particularly in controlling pH (Wallace et al. 2014, Kessouri et al. 2021). Phytoplankton blooms, for instance, can locally elevate pH within the sunlit euphotic layer through intense photosynthetic CO_2 uptake (Borges and Gypens 2010, Hall et al. 2023). Consequently, long-term trends in surface carbonate parameters generally require more than a decade of observations to be distinguished from natural variability. Annual surface anomalies in this report must therefore be interpreted considering local drivers, interannual variability, and episodic events that modulate carbonate chemistry from year to year.

In 2024, surface carbonate-system conditions across the EGSL revealed complex anomaly patterns. While some regions exhibited conditions less conducive to buffering and pH stability relative to the climatological period of 2014–2020, others remained within the expected range or even showed enhanced saturation states and reduced CO_2-driven stress. Such variations likely reflect natural interannual variability within a highly dynamic system, and should not be interpreted as directional trends. Notably, surface waters of the Estuary in 2024 exhibited above-normal annual anomalies in TA, CSVI, Ω_A, Ω_C, SIR, and pH_T, alongside near-normal conditions for DIC and pCO_2. These patterns signal overall more favorable than normal surface carbonate system conditions in 2024. The Northwest Gulf displayed a similar, though more subdued, anomaly pattern: TA, CSVI, Ω_A and Ω_C were mostly above normal, while other variables remained near climatological values. While causality cannot be assigned, record-low sea ice volume and extent during winter 2024 (Galbraith et al. 2025b) may have influenced carbonate system dynamics by reducing seasonal dilution and enhancing air–sea CO_2 exchange. With less ice formation, surface waters experience less dilution from meltwater, contributing to above-normal annual TA and buffering (CSVI) anomalies. At the same time, expanded open-water areas may increase CO_2 fluxes, promoting outgassing where surface pCO_2 exceeds atmospheric levels.

In contrast to the Estuary and Northwest Gulf, surface conditions in the Northeast Gulf, Centre Gulf, and Magdalen Shallows during 2024 were broadly, but not uniformly, characterized by above-normal annual pCO_2 anomalies, below-normal pH_T and SIR, despite similarly above-normal conditions of CSVI, Ω_A, and Ω_C. Elevated pCO_2 paired with reduced pH_T and SIR suggest stronger influence of respiration and remineralization relative to photosynthetic drawdown, particularly during stratified periods when organic matter degradation accumulates CO_2 in surface layers. This interpretation aligns with observations of below-normal chl *a* inventories (0–100 m) in these EGSL regions in early and late summer 2024, suggesting reduced phytoplankton biomass and limited biological CO_2 uptake during key growth periods (Blais et al. 2025, Fig. 28). Together, these diverse responses underscore the complexity of surface carbonate dynamics in semi-enclosed environments where physical and biological influences vary regionally.

At the 50 m and 100 m depth horizons, the 2024 carbonate system conditions across the EGSL were broadly characterized by below-normal or near-normal values of CSVI, pH_T, SIR, Ω_A and Ω_C, alongside mostly above-normal or near-normal pCO_2. These depth horizons, though below the surface, remain susceptible to seasonal mixing and often overlap with the CIL, formed from winter-cooled surface water, and isolated beneath the seasonal pycnocline (Galbraith et al. 2025b). Typically, the CIL's cooler temperatures promote CO_2 solubility, lowering pH_T and carbonate saturation states. In 2024, the mid-summer CIL minimum temperature ranked as the fourth highest since 1985 (Galbraith et al. 2025b). Although higher temperatures may reduce CO_2 solubility, they can also stimulate microbial respiration (Nydahl et al. 2013, Robinson 2019), increasing CO_2 production and altering carbonate chemistry. This interplay reinforces that temperature does not act in a straightforward way; it interacts with organic matter oxidation,

nutrient regeneration and mixing processes, creating complex patterns in carbonate system dynamics (Simpson et al. 2022). The CIL, though partly shielded from atmospheric forcing, is subject to episodic vertical exchange, mostly in winter (Cyr et al. 2011), which contributes to seasonal variability in its carbonate chemistry. Together, these conditions reflect the transitional nature of the CIL, partially coupled to surface dynamics, yet increasingly shaped by subsurface biogeochemical transformations as seasons progress.

One exception to this broad regional trend occurs in the Magdalen Shallows, where conditions at 100 m in 2024 showed above-normal pH_T, SIR, Ω_A, and Ω_C, alongside below-normal pCO_2. These departures appear to be part of a multi-year anomaly sequence that began in 2021, highlighting short-term variability that could reflect evolving local conditions. The Magdalen Shallows are a shallow shelf plateau where the CIL typically influences bottom-water temperatures through seasonal cooling and advection. However, in 2024, the mixed layer was unusually shallow and did not reach the seafloor at many stations (Galbraith et al. 2025b). Consistent with this limited mixing, 2024 near-bottom averages in the Magdalen Shallows reveal below-normal pH_T and SIR, near-normal Ω_A and Ω_C, and above-normal pCO_2 anomalies, as shown in the scorecards of annual means. However, the deepest sampled horizon at 100 m showed the opposite pattern, with higher pH_T and saturation states and lower pCO_2. These contrasting signals point to local mechanisms, possibly sediment–water interactions at the benthic–pelagic interface, shaping conditions in ways that override the expected mixing effect, but further investigation is needed to clarify their role.

4.1.2 Deeper subsurface waters: from channel depths to shelf bottoms

This section addresses the deeper layers of the EGSL intersected by the Laurentian, Esquiman, and Anticosti Channels. These waters originate near the continental shelf break and circulate landward with limited exchange with upper layers (Galbraith et al. 2025b). Regional gradients reflect deep-water transport along the channels: marine waters entering through Cabot Strait accumulate respiration-derived CO_2 as they progress landward. Density stratification may act as a physical barrier, trapping carbon-rich waters, and intensifying acidification toward channel heads. This connectivity is modulated by decadal shifts in LCW and NACW relative proportions, influencing carbonate system parameters and driving spatial variability in acidification exposure across the EGSL. Compared to surface layers, these deeper waters exhibit greater chemical stability, providing a useful baseline for detecting emerging trends. Variability at depth more strongly reflects persistent physical and biogeochemical processes rather than episodic events, offering a stronger basis for assessing sustained carbonate system constraints. Beyond these deep layers, bottom waters span a wide bathymetric range, where near-shore and sediment–water interactions, and variable mixing and ventilation further shape carbonate chemistry.

Among the deeper horizons, the 200 m layer stands out as a zone of pronounced, system-wide acidification. In 2024, all monitored regions intersecting the Laurentian, Esquiman, and Anticosti Channels exhibit below-normal anomalies for CSVI, pH_T, Ω_A, Ω_C, and SIR, coupled with above-normal DIC and pCO_2. This coherent convergence of anomalies across all carbonate system indicators and all EGSL regions represents a striking signal. This pattern is paralleled by concomitant oxygen trends: since 2020, a persistent below-normal anomaly in oxygen saturation has emerged across all deep regions of the EGSL at the 200 m horizon (Blais et al. 2025). This oxygen decline is intimately tied to respiration-driven processes that also influence carbonate chemistry. Hydrodynamic changes are likely key drivers of these signals. At 200 m, thermocline movements can entrain water from deeper layers near the temperature maximum zone, creating warm anomalies (Galbraith et al. 2025b, see Fig. 52) and introducing O_2-poor and CO_2-rich waters resulting from increased metabolic activity. Furthermore, recent Gulf

Stream intrusions, peaking in 2022, may have altered water mass properties (Galbraith et al. 2025b), compounding effects related to warmer temperatures in amplifying biogeochemical processes that contribute to acidification. The coherence and persistence of these anomalies underscore vulnerability of the 200 m horizon, where limited ventilation may amplify CO_2 accumulation and acidification risk. These anomalies cannot be attributed to reduced natural variability, since the 200 m horizon is as variable climatologically as deeper layers.

At 300 m, regional contrasts in carbonate system anomalies are more visible, aligning with differences in water mass structure reported in Galbraith et al. (2025b). In 2024, the Estuary and Northwest Gulf exhibit a deterioration pattern like that observed at 200 m: below-normal anomalies for pH_T, CSVI, Ω_A, Ω_C, and SIR, coupled with above-normal DIC and pCO_2, with strongest anomalies observed in the Estuary. The Estuary continued to warm in 2024 as the leading edge of the warm-water intrusion moved through the Laurentian Channel (Galbraith et al. 2025b). These conditions, combined with the time required for waters to reach the channel head, favor the accumulation of respired CO_2, intensifying acidification. In contrast, the Northeast Gulf and Center Gulf show near-normal conditions across all indicators at 300 m, demonstrating that subsurface vulnerability is more spatially heterogeneous at this depth. Waters at 300 m in the Center Gulf near the mouth of the Laurentian Channel were cooler in 2024 compared to 2023, due to increased LCW content, but still showed above-normal anomalies (Galbraith et al. 2025b). Blais et al. (2025) report the re-emergence of near-normal oxygen saturation values at 300 m in Cabot Strait, the first such occurrence since 2015. Because Cabot Strait is a primary entry point for source waters entering the Laurentian Channel and subsequently flowing into the Esquiman and Anticosti Channels, these near-normal conditions in parts of the Northeast Gulf likely reflect upstream water mass properties rather than local buffering capacity or biogeochemical resilience.

The final depth tier examined in this report encompasses near-bottom waters, which span a wide bathymetric range, from shallower shelf zones to the deepest troughs of the Laurentian, Esquiman, and Anticosti Channels. In 2024, near-bottom waters in the Estuary and Northwest Gulf exhibit a clear deterioration signal, with below-normal anomalies for CSVI, pH_T, Ω_A, Ω_C, and SIR, alongside elevated DIC and pCO_2. These anomalies mirror those observed at 200 m and 300 m, reinforcing the notion that the 2024 carbonate system constraints in these regions extend from mid-depths to the seafloor. However, patterns in other regions are less straightforward, likely reflecting the composite nature of bottom waters, where deep channel inflows and shelf-derived near-bottom layers converge, each with distinct carbonate system dynamics.

In the Northeast Gulf, near-bottom waters show slightly below-normal annual anomalies of CSVI, pH_T, SIR, and carbonate mineral saturation states, yet pCO_2 and DIC are also slightly below normal, a counterintuitive combination that may signal transitional conditions. This pattern could reflect the influence of mixed water masses, where deep channel inflows and shelf-derived bottom waters co-occur, each with distinct carbonate system signatures. It may also be shaped by the region's relatively high overall climatological (2014–2020) variability, which can obscure emerging trends or dampen anomaly strength. Despite these subdued anomalies, 2024 pCO_2 remains elevated in absolute terms, suggesting that acidification pressures persist even where interannual signals appear muted. The Centre Gulf presents a similarly muted profile, with near-normal CSVI and weakly below-normal anomalies across most indicators, apart from weak above-normal DIC and pCO_2. Spatial maps (Figures 6, 7, 8, 12, 13, 22, 23, and 24) reveal pronounced heterogeneity in anomaly patterns over the Magdalen Shallows, with some of the strongest local anomalies over the central plateau. These maps show areas of strongly below-normal anomalies alongside near-normal anomalies in pH_T, TA, CSVI, Ω_A, Ω_C, and SIR, as well

as mostly above-normal pCO_2. The overall regional annual mean anomalies integrate this variability, reflecting the same general pattern but with a weaker signal compared to localized peak anomaly values.

Overall, near-bottom carbonate dynamics in the EGSL exhibit structural and spatial complexity driven by bathymetry, mixing regimes, and proximity to sediment interfaces. Deep-channel inflows interacting with shelf-derived near-bottom waters create gradients in residence time, remineralization intensity, and ventilation exposure, all of which shape carbonate system conditions. In shelf zones, additional influences from freshwater discharge, nutrient loading, and terrestrial organic matter inputs further modify near-bottom chemistry, contributing to localized variability in buffering capacity and acidification risk. Modest increases in climatological CSVI near the bottom indicate that buffering capacity reflects mixed signals, where DIC and TA (Figure 5) are consumed or regenerated through physical, chemical, and biological processes. Resulting stoichiometric patterns vary regionally, underscoring the interplay of carbon and alkalinity-modifying mechanisms and the need to account for benthic–pelagic coupling when interpreting vertical carbonate system behavior. Collectively, the EGSL carbonate system dynamics reveal complexity spanning space and depth, as observed in other marine systems (Li et al. 2022), and reinforce the importance of depth-specific diagnostics for assessing carbonate system risk exposure across the EGSL.

4.2 PERSPECTIVES ON EGSL REGIONAL VULNERABILITY TO CO_2-DRIVEN STRESSORS

The following section shifts focus from overall annual anomaly trends to a tiered assessment of vulnerability, examining how CO_2-driven stressors manifest, co-occur, and accumulate across regions and depths of the EGSL in 2024. This framing highlights the spatial and vertical gradients of exposure, identifying zones where acidification and other CO_2-driven conditions most likely challenge ecosystem resilience.

As discussed previously, carbonate system variability remains high across all EGSL regions, reflecting a combination of natural fluctuations and potential signs of broader system shifts. Despite this underlying variability, spatial and vertical patterns in annual cumulative CO_2-driven stressor exceedance (Figure 25) reveal a pronounced gradient of vulnerability in 2024. These exceedances are defined by threshold values that mark ecologically and chemically significant boundaries. The cumulative exceedance of these thresholds across multiple indicators and depths serves as a diagnostic tool for identifying areas of heightened biological exposure to acidification and other types of CO_2-driven stressors. Thresholds are used here not as absolute limits, but as ecologically meaningful benchmarks translating complex chemical variability into biologically relevant risk indicators. This threshold-based approach aligns with recent planetary boundary assessments and ecological risk frameworks (Cornwall et al. 2024, Findlay et al. 2025, Sakschewski et al. 2025), which emphasize the practical value of clear inflection points for guiding management decisions and evaluating systemic vulnerability.

At one end of the spectrum, the Estuary emerges as a zone of extreme vulnerability, where all five stressor thresholds are exceeded at depth (Figure 25). Signs of ocean acidification begin to emerge around 50 m in the Estuary, marked by the onset of aragonite undersaturation; however, the 200 m horizon represents a critical zone, where all five CO_2-driven stressor thresholds are simultaneously exceeded for the first time. These conditions reflect a lockstep intensification of hypercapnia, impaired buffering capacity (CSVI), undersaturation of the carbonate minerals aragonite and calcite, and a greater potential for metabolic inhibition associated with low SIR. They also coincide with indicators of organic matter degradation in

deeper layers, aligning with recent observations of increased deoxygenation at depth reported by Blais et al. (2025). Together, such stressors may impose multiple overlapping physiological constraints on marine calcifiers as well as other CO_2-sensitive organisms.

Moving eastward, the Northwest Gulf presents a moderately vulnerable profile (Figure 25). The first signs of carbonate system deterioration emerge around 100 m, where aragonite undersaturation begins to appear. At 200 m, vulnerability intensifies: four stressor thresholds are exceeded, including hypercapnia and combined stressors related to altered carbonate formation and dissolution dynamics. In addition, the 2024 calcite undersaturation depth distribution in the Northwest Gulf exhibits a narrower interquartile range alongside a modest upward shift, suggesting a more uniform exposure of the water column to corrosive conditions. Nevertheless, the presence of relatively higher CSVI values suggests that some buffering capacity persists, partially tempering the severity of CO_2-driven impacts.

The Northeast Gulf and Centre Gulf exhibit relatively lower vulnerability compared to other regions, with only one or two stressor thresholds typically exceeded. However, their degree of exposure differs. In the Northeast Gulf, signs of acidification begin near 100 m, where aragonite undersaturation extends from mid-depth to the bottom. Hypercapnic conditions also emerge at 200 m, contributing to a moderate multi-stressor load in deeper layers. In contrast, the Centre Gulf shows a more limited stressor profile: while aragonite undersaturation is present from 100 m down to bottom waters, pCO_2 levels remain below the hypercapnia threshold in 2024, indicating comparatively lower vulnerability. Despite the reduced intensity of multi-stressor exposure, even partial threshold exceedance indicates biologically relevant impacts that warrant continued attention.

Finally, the Magdalen Shallows, characterized by shallower bathymetry and the lack of deep troughs, are not reached by the deep-water layers that dominate other regions (Figure 25). Their deepest waters remain within the more dynamic upper ocean, where mixing and ventilation are comparatively stronger. As a result, exposure to persistent CO_2-driven stressors is limited; in 2024, aragonite undersaturation is the only threshold exceeded in this region, occurring near ~100 m and near the bottom. Consequently, the Magdalen Shallows represent a zone of reduced multi-stressor exposure, with relatively buffered carbonate conditions. However, species-specific tolerances and limited vertical structure may constrain the relevance of this zone for deep-dwelling taxa, underscoring the need to interpret spatial vulnerability gradients through the lens of habitat specificity and biological accessibility.

This report establishes that enhanced ocean acidification, documented in other regions of the world's oceans (Cai et al. 2011, Lauvset et al. 2020, Fassbender et al. 2023), is also occurring in the deep waters of the EGSL. Long residence times, strong stratification, and limited ventilation promote the accumulation of remineralized CO_2, creating corrosive conditions and hypercapnia below the pycnocline. These stressor regimes have intensified since 2020, forming vertical gradients that may increase biological vulnerability. Although the drivers in estuarine and marginal seas differ from those in the open ocean, the outcome is similar: intensification of acidification below the pycnocline. In the global ocean, this process is primarily driven by the downward transport of anthropogenic dissolved inorganic carbon and respiration-derived CO_2 (Cai et al. 2011, Lauvset et al. 2020, Fassbender et al. 2023). By 2020, approximately 60% of subsurface waters from 50 m down to 200 m had entered the uncertainty range of the planetary boundary for ocean acidification (compared to 40% of surface waters), highlighting that subsurface layers are strongly affected (Findlay et al. 2025). Both regional and global evidence confirm that enhanced acidification below the pycnocline is a defining feature of the changing carbonate system.

In the EGSL, spatial and vertical gradients in CO_2-driven stressors may shape exposure patterns and influence biological vulnerability. These gradients complicate efforts to evaluate ecosystem resilience and predict species-level responses because physical, chemical, and biological processes interact across scales. Biological vulnerability spans multiple habitats, including benthic communities that include a diverse array of calcifying organisms, mollusks, bivalves, benthic foraminifera, crustaceans, echinoderms, cnidarians, and gastropods, that play key ecological roles and contribute to biogeochemical cycling (Steinhart 2023, Chamberland et al. 2025). Deeper pelagic layers support midwater and vertically migrating organisms, including invertebrates and numerous fish species, ranging from pelagic to demersal taxa, which sustain trophic connectivity, carbon flux, and, together with benthic taxa, underpin regional fisheries of commercial importance (Nozères et al. 2010, Bourdages et al. 2017, Bernier et al. 2023). Pelagic larval phases of many species link surface, midwater, and benthic habitats, reinforcing ecosystem connectivity (e.g., Ouellet and Saint-Marie 2018). This network's resilience depends partly on the integrity of deep-water habitats and the cohesion of carbonate system dynamics throughout the EGSL.

Anthropogenic climate and environmental change are reshaping marine ecosystems through warming, acidification, hypercapnia, and hypoxia, with these stressors interacting in complex, non-linear ways to affect aquatic life (Small et al. 2020, Collins et al. 2021, Huo et al. 2021a, Huo et al. 2023). They impose growing risks on mesopelagic ecosystems and fisheries, including those in the St. Lawrence Gulf and Estuary (Guscelli et al. 2023, Guitard et al. 2025), and generate cascading costs for food security and commercial fishing (Gruber 2011, Doney et al. 2012, Pörtner 2012, Baumann 2015, Baumann 2019, Barange et al. 2018, Frazão Santos et al. 2020). Experimental studies have shown that carbonate undersaturation can result in reduced net calcification rates (Figuerola et al. 2022), with early life stages particularly vulnerable to such stress (Waldbusser and Salisbury 2014, Small et al. 2015, Small et al. 2016, Dodd et al. 2020, Stiasny et al. 2021). In addition, non-calcifiers may experience physiological impairment under hypercapnic conditions through altered acid–base disruption and metabolic stress (Michaelidis et al. 2007, Spicer and Morley 2022). These physiological effects can scale up to affect key biological functions, potentially driving population-level shift and biodiversity changes (Sunday et al. 2017, Huo et al. 2018, Huo et al. 2021b). Species' responses vary widely across taxa and environments, shaped by genetic diversity, physiological plasticity, and local environmental context (Gaitán-Espitia et al. 2017a, Gaitán-Espitia et al. 2017b, Gaitán-Espitia et al. 2023, Alter et al. 2024). Such responses often involve energetic trade-offs, whereby energy diverted toward acid–base regulation or shell maintenance, may reduce resources available for other physiological functions such as growth, reproduction, or immune function (e.g., Schwaner et al. 2020). In dynamic environments such as estuaries and semi-enclosed seas, species are often exposed to strong regional gradients and may exhibit local adaptation (Vargas et al. 2022), yet shifting carbonate baselines can push conditions beyond historical exposure ranges. This underscores the need for integrated, multi-stressor research frameworks to understand how acidification, hypercapnia, warming, and hypoxia jointly affect marine species, ecological interactions, and ecosystem structure (Small et al. 2020, Beauchesne et al. 2025, Guscelli et al. 2023, Jian et al. 2025).

Building on this recognition, the findings presented in this report highlight the crucial role of long-term, multi-decadal observational programs for advancing our understanding of ocean acidification and other related CO_2-driven stressors. Such programs are indispensable for disentangling natural variability from anthropogenic trends, a priority consistently reaffirmed by the international scientific community (Bates et al. 2014, Hassoun et al. 2025). Sustained monitoring is also essential for ecosystem-based fisheries management, providing the

foundational data needed to assess exposure, evaluate vulnerability, and develop adaptive management strategies (e.g., Wright-Fairbanks et al. 2025). Deepening our grasp of the ecological consequences of OA and other CO_2-driven conditions requires high-resolution observations, experimental validation, and predictive modeling, supported by multidisciplinary collaboration across marine sciences.

5. KEY FINDINGS

This report documents acidification and CO_2-driven conditions observed in the Estuary and Gulf of St. Lawrence during 2024, in the context of ongoing fluctuations and trends in physical and biological conditions in the region. Surface and upper mixed layer carbonate chemistry is highly variable in the EGSL, shaped by short-term physical, chemical, and biological processes. Because surface water annual anomalies largely reflect local and episodic variability, reliable trend detection in upper layers of the water column will require longer-term records and contextualization; therefore, key findings focus on subsurface and deep-water conditions where signals are more persistent.

- In 2024, Rimouski Station exhibited intensified acidification and carbon accumulation, particularly in deep and bottom waters, with pCO_2 levels exceeding 1000 µatm from midsummer onward and record-low pH_T anomalies. Shoaling of saturation and stress thresholds (Ω_A, Ω_C, CSVI, SIR) may signal a compression of habitat for marine organisms and a shift towards more acidic conditions in the Estuary.

- Waters from the subsurface down to near-bottom depths in the EGSL exhibited near-normal to below-normal buffering capacity, as indicated by the carbonate system vulnerability index, with a distinct signal of below-normal anomalies at 200 m.

    - Notably, time series CSVI record lows are observed at 200 m at Rimouski Station, in the Estuary, Centre Gulf, and Northeast Gulf.

- Subsurface pH_T anomalies generally showed near-normal to below-normal conditions, except for an above-normal anomaly at the 100 m depth horizon in the Magdalen Shallows.

    - Notably, 2024 marked time-series record lows in the Estuary at 50 m, 100 m, 200 m, and near-bottom (tied with 2023), as well as at 200 m in the Centre Gulf (also tied with 2023).

- Subsurface pCO_2 anomalies across the EGSL generally showed near-normal to above-normal conditions. Exceptions to this overall distribution include below-normal anomalies at the 100 m depth horizon in the Magdalen Shallows and in near-bottom waters of the Northeast and Centre Gulf regions.

    - At the 200 m depth horizon, all deep regions exhibited hypercapnia, except the Centre Gulf, where pCO_2 remained narrowly below the 1000 µatm threshold.

    - Time-series record high pCO_2 annual means were observed in the Estuary at both 50 m and 200 m.

- Subsurface aragonite saturation state (Ω_A) anomalies across the EGSL generally showed near-normal to below-normal conditions, except for an above-normal anomaly at the 100 m depth horizon in the Magdalen Shallows, consistent with pH_T patterns.

  - Undersaturation of aragonite was prevalent in all regions in near-bottom waters and at depth horizons 100 m and deeper (when such depths are present). In the Centre Gulf at 100 m, Ω_A remained on the edge of undersaturation with a value of 1.

  - In the Estuary, the onset of aragonite undersaturation occurred at a shallower depth, around 50 m.

  - In 2024, time series Ω_A record lows were present at 50 m at Rimouski Station, at 100 m in the Northeast Gulf (tied with 2020), and at 200 m in all EGSL regions except the Northwest Gulf.

- Regional and depth-dependent subsurface anomalies in calcite saturation state (Ω_C) across the EGSL exhibited spatial patterns that mirror those observed for Ω_A.

  - Undersaturation of calcite was present at 200 m and 300 m in the Estuary and at 200 m in the Northwest Gulf.

  - In 2024, time series Ω_C record lows were present at 50 m at Rimouski Station, at 100 m in the Northeast Gulf, and at 200 m in all EGSL regions except the Northwest Gulf.

- Subsurface substrate-inhibitor ratio anomalies across the EGSL generally reflected near- to below-normal conditions, apart from an above-normal anomaly observed at the 100 m depth horizon in the Magdalen Shallows.

  - Annual 2024 values of SIR were below the threshold of 0.100 in the Estuary (at 200 m, 300 m, and bottom) and in the Northwest Gulf (at 200 m and 300 m).

  - The year 2024 marked time series SIR record lows in the Estuary, including Rimouski Station, at 50 m, as well as at 200 m in all EGSL regions except for the Northwest Gulf, with some of these records tied with previous low years.

- Since 2020 and continuing in 2024, the 200 m depth horizon stands out as a zone of generally sustained below-normal conditions in CSVI, pH_T, Ω_A, Ω_C, and SIR, alongside above-normal levels of pCO_2 and DIC, marking it as a key zone of carbonate system vulnerability across all regions intersected by deep channels.

- A regional gradient in annual average cumulative CO_2-driven stressor exceedance was present across the EGSL in 2024:

  - The Estuary showed the most severe multi-stressor vulnerability from 200 m to the bottom, where all five thresholds, CSVI, pCO_2, Ω_A, Ω_C, and SIR, were exceeded, with aragonite undersaturation present as shallow as 50 m.

  - The Northwest Gulf exhibited high vulnerability, particularly at 200 m, with four thresholds, pCO_2, Ω_A, Ω_C, and SIR, crossed at this depth.

  - The Northeast Gulf showed moderate vulnerability, with hypercapnia and aragonite undersaturation at 200 m.

- The Centre Gulf and Magdalen Shallows also showcase vulnerability but remained comparatively less affected overall, though aragonite undersaturation was present in bottom waters and at depths of 100 m.

ACKNOWLEDGEMENTS

The monitoring of data presented here is made possible thanks to the dedicated commitment of the employees participating in the Atlantic Zone Monitoring Program and the Aquatic Climate Change Adaptation Services Program of DFO (Félix St-Pierre, David Leblanc, Caroline Lafleur, Anthony Ouellet, Nicolas Coulombe, Sylvain Dubé, Guillaume Mercier, Myranda Blouin, Michel Rousseau, Véronique Desborbes, Marie-Noëlle Bourassa and Hélèna Talbot). We thank Claude Potvin, Aude Boivin-Rioux, and Renée Allain for the preparation, analysis and calibration of the CO_2-carbonate system data. We are grateful to Daniel Small and Tonya Burgers for reviewing the manuscript and providing insightful comments, and Jean-Luc Shaw as the technical report editor.

REFERENCES CITED

Allemand, D., Ferrier-Pagés, C., Furla, P., Houlbrèque, F., Puverel, S., Reynaud, S., Tambutté, É., Tambutté, S., and Zoccola, D. 2004. Biomineralisation in reef-building corals: from molecular mechanisms to environmental control. C. R. Palevol 3:453–467. https://doi.org/10.1016/j.crpv.2004.07.011

Alter, K., Jacquemont, J., Claudet, J., Lattuca, M.E., Barrantes, M.E., Marras, S., Manríquez, P.H., González, C.P., Fernández, D.A., Peck, M.A., Cattano, C., Milazzo, M., Mark, F.C., and Domenici, P. 2024. Hidden impacts of ocean warming and acidification on biological responses of marine animals revealed through meta-analysis. Nat. Commun. 15:2885. https://doi.org/10.1038/s41467-024-47064-3

Arroyo, M.C., Fassbender, A.J., Carter, B.R., Edwards, C.A., Fiechter, J., Norgaard, A., and Feely, R.A. 2022. Dissimilar sensitivities of ocean acidification metrics to anthropogenic carbon accumulation in the central North Pacific Ocean and California Current Large Marine Ecosystem. Geophys. Res. Lett. 49(15):e2022GL097835. https://doi.org/10.1029/2022GL097835

Bach, L.T. 2015. Reconsidering the role of carbonate ion concentration in calcification by marine organisms. Biogeosciences 12:4939–4951. https://doi.org/10.5194/bg-12-4939-2015

Barange, M., Bahri, T., Beveridge, M.C.M., Cochrane, K.L., Funge-Smith, S., and Poulain, F. (eds.). 2018. Impacts of climate change on fisheries and aquaculture: synthesis of current knowledge, adaptation and mitigation options. FAO Fish. Aquac. Tech. Pap. 627. Rome: FAO. 628 p.

Bates, N.R., Astor, Y.M., Church, M.J., Currie, K., Dore, J.E., González-Dávila, M., Lorenzoni, L., Muller-Karger, F., Olafsson, J., and Santana-Casiano, J.M. 2014. A time-series view of changing ocean chemistry due to ocean uptake of anthropogenic CO_2 and ocean acidification. Oceanography 27(1):126–141. https://doi.org/10.5670/oceanog.2014.16

Baumann, H., Wallace, R.B., Tagliaferri, T., and Gobler, C.J. 2015. Large natural pH, CO_2, and O2 fluctuations in a temperate tidal salt marsh on diel, seasonal, and interannual time scales. Estuaries Coasts 38:220–231. https://doi.org/10.1007/s12237-014-9800-y

Baumann, H. 2019. Experimental assessments of marine species sensitivities to ocean acidification and co-stressors: how far have we come? Can. J. Zool. 97(5):399–408. https://doi.org/10.1139/cjz-2018-0198

Beauchesne, D., Cazelles, K., Daigle, R.M., Gravel, D., and Archambault, P. 2025. Ecological interactions amplify cumulative effects in marine ecosystems. Sci. Adv. 11(4):eade09315. https://doi.org/10.1126/sciadv.adp9315

Bednaršek, N., Feely, R.A., Howes, E.L., Hunt, B.P.V., Kessouri, F., León, P., Lischka, S., Maas, A.E., McLaughlin, K., Nezlin, N.P., Sutula, M., and Weisberg, S.B. 2019. Systematic review and meta-analysis toward synthesis of thresholds of ocean acidification impacts on calcifying pteropods and interactions with warming. Front. Mar. Sci. 6:227. https://doi.org/10.3389/fmars.2019.00227

Bernier, R.Y., Jamieson, R.E., Kelly, N.E., Lafleur, C., and Moore, A.M. (eds.). 2023. State of the Atlantic Ocean: synthesis report. Can. Tech. Rep. Fish. Aquat. Sci. 3544: v+219 p.

Blais, M., Galbraith, P.S., Lizotte, M., Clay, S.A., and Starr, M. 2024. Chemical and biological oceanographic conditions in the Estuary and Gulf of St. Lawrence during 2023. Can. Tech. Rep. Hydrogr. Ocean Sci. 385: v+84 p.

Blais, M., Clay, S.A., Galbraith, P.S., and Starr, M. 2025. Chemical and biological oceanographic conditions in the Gulf of St. Lawrence during 2024. Can. Tech. Rep. Hydrogr. Ocean Sci. 405: vi+87 p. https://doi.org/10.60825/gmbq-jf70

Borges, A.V., and Gypens, N. 2010. Carbonate chemistry in the coastal zone responds more strongly to eutrophication than ocean acidification. Limnol. Oceanogr. 55(1):346–353.

Bourdages, H., Brassard, C., Desgagnés, M., Galbraith, P., Gauthier, J., Légaré, B., Nozères, C., and Parent, E. 2017. Preliminary results from the groundfish and shrimp multidisciplinary survey in August 2016 in the Estuary and northern Gulf of St. Lawrence. DFO Can. Sci. Advis. Sec. Res. Doc. 2017/002. v+87 p.

Bugden, G.L. 1991. Changes in the temperature–salinity characteristics of the deeper waters of the Gulf of St. Lawrence over the past several decades. In Therriault, J.-C. (ed.). The Gulf of St. Lawrence: small ocean or big estuary? Can. Spec. Publ. Fish. Aquat. Sci. 113:139–147.

Cai, W.-J., Hu, X., Huang, W.-J., Murrell, M.C., Lehrter, J.C., Lohrenz, S.E., Chou, W.-C., Zhai, W., Hollibaugh, J., Wang, Y., Zhao, P., Guo, X., Gundersen, K., Dai, M., and Gong, G.-C. 2011. Acidification of subsurface coastal waters enhanced by eutrophication. Nat. Geosci. 4:766–770. https://doi.org/10.1038/ngeo1297

Cai, W.-J., Huang, W.-J., Luther III, G.W., Pierrot, D., Li, M., Testa, J., Xue, M., Joesoef, A., Mann, R., Brodeur, J., Xu, Y.-Y., Chen, B., Hussain, N., Waldbusser, G.G., Cornwell, J., and Kemp, M.W. 2017. Redox reactions and weak buffering capacity lead to acidification in the Chesapeake Bay. Nat. Commun. 8:369. https://doi.org/10.1038/s41467-017-00417-7

Cai, W.-J., Feely, R.A., Testa, J.M., Li, M., Evans, W., Alin, S.R., Xu, Y.-Y., Pelletier, G., Ahmed, A., Greeley, D.J., Newton, J.A., and Bednaršek, N. 2021. Natural and anthropogenic drivers of acidification in large estuaries. Annu. Rev. Mar. Sci. 13:23–55. https://doi.org/10.1146/annurev-marine-010419-011004

Caldeira, K., and Wickett, M. 2003. Anthropogenic carbon and ocean pH. Nature 425:365. https://doi.org/10.1038/425365a

Carstensen, J., and Duarte, C.M. 2019. Drivers of pH variability in coastal ecosystems. Environ. Sci. Technol. 53:4020–4029. https://doi.org/10.1021/acs.est.8b03655

Chabot, D., and Gilbert, D. 2013. Description of the Atlantic Large Aquatic Basin as a habitat for marine fish and invertebrates. In Shackell, N.L., Greenan, B.J.W., Pepin, P., Chabot, D., and Warburton, A. (eds.). Climate change impacts, vulnerabilities and opportunities analysis of the Marine Atlantic Basin. Can. Manuscr. Rep. Fish. Aquat. Sci. 3012:1–15.

Chamberland, J.-M., Bourdages, H., Desgagnés, M., Galbraith, P., Isabel, L., Ouellette-Plante, J., Roux, M.-J., Scallon-Chouinard, P.-M., and Senay, C. 2025. Preliminary results from the 2024 August ecosystemic survey in the Estuary and northern Gulf of St. Lawrence. DFO Can. Sci. Advis. Sec. Res. Doc. 2025/032. iv+101 p.

Chan, F., Barth, J.A., Blanchette, C.A., Byrne, R.H., Chavez, F., Cheriton, O., Feely, R.A., Friederich, G., Gaylord, B., Gouhier, B., Hacker, S., Hill, T., Hofmann, G., McManus, M.A., Menge, B.A., Nielsen, K.J., Russell, A., Sanford, E., Sevadjian, J., and Washburn, L. 2017. Persistent spatial structuring of coastal ocean acidification in the California Current System. Sci. Rep. 7:2526. https://doi.org/10.1038/s41598-017-02777-y

Chan, F., Barth, J.A., Kroeker, K.J., Lubchenco, J., and Menge, B.A. 2019. The dynamics and impact of ocean acidification and hypoxia: insights from sustained investigations in the Northern California Current Large Marine Ecosystem. Oceanography 32(3):62–71. https://doi.org/10.5670/oceanog.2019.312

Chen, J., Glibert, P.M., Cai, W.-J., and Huang, D. 2023. Editorial: eutrophication, algal bloom, hypoxia and ocean acidification in large river estuaries, volume II. Front. Mar. Sci. 10:1225903. https://doi.org/10.3389/fmars.2023.1225903

Clayton, T.D., and Byrne, R.H. 1993. Spectrophotometric seawater pH measurements: total hydrogen ion concentration scale calibration of m-cresol purple and at-sea results. Deep Sea Res. Part I Oceanogr. Res. Pap. 40(10):2115–2129. https://doi.org/10.1016/0967-0637(93)90048-8

Clements, J.C., and Hunt, H.L. 2015. Marine animal behaviour in a high CO_2 ocean. Mar. Ecol. Prog. Ser. 536:259–279. https://doi.org/10.3354/meps11426

Collins, M., Truebano, M., Verbeke, W.C.E.P., and Spicer, J.I. 2021. Do aquatic ectotherms perform better under hypoxia after warm acclimation? J. Exp. Biol. 224:jeb232512. https://doi.org/10.1242/jeb.232512

Cornwall, C.E., Comeau, S., and Harvey, B.P. 2024. Are physiological and ecosystem-level tipping points caused by ocean acidification? A critical evaluation. Earth Syst. Dynam. 15(3):671–687. https://doi.org/10.5194/esd-15-671-2024

Cyr, F., Bourgault, D., and Galbraith, P.S. 2011. Interior versus boundary mixing of a cold intermediate layer. J. Geophys. Res. Oceans 116:C07029. https://doi.org/10.1029/2011JC007359

Cyronak, T., Schulz, K.G., and Jokiel, P.L. 2016. The omega myth: what really drives lower calcification rates in an acidifying ocean. ICES J. Mar. Sci. 73(3):558–562. https://doi.org/10.1093/icesjms/fsv075

DeVries, T. 2014. The oceanic anthropogenic CO_2 sink: storage, air–sea fluxes, and transports over the industrial era. Global Biogeochem. Cycles 28:631–647. https://doi.org/10.1002/2013GB004739

Dickson, A.G. 1990. Standard potential of the reaction AgCl(s) + 1/2 H2(g) = Ag(s) + HCl(aq), and the standard acidity constant of the ion HSO_4^- in synthetic seawater from 273.15 to 318.15 K. J. Chem. Thermodyn. 22(2):113–127. https://doi.org/10.1016/0021-9614(90)90074-Z

Dickson, A.G. 2010. Standards for ocean measurements. Oceanography 23(3):34–47. https://doi.org/10.5670/oceanog.2010.22

Dickson, A.G., and Riley, J.P. 1979. The estimation of acid dissociation constants in seawater media from potentiometric titrations with strong base. Mar. Chem. 7(2):89–99. https://doi.org/10.1016/0304-4203(79)90001-X

Dickson, A.G., Sabine, C.L., and Christian, J.R. (eds.). 2007. Guide to best practices for ocean CO_2 measurements. PICES Spec. Publ. 3. 191 p.

Dixson, D.L., Munday, P.L., and Jones, G.P. 2010. Ocean acidification disrupts the innate ability of fish to detect predator olfactory cues. Ecol. Lett. 13(1):68–75. https://doi.org/10.1111/j.1461-0248.2009.01400.x

Dixson, D.L., Jennings, A.R., Atema, J., and Munday, P.L. 2015. Odor tracking in sharks is reduced under ocean acidification conditions. Glob. Change Biol. 21:1454–1462. https://doi.org/10.1111/gcb.12678

Dodd, L. F., Grabowski, J. H., Piehler, M. F., and Westfield, I. 2020. Ocean acidification impairs crab larval development and survival. Mar. Environ. Res. 159:104948. https://doi.org/10.1016/j.marenvres.2020.104948

Doney, S.C., Fabry, V.J., Feely, R.A., and Kleypas, J.A. 2009. Ocean Acidification: The Other CO_2 Problem. Annu. Rev. Mar. Sci. 1:169–192. https://doi.org/10.1146/annurev.marine.010908.163834

Doney, S.C., Ruckelshaus, M., Duffy, J.E., Barry, J.P., Chan, F., English, C.A., Galindo, H.M., Grebmeier, J.M., Hollowed, A.B., Knowlton, N., Polovina, J., Rabalais, N.N., Sydeman, W.J., and Talley, L.D. 2012. Climate Change Impacts on Marine Ecosystems. Annu. Rev. Mar. Sci. 4:11–37. https://doi.org/10.1146/annurev-marine-041911-111611

Doney, S.C., Busch, D.S., Cooley, S.R., and Kroeker, K.J. 2020. The Impacts of Ocean Acidification on Marine Ecosystems and Reliant Human Communities. Annu. Rev. Environ. Resour. 45:83–112. https://doi.org/10.1146/annurev-environ-012320-083019

European Environment Agency (EEA). 2024. Ocean acidification. Indicators. https://www.eea.europa.eu/en/analysis/indicators/ocean-acidification

Egleston, E.S., Sabine, C.L., and Morel, F.M.M. 2010. Revelle revisited: Buffer factors that quantify response of ocean chemistry to changes in DIC and alkalinity. Global Biogeochem. Cy. 24:9 p. https://doi.org/10.1029/2008GB003407

El-Sabh, M.I., and Silverberg, N. 1990. Chapter 1, The St. Lawrence Estuary: Introduction. Oceanography of a Large-Scale Estuarine System, Vol. 39. https://doi.org/10.1002/9781118663783.ch1

Emerson, S., and Hedges, J. 2008. Chemical oceanography and the marine carbon cycle. Cambridge University Press, New York. 453 p. https://doi.org/10.1017/CBO9780511793202

Fabry, V.J., Seibel, B.A., Feely, R.A., and Orr, J.C. 2008. Impacts of ocean acidification on marine fauna and ecosystem processes. ICES J. Mar. Sci. 65(3):414–432. https://doi.org/10.1093/icesjms/fsn048

Fassbender, A.J., Carter, B.R., Sharp, J.D., Huang, Y., Arroyo, M.C., and Frenzel, H. 2023. Amplified subsurface signals of ocean acidification. Global Biogeochem. Cy. 37(12):14 p. https://doi.org/10.1029/2023GB007843

Feely, R.A., Sabine, C.L., Lee, K., Berelson, W., Kleypas, J., Fabry, V.J., and Millero, F.J. 2004. Impact of Anthropogenic CO_2 on the $CaCO_3$ System in the Oceans. Science 305:362–366. https://doi.org/10.1126/science.1097329

Feely, R.A., Sabine, C.L., Hernandez-Ayon, J.M., Ianson, D., and Hales, B. 2008. Evidence for Upwelling of Corrosive "Acidified" Water onto the Continental Shelf. Science 320:1490–1492. https://doi.org/10.1126/science.1155676

Feely, R.A., Alin, S.R., Carter, B., Bednarsek, N., Hales, B., Chan, F., Hill, T.M., Gaylord, B., Sanford, E., Byrne, R.H., Sabine, C.L., Greeley, D., and Juranek, L. 2016. Chemical and biological impacts of ocean acidification along the west coast of North America. Estuar. Coast. Shelf Sci. 183:260–270. http://dx.doi.org/10.1016/j.ecss.2016.08.043

Feely, R.A., Okazaki, R.R., Cai, W.-J., Bednarsek, N., Alin, S.R., Byrne, R.H., and Fassbender, A. 2018. The combined effects of acidification and hypoxia on pH and aragonite saturation in the coastal waters of the California current ecosystem and the northern Gulf of Mexico. Cont. Shelf Res. 152:50–60. https://doi.org/10.1016/j.csr.2017.11.002

Figuerola, B., Hancock, A. M., Stark, J. S., and King, C. K. 2021. A review and meta-analysis of potential impacts of ocean acidification on marine calcifiers from the Southern Ocean. Front. Mar. Sci. 8:584445. https://doi.org/10.3389/fmars.2021.584445

Figuerola, B., Griffiths, H.J., Krzeminska, M., Piwoni-Piorewicz, A., Iglikowska, A., and Kuklinski, P. 2022. Temperature as a likely driver shaping global patterns in mineralogical composition in bryozoans: implications for marine calcifiers under global change. Ecography e06381, 14 p. https://doi.org/10.1111/ecog.06381

Findlay, S.F., Feely, R.A., Jiang, L.-Q., Pelletier, G., and Bednaršek, N. 2025. Ocean Acidification: Another Planetary Boundary Crossed. Glob. Chang. Biol. 17p. https://doi.org/10.1111/gcb.70238

Frankignoulle, M., Canon, C., and Gattuso, J.-P. 1994. Marine calcification as a source of carbon dioxide: Positive feedback of increasing atmospheric CO_2. Limnol. Oceanogr. 39(2):458–462. https://doi.org/10.4319/lo.1994.39.2.0458

Frazão Santos, C., Agardy, T., Andrade, F., Calado, H., Crowder, L.B., Ehler, C.N., García-Morales, S., Gissi, E., Halpern, B.S., Orbach, M.K., Pötner, H.-O., and Rosa, R. 2020. Integrating climate change in ocean planning. Nat. Sustain. 3:505–516. https://doi.org/10.1038/s41893-020-0513-x

Gaitán-Espitia, J.D., Marshall, D., Dupont, S., Bacigalupe, L.D., Bodrossy, L., and Hobday, A.J. 2017a. Geographical gradients in selection can reveal genetic constraints for evolutionary responses to ocean acidification. Biol. Lett. 13:20160784. https://doi.org/10.1098/rsbl.2016.0784

Gaitán-Espitia, J.D., Villanueva, P.A., Lopez, J., Torres, R., Navarro, J.M., and Bacigalupe, L.D. 2017b. Spatio-temporal environmental variation mediates geographical differences in phenotypic responses to ocean acidification. Biol. Lett. 13:20160865. https://doi.org/10.1098/rsbl.2016.0865

Gaitán-Espitia, J.D., Vargas, C.A., and Hofmann, G.E. 2023. Phenotypic plasticity and physiological tolerance shape marine organisms' responses to climate change. Front. Mar. Sci. 10:1231099. https://doi.org/10.3389/fmars.2023.1231099

Galbraith, P.S. 2006. Winter water masses in the Gulf of St. Lawrence. J. Geophys. Res. Oceans 111:C06022. https://doi.org/10.1029/2005JC003159

Galbraith, P.S., Blais, M., Lizotte, M., Cyr, F., Bélanger, D., Casault, B., Clay, S., Layton, C., Starr, M., Chassé, J., Azetsu-Scott, K., Coyne, J., Devred, E., Gabriel, C.-E., Johnson, C.L., Maillet, G., Pepin, P., Plourde, S., Ringuette, M., and Shaw, J.-L. 2024. Oceanographic conditions in the Atlantic zone in 2023. Can. Tech. Rep. Hydrogr. Ocean Sci. 379: v+38 p.

Galbraith, P.S., Lizotte, M., Blais, M., Bélanger, D., Casault, B., Coyne, J., Layton, C., Azetsu-Scott, K., Beazley, L., Chassé, J., Clay, S., Cyr, F., Devred, E., Fudge, A., Gabriel, C.-E., Greenan, B., Hébert, A.-J., Johnson, C.L., Maillet, G., Penney, J., Rastin, S., Ringuette, M., Shaw, J.-L., Snook, S., and Starr, M. 2025a. Oceanographic conditions in the Atlantic zone in 2024. Can. Tech. Rep. Hydrogr. Ocean Sci. 400: viii+49 p. https://doi.org/10.60825/e92v-d229

Galbraith, P.S., Chassé, J., Shaw, J.-L., Lefaivre, D., and Bourassa, M.-N. 2025b. Physical oceanographic conditions in the Gulf of St. Lawrence during 2024. Can. Tech. Rep. Hydrogr. Ocean Sci. 397: v+95 p. https://doi.org/10.60825/eznq-0815

Gattuso, J.-P., Epitalon, J.-M., Lavigne, H., Orr, J., Gentili, B., Hagens, M., Hofmann, A., Mueller, J.-D., Proye, A., Rae, J., and Soetaert, K. 2024. seacarb: seawater carbonate chemistry, version 3.3.3. https://doi.org/10.32614/CRAN.package.seacarb

Gattuso, J.-P., Frankignoulle, M., and Wollast, R. 1998. Carbon and carbonate metabolism in coastal aquatic ecosystems. Annu. Rev. Ecol. Syst. 29:405–434. https://doi.org/10.1146/annurev.ecolsys.29.1.405

Gattuso, J.-P., and Hansson, L. 2020. Ocean acidification. Oxford University Press, Oxford. xix+326 p.

Gazeau, F., Parker, L.M., Comeau, S., Gattuso, J.-P., O'Connor, W.A., Martin, S., Pörtner, H.-O., and Ross, P.M. 2013. Impacts of ocean acidification on marine shelled molluscs. Mar. Biol. 160:2207–2245. https://doi.org/10.1007/s00227-013-2219-3

Gehlen, M., Gruber, N., Gangsto, R., Bopp, L., and Oschlies, A. 2011. Biogeochemical consequences of ocean acidification and feedbacks to the Earth system. In Gattuso, J.-P., and Hansson, L. (eds.). Ocean acidification. https://doi.org/10.1093/oso/9780199591091.003.0017

Genovesi, L., de Vernal, A., Thibodeau, B., Hilaire-Marcel, C., Mucci, A., and Gilbert, D. 2011. Recent changes in bottom water oxygenation and temperature in the Gulf of St. Lawrence: micropaleontological and geochemical evidence. Limnol. Oceanogr. 56(4):1319–1329. https://doi.org/10.4319/lo.2011.56.4.1319

Gibb, O., Cyr, F., Azetsu-Scott, K., Chassé, J., Childs, D., Gabriel, C.-E., Galbraith, P.S., Maillet, G., Pepin, P., Punshon, S., and Starr, M. 2023. Spatiotemporal variability in pH and carbonate parameters on the Canadian Atlantic continental shelf between 2014 and 2022. Earth Syst. Sci. Data 15:4127–4162. https://doi.org/10.5194/essd-15-4127-2023

Gilbert, D., and Pettigrew, B. 1997. Interannual variability (1948–1994) of the CIL core temperature in the Gulf of St. Lawrence. Can. J. Fish. Aquat. Sci. 54(S1):57–67. https://doi.org/10.1139/f96-160

Gilbert, D., Sundby, B., Gobeil, C., Mucci, A., and Tremblay, G.-H. 2005. A seventy-two-year record of diminishing deep-water oxygen in the St. Lawrence Estuary: the northwest Atlantic connection. Limnol. Oceanogr. 50(5):1654–1666. https://doi.org/10.4319/lo.2005.50.5.1654

Gruber, N. 2011. Warming up, turning sour, losing breath: ocean biogeochemistry under global change. Philos. Trans. R. Soc. A 369(1943):1980–1996. https://doi.org/10.1098/rsta.2011.0003

Gruber, N., Clement, D., Carter, B.R., Feely, R.A., van Heuven, S., Hoppema, M., Ishii, M., Key, R.M., Kozyr, A., Lauvset, S.K., Monaco, C.L., Mathis, J.T., Murata, A., Olsen, A., Pérez, F.F., Sabine, C.L., Tanhua, T., and Wanninkhof, R. 2019. The oceanic sink for anthropogenic CO_2 from 1994 to 2007. Science 363:1193–1199. https://doi.org/10.1126/science.aau5153

Gruber, N., Bakker, D.C.E., DeVries, T., Gregor, L., Hauck, J., Landschützer, P., McKinley, G.A., and Müller, J.D. 2023. Trends and variability in the ocean carbon sink. Nat. Rev. Earth Environ. 4:119–134. https://doi.org/10.1038/s43017-022-00381-x

Guitard, J.J., Chabot, D., Senay, C., Robert, D., and Deslauriers, D. 2025. Warming, but not acidification, increases metabolism and reduces growth of redfish (Sebastes fasciatus) in the Gulf of St. Lawrence. Can. J. Zool. 103:1–18. https://doi.org/10.1139/cjz-2025-0014

Guscelli, E., Noisette, F., Chabot, D., Blier, P.U., Hansen, T., Cassista-Da Ros, M., Pepin, P., Skanes, K.R., and Calosi, P. 2023. Northern shrimp from multiple origins show similar sensitivity to global change drivers, but different cellular energetic capacity. J. Exp. Biol. 226(16):jeb245400. https://doi.org/10.1242/jeb.245400

Hall, N.S., Testa, J.M., Li, M., and Paerl, H.W. 2023. Assessing drivers of estuarine pH: a comparative analysis of the continental U.S.A.'s two largest estuaries. Limnol. Oceanogr. 68:2227–2244. https://doi.org/10.1002/lno.12418

Hassoun, A.E.R., Sutton, A., Dupont, S., Guo, X., and Hernandez-Ayon, J.M. 2025. Editorial: Time-series observations of ocean acidification: a key tool for documenting impacts on a changing planet. Front. Mar. Sci. 12:1581134. https://doi.org/10.3389/fmars.2025.1581134

Hönisch, B., Ridgwell, A., Schmidt, D.N., Thomas, E., Gibbs, S.J., Sluijs, A., Zeebe, R., Kump, L., Martindale, R.C., Greene, S.E., Kiessling, W., Ries, J., Zachos, J.C., Royer, D.L., Barker, S., Marchitto, T.M., Moyer, R., Pelejero, C., Ziveri, P., Foster, G.L., and Williams, B. 2012. The geological record of ocean acidification. Science 335:1058–1063. https://doi.org/10.1126/science.1208277

Hu, X. 2020. Effect of organic alkalinity on seawater buffer capacity: a numerical exploration. Aquat. Geochem. 26:161–178. https://doi.org/10.1007/s10498-020-09375-x

Huo, D., Sun, L., Ru, X., Zhang, L., Lin, C., Liu, S., Xin, X., and Yang, H. 2018. Impact of hypoxia stress on the physiological responses of sea cucumber Apostichopus japonicus: respiration, digestion, immunity and oxidative damage. PeerJ 6:e4651. https://doi.org/10.7717/peerj.4651

Huo, D., Sun, L., Sun, J., Zhang, L., Liu, S., Su, F., and Yang, H. 2021a. Sea cucumbers in a high temperature and low dissolved oxygen world: roles of miRNAs in the regulation of environmental stresses. Environ. Pollut. 268:115509. https://doi.org/10.1016/j.envpol.2020.115509

Huo, D., Sun, L., Sun, J., Lin, C., Liu, S., Zhang, L., and Yang, H. 2021b. Emerging roles of circRNAs in regulating thermal and hypoxic stresses in Apostichopus japonicus (Echinodermata: Holothuroidea). Ecotoxicol. Environ. Saf. 228:112994. https://doi.org/10.1016/j.ecoenv.2021.112994

Huo, D., Gaitán-Espitia, J.D., Spicer, J.I., and Yang, H. 2023. Editorial: the adaptation and response of aquatic animals in the context of global climate change. Front. Mar. Sci. 10:1231099. https://doi.org/10.3389/fmars.2023.1231099

IPBES. 2019. Summary for policymakers of the global assessment report on biodiversity and ecosystem services of the Intergovernmental Science-Policy Platform on Biodiversity and Ecosystem Services. IPBES secretariat, Bonn, Germany. 56 p. https://doi.org/10.5281/zenodo.3553579

Jian, Z., Zhong, M., Li, R., Su, H., Rao, Q., Wang, Y., Wang, C., Sun, S., Chen, J., and Xie, P. 2025. Warming enhances the effects of acidification on aquatic biota: a global meta-analysis. Glob. Ecol. Biogeogr. 34:e70080. https://doi.org/10.1111/geb.70080

Johnson, K.M., Wills, K.D., Butler, D.B., Johnson, W.K., and Wong, C.S. 1993. Coulometric total carbon dioxide analysis for marine studies: maximizing the performance of an automated gas extraction system and coulometric detector. Mar. Chem. 44(2–4):167–187. https://doi.org/10.1016/0304-4203(93)90201-X

Jokiel, P.L. 2011. Ocean acidification and control of reef coral calcification by boundary layer limitation of proton flux. Bull. Mar. Sci. 87(3):639–657. https://doi.org/10.5343/bms.2010.1107

Jokiel, P.L. 2013. Coral reef calcification: carbonate, bicarbonate and proton flux under conditions of increasing ocean acidification. Proc. R. Soc. B 280(1764):20130031. https://doi.org/10.1098/rspb.2013.0031

Jutras, M., Mucci, A., Chaillou, G., Nesbitt, W.A., and Wallace, D.W.R. 2023. Temporal and spatial evolution of bottom-water hypoxia in the St Lawrence estuarine system. Biogeosciences 20:839–849. https://doi.org/10.5194/bg-20-839-2023

Kahil, K., Weiner, S., Addadi, L., and Gal, A. 2021. Ion pathways in biomineralization: perspectives on uptake, transport, and deposition of calcium, carbonate, and phosphate. J. Am. Chem. Soc. 143(50):21100–21112. https://doi.org/10.1021/jacs.1c09174

Keppel, E.A., Scrosati, R.A., and Courtenay, S.C. 2012. Ocean acidification decreases growth and development in American lobster (Homarus americanus) larvae. J. Northw. Atl. Fish. Sci. 44:61–66. https://doi.org/10.2960/J.v44.m683

Kerr, D.E., Brown, P.J., Grey, A., and Kelleher, B.P. 2021. The influence of organic alkalinity on the carbonate system in coastal waters. Mar. Chem. 237:104050. https://doi.org/10.1016/j.marchem.2021.104050

Kessouri, F., McWilliams, J.C., Bianchi, D., Sutula, M., Renault, L., Deutsch, C., Feely, R.A., McLaughlin, K., Ho, M., Howard, E.M., Bednaršek, N., Damien, P., Molemaker, J., and Weisberg, S.B. 2021. Coastal eutrophication drives acidification, oxygen loss, and ecosystem change in a major oceanic upwelling system. Proc. Natl. Acad. Sci. U.S.A. 118(21):e2018856118. https://doi.org/10.1073/pnas.2018856118

Khatiwala, S., Primeau, F., and Hall, T. 2009. Reconstruction of the history of anthropogenic CO_2 concentrations in the ocean. Nature 462:346–349. https://doi.org/10.1038/nature08526

Kroeker, K.J., Kordas, R.L., Crim, R.N., and Singh, G.G. 2010. Meta-analysis reveals negative yet variable effects of ocean acidification on marine organisms. Ecol. Lett. 13(11):1419–1434. https://doi.org/10.1111/j.1461-0248.2010.01518.x

Lauvset, S.K., Gruber, N., Landschützer, P., Olsen, A., and Tjiputra, J. 2015. Trends and drivers in global surface ocean pH over the past three decades. Biogeosciences 12:1285–1298. https://doi.org/10.5194/bg-12-1285-2015

Lauvset, S.K., Carter, B.R., Pérez, F.F., Feely, R.A., Velo, A., and Olsen, A. 2020. Processes driving global interior ocean pH distribution. Global Biogeochem. Cycles 34(1):e2019GB006229. https://doi.org/10.1029/2019GB006229

Lavoie, D., Lambert, N., Rousseau, S., Dumas, J., Chassé, J., Long, Z., Perrie, W., Starr, M., Brickman, D., and Azetsu-Scott, K. 2020. Projections of future physical and biochemical conditions in the Gulf of St. Lawrence, on the Scotian Shelf and in the Gulf of Maine using a regional climate model. Can. Tech. Rep. Hydrogr. Ocean Sci. 334: xiii+102 p.

Lavoie, D., Lambert, N., Starr, M., Chassé, J., Riche, O., Le Clainche, Y., Azetsu-Scott, K., Béjaoui, B., Christian, J.R., and Gilbert, D. 2021. The Gulf of St. Lawrence Biogeochemical Model: a modelling tool for fisheries and ocean management. Front. Mar. Sci. 8:732269. https://doi.org/10.3389/fmars.2021.732269

Lee, K., Kim, T.-W., Byrne, R.H., Millero, F.J., Feely, R.A., and Liu, Y.-M. 2010. The universal ratio of boron to chlorinity for the North Pacific and North Atlantic oceans. Geochim. Cosmochim. Acta 74(6):1801–1811. https://doi.org/10.1016/j.gca.2009.12.027

Leung, J.Y.S., Zhang, S., and Connell, S.D. 2022. Is ocean acidification really a threat to marine calcifiers? A systematic review and meta-analysis of 980+ studies spanning two decades. Small 18(35):e2107407. https://doi.org/10.1002/smll.202107407

Li, L., Chen, B., Luo, Y., Xia, J., and Qi, D. 2022. Factors controlling acidification in intermediate and deep/bottom layers of the Japan/East Sea. J. Geophys. Res. Oceans 127:e2021JC017712. https://doi.org/10.1029/2021JC017712

Li, M., Guo, Y., Cai, W.-J., Testa, J.M., Shen, C., Li, R., and Su, J. 2023. Projected increase in carbon dioxide drawdown and acidification in large estuaries under climate change. Commun. Earth Environ. 4:68. https://doi.org/10.1038/s43247-023-00733-5

Li, M., Li, R., Guo, Y., Testa, J.M., Cai, W.-J., Shen, C., Chen, Y., and Kaushal, S.S. 2025. Disentangling the effects of global and regional drivers on diverse long-term pH trends in coastal waters. AGU Adv. 6:e2024AV001350. https://doi.org/10.1029/2024AV001350

Long, W.C., Swiney, K.M., Harris, C., Page, H.N., and Foy, R.J. 2016. Effects of ocean acidification on juvenile red king crab (Paralithodes camtschaticus) and Tanner crab (Chionoecetes bairdi) growth, condition, calcification, and survival. ICES J. Mar. Sci. 73(3):716–726. https://doi.org/10.1093/icesjms/fsv205

Lueker, T.J., Dickson, A.G., and Keeling, C.D. 2000. Ocean pCO_2 calculated from dissolved inorganic carbon, alkalinity, and equations for K1 and K2: validation based on laboratory measurements of CO2 in gas and seawater at equilibrium. Mar. Chem. 70(1–3):105–119. https://doi.org/10.1016/S0304-4203(00)00022-0

Mackinder, L., Wheeler, G., Schroeder, D., Riebesell, U., and Brownlee, C. 2010. Molecular mechanisms underlying calcification in coccolithophores. Geomicrobiol. J. 27:585–595. https://doi.org/10.1080/01490451003703014

Majdisova, Z., and Skala, V. 2017. Radial basis function approximations: comparison and applications. Appl. Math. Model. 51:728–743. https://doi.org/10.1016/j.apm.2017.07.033

Mann, S. 2001. Biomineralization: principles and concepts in bioinorganic materials chemistry. Oxford University Press, New York. https://doi.org/10.1093/oso/9780198508823.001.0001

Martínez-Trejo, J.A., Cardoso-Mohedano, J.G., Sanchez-Cabeza, J.A., Ayón, J.M.H., Ruiz-Fernández, A.C., Gómez-Ponce, M.A., Barranco, L., and Pech, D. 2024. Variability of dissolved inorganic carbon in the most extensive karst estuarine–lagoon system of the southern Gulf of Mexico. Estuaries Coasts 47:2573–2588. https://doi.org/10.1007/s12237-024-01384-1

McNeil, B., and Sasse, T. 2016. Future ocean hypercapnia driven by anthropogenic amplification of the natural CO_2 cycle. Nature 529:383–386. https://doi.org/10.1038/nature16156

Melzner, F., Mark, F.C., Seibel, B.A., and Tomanek, L. 2020. Ocean acidification and coastal marine invertebrates: tracking CO2 effects from seawater to cell. Annu. Rev. Mar. Sci. 12:499–523. https://doi.org/10.1146/annurev-marine-010419-010658

Michaelidis, B., Spring, A., and Pörtner, H.-O. 2007. Effects of long-term acclimation to environmental hypercapnia on the physiology of the Mediterranean fish Sparus aurata. Mar. Biol. 150(6):1417–1429. https://doi.org/10.1007/s00227-006-0390-5

Middelburg, J.J., Soetaert, K., and Hagens, M. 2020. Ocean alkalinity, buffering and biogeochemical processes. Rev. Geophys. 58(3):e2019RG000681. https://doi.org/10.1029/2019RG000681

Millero, F.J. 1986. The pH of estuarine waters. Limnol. Oceanogr. 31(4):839–847. https://doi.org/10.4319/lo.1986.31.4.0839

Mintrop, L., Pérez, F.F., González-Dávila, M., Santana-Casiano, J.M., and Körtzinger, A. 2000. Alkalinity determination by potentiometry: intercalibration using three different methods. Cienc. Mar. 26(1):23–27. https://doi.org/10.7773/cm.v26i1.573

Mitchell, M.R., Harrison, G., Pauley, K., Gagné, A., Maillet, G., and Strain, P. 2002. Atlantic Zonal Monitoring Program sampling protocol. Can. Tech. Rep. Hydrogr. Ocean Sci. 223: iv+23 p.

Moraga, P. 2023. Spatial statistics for data science: theory and practice with R (1st ed.). Chapman and Hall/CRC, New York. 298 p. https://doi.org/10.1201/9781032641522

Morse, J.W., and Mackenzie, F.T. 1990. Geochemistry of sedimentary carbonates. Elsevier, Amsterdam. 707 p.

Morse, J.W., Arvidson, R.S., and Lüttge, A. 2007. Calcium carbonate formation and dissolution. Chem. Rev. 107(2):342–381. https://doi.org/10.1021/cr050358j

Mucci, A. 1983. The solubility of calcite and aragonite in seawater at various salinities, temperatures, and one atmosphere total pressure. Am. J. Sci. 283(7):780–799. https://doi.org/10.2475/ajs.283.7.780

Mucci, A., Starr, M., Gilbert, D., and Sundby, B. 2011. Acidification of Lower St. Lawrence Estuary bottom waters. Atmos.–Ocean 49(3):206–218. https://doi.org/10.1080/07055900.2011.599265

Mucci, A., Levasseur, M., Gratton, Y., Martias, C., Scarratt, M., Gilbert, D., Tremblay, J.-É., Ferreyra, G., and Lansard, B. 2017. Tidally induced variations of pH at the head of the Laurentian Channel. Can. J. Fish. Aquat. Sci. 75:1128–1141. https://doi.org/10.1139/cjfas-2017-0007

Nilsson, G.E., Dixson, D.L., Domenici, P., McCormick, M.I., Sørensen, C., Watson, S.-A., and Munday, P.L. 2012. Near-future carbon dioxide levels alter fish behaviour by interfering with neurotransmitter function. Nat. Clim. Change 2:201–204. https://doi.org/10.1038/nclimate1352

Ninokawa, A.T., Saley, A.M., Shalchi, R., and Gaylord, B. 2024. Multiple carbonate system parameters independently govern shell formation in a marine mussel. Commun. Earth Environ. 5:273. https://doi.org/10.1038/s43247-024-01440-5

NOAA Ocean Acidification Program. 2024. Ocean acidification. Copernicus Marine Environment Monitoring Service. https://marine.copernicus.eu/ocean-climate-portal/ocean-acidification

Nozères, C., Archambault, D., Chouinard, P.-M., Gauthier, J., Miller, R., Parent, E., Schwab, P., Savard, L., and Dutil, J.-D. 2010. Identification guide for marine fishes of the estuary and northern Gulf of St. Lawrence and sampling protocols used during trawl surveys between 2004 and 2008. Can. Tech. Rep. Fish. Aquat. Sci. 2866: xi+243 p.

Nydahl, A., Panigrahi, S., and Wikner, J. 2013. Increased microbial activity in a warmer and wetter climate enhances the risk of coastal hypoxia. FEMS Microbiol. Ecol. 85(2):338–347. https://doi.org/10.1111/1574-6941.12123

Orr, J., Fabry, V., Aumont, O., Bopp, L., Doney, S.C., Feely, R.A., Gnanadesikan, A., Gruber, N., Ishida, A., Joos, F., Key, R.M., Lindsay, K., Maier-Reimer, E., Matear, R., Monfray, P., Mouchet, A., Najjar, R.G., Plattner, G.-K., Rodgers, K.B., Sabine, C.L., Sarmiento, J.L., Schlitzer, R., Slater, R.D., Totterdell, I.J., Weirig, M.-F., Yamanaka, Y., and Yool, A. 2005. Anthropogenic ocean acidification over the twenty-first century and its impact on calcifying organisms. Nature 437:681–686. https://doi.org/10.1038/nature04095

Orr, J.C., Epitalon, J.-M., and Gattuso, J.-P. 2015. Comparison of ten packages that compute ocean carbonate chemistry. Biogeosciences 12:1483–1510. https://doi.org/10.5194/bg-12-1483-2015

Ouellet, P., and Sainte-Marie, B. 2018. Vertical distribution of snow crab (Chionoecetes opilio) pelagic stages in the Gulf of St. Lawrence (Canada) and effect of temperature on development and survival. ICES J. Mar. Sci. 75(2), 773–784. https://doi.org/10.1093/icesjms/fsx169

Padilla-Gamino, J.L., Alma, L., Spencer, L.H., Venkataraman, Y.R., and Wessler, L. 2022. Ocean acidification does not overlook sex: review of understudied effects and implications of low pH on marine invertebrate sexual reproduction. Front. Mar. Sci. 9:977754. https://doi.org/10.3389/fmars.2022.977754

Perez, F.F., and Fraga, F. 1987. Association constant of fluoride and hydrogen ions in seawater. Mar. Chem. 21(2):161–168. https://doi.org/10.1016/0304-4203(87)90036-3

Perry, S.F., and Gilmour, K.M. 2006. Acid–base balance and CO_2 excretion in fish: unanswered questions and emerging models. Respir. Physiol. Neurobiol. 154(1–2):199–215. https://doi.org/10.1016/j.resp.2006.04.010

Pimentel, M.S., Faleiro, F., Marques, T., Bispo, R., Dionísio, G., Faria, A.M., Machado, J., Peck, M.A., Pörtner, H.-O., Pousão-Ferreira, P., Gonçalves, E.J., and Rosa, R. 2016. Foraging behaviour, swimming performance and malformations of early stages of commercially important fishes under ocean acidification and warming. Clim. Change 137:495–509. https://doi.org/10.1007/s10584-016-1682-5

Pörtner, H.-O. 2012. Oceans under climate change: effects of warming, hypoxia and acidification on marine animals. Comp. Biochem. Physiol. A 163(Suppl.):S1–S3. https://doi.org/10.1016/j.cbpa.2012.05.007

Pousse, E., Poach, M.E., Redman, D.H., Sennefelder, G., White, L.E., Lindsay, J.M., Munroe, D., Hart, D., Hennen, D., Dixon, M.S., Li, Y., Wikfors, G.H., and Meseck, S. 2020. Energetic response of Atlantic surfclam Spisula solidissima to ocean acidification. Mar. Pollut. Bull. 161:111740. https://doi.org/10.1016/j.marpolbul.2020.111740

Raimondi, L., Matthews, J.B.R., Atamanchuk, D., Azetsu-Scott, K., and Wallace, D.W.R. 2019. The internal consistency of the marine carbon dioxide system for high latitude shipboard and in situ monitoring. Mar. Chem. 213:49–70. https://doi.org/10.1016/j.marchem.2019.03.001

Reimer, J.J., Medeiros, P.M., Hussain, N., Gonski, S.F., Xu, Y.-Y., Huang, T.-H., and Cai, W.-J. 2024. Carbonate chemistry and the potential for acidification in Georgia coastal marshes and the South Atlantic Bight, USA. Estuaries Coasts 47:76–90. https://doi.org/10.1007/s12237-023-01261-3

Ries, J.B., Cohen, A.L., and McCorkle, D.C. 2009. Marine calcifiers exhibit mixed responses to CO2-induced ocean acidification. Geology 37(12):1131–1134. https://doi.org/10.1130/G30210A.1

Robinson, C. 2019. Microbial respiration, the engine of ocean deoxygenation. Front. Mar. Sci. 5:533. https://doi.org/10.3389/fmars.2018.00533

Rodríguez-Domínguez, A., Connell, S.D., Baziret, C., and Nagelkerken, I. 2018. Irreversible behavioural impairment of fish starts early: embryonic exposure to ocean acidification. Mar. Pollut. Bull. 133:562–567. https://doi.org/10.1016/j.marpolbul.2018.06.004

Roleda, M.Y., Boyd, P.W., and Hurd, C.L. 2012. Before ocean acidification: calcifier chemistry lessons. J. Phycol. 48(4):840–843. https://doi.org/10.1111/j.1529-8817.2012.01195.x

Sakschewski, B., Caesar, L., Andersen, L., Bechthold, M., Bergfeld, L., Beusen, A., Billing, M., Bodirsky, B.L., Botsyun, S., Dennis, D., Donges, J.F., Dou, X., Eriksson, A., Fetzer, I., Gerten, D., Häyhä, T., Hebden, S., Heckmann, T., Heilemann, A., Huiskamp, W.N., Jahnke, A., Kaiser, J., Kitzmann, N., Krönke, J., Kühnel, D., Laureanti, N.C., Li, C., Liu, Z., Loriani, S., Ludescher, J., Mathesius, S., Norström, A., Otto, F., Paolucci, A., Pokhotelov, D., Rafiezadeh Shahi, K., Raju, E., Rostami, M., Schaphoff, S., Schmidt, C., Steinert, N.J., Stenzel, F., Virkki, V., Wendt-Potthoff, K., Wunderling, N., and Rockström, J. 2025. Planetary health check 2025: a scientific assessment of the state of the planet. Potsdam Institute for Climate Impact Research, Potsdam. 144 p. https://doi.org/10.48485/pik.2025.017

Schwaner, C., Barbose, M., Connors, P., Park, T.-J., de Silva, D., Griffith, A., Gobler, C.J., Espinosa, E.P., and Allam, B. 2020. Experimental acidification increases susceptibility of Mercenaria mercenaria to infection by Vibrio species. Mar. Environ. Res. 154:104872. https://doi.org/10.1016/j.marenvres.2019.104872

Shi, Y., and Li, Y. 2024. Impacts of ocean acidification on physiology and ecology of marine invertebrates: a comprehensive review. Aquat. Ecol. 58:207–226. https://doi.org/10.1007/s10452-023-10058-2

Siedlecki, S.A., Salisbury, J., Gledhill, D.K., Bastidas, C., Meseck, S., McGarry, K., Hunt, C.W., Alexander, M., Lavoie, D., Wang, Z.A., Scott, J., Brady, D.C., Mlsna, I., Azetsu-Scott, K., Liberti, C.M., Melrose, D.C., White, M.M., Pershing, A., Vandemark, D., Townsend, D.W., Chen, C., Mook, W., and Morrison, R. 2021. Projecting ocean acidification impacts for the Gulf of Maine to 2050: new tools and expectations. Elem. Sci. Anth. 9(1):29. https://doi.org/10.1525/elementa.2020.00062

Simpson, E., Ianson, D., and Kohfeld, K.E. 2022. Using end-member models to estimate seasonal carbonate chemistry and acidification sensitivity in temperate estuaries. Geophys. Res. Lett. 49(2):e2021GL095579. https://doi.org/10.1029/2021GL095579

Small, D.P., Calosi, P., Boothroyd, D., and Spicer, J.I. 2015. Stage-specific changes in physiological and life-history responses to elevated temperature and pCO_2 during the larval development of the European lobster Homarus gammarus (L.). Physiol. Biochem. Zool. 88(5):494–507. https://doi.org/10.1086/682238

Small, D.P., Calosi, P., Boothroyd, D., and Spicer, J.I. 2016. The sensitivity of the early benthic juvenile stage of the European lobster Homarus gammarus (L.) to elevated pCO_2 and temperature. Mar. Biol. 163:53. https://doi.org/10.1007/s00227-016-2834-x

Small, D.P., Calosi, P., Rastrick, S.P.S., Turner, L.M., Widdicombe, S., and Spicer, J.I. 2020. The effects of elevated temperature and pCO2 on the energetics and haemolymph pH homeostasis of juveniles of the European lobster Homarus gammarus. J. Exp. Biol. 223(8):jeb209221. https://doi.org/10.1242/jeb.209221

Spicer, J.I., and Morley, S.A. 2022. Hypercapnia in marine environments: physiological impacts and ecological consequences. Front. Mar. Sci. 9:977754. https://doi.org/10.3389/fmars.2022.977754

Steinhart, R. 2023. Temporal and spatial analysis of the relationship between hypoxia, temperature, and benthic biodiversity in the St. Lawrence Estuary and Gulf. M.Sc. thesis, Memorial University of Newfoundland. 143 p.

Stiasny, M.H., Mittermayer, F.H., Sswat, M., Voss, R., Jutfelt, F., Chierici, M., Puvanendran, V., Mortensen, A., Reusch, T.B.H., and Clemmesen, C. 2021. Ocean acidification effects on Atlantic cod larval survival and recruitment to the fished population. PLoS One 16(8):e0155448. https://doi.org/10.1371/journal.pone.0155448

Stumpp, M., Hu, M.Y., Melzner, F., Gutowska, M.A., Dorey, N., Himmerkus, N., Holtmann, W.C., Dupont, S., Thorndyke, M.C., and Bleich, M. 2012. Acidified seawater impacts sea urchin larval pH regulatory systems relevant for calcification. Proc. Natl. Acad. Sci. U.S.A. 109(44):18192–18197. https://doi.org/10.1073/pnas.1209174109

Sunday, J.M., Fabricius, K.E., Kroeker, K.J., Anderson, K.M., Brown, N.E., Barry, J.P., Connell, S.D., Dupont, S., Gaylord, B., Hall-Spencer, J.M., Klinger, T., Milazzo, M., Munday, P.L., Russell, B.D., Sanford, E., Thiyagarajan, V., Vaughan, M.L.H., Widdicombe, S., and Harley, C.D.G. 2017. Ocean acidification can mediate biodiversity shifts by changing biogenic habitat. Nat. Clim. Change 7:81–85. https://doi.org/10.1038/nclimate3161

Takahashi, T., Sutherland, S.C., and Kozyr, A. 2017. Global ocean surface water partial pressure of CO2 database (1957–2019), LDEO database (version 2019). NOAA Natl. Cent. Environ. Inf. Dataset. https://doi.org/10.3334/CDIAC/OTG.NDP088(V2015)

Therriault, J.-C., Petrie, B., Gagnon, J., Gregory, D., Helbig, J., Herman, A., Lefaivre, D., Mitchell, M., Pelchat, B., Runge, J., and Sameoto, D. 1998. Proposal for a Northwest Atlantic Zonal Monitoring Program. Can. Tech. Rep. Hydrogr. Ocean Sci. 194: vii+57 p.

Thibodeau, B., de Vernal, A., and Mucci, A. 2006. Recent eutrophication and consequent hypoxia in the bottom waters of the Lower St. Lawrence Estuary: micropaleontological and geochemical evidence. Mar. Geol. 231(1–4):37–50. https://doi.org/10.1016/j.margeo.2006.05.010

Thibodeau, B., de Vernal, A., Hillaire-Marcel, C., and Mucci, A. 2010. Twentieth-century warming in deep waters of the Gulf of St. Lawrence: a unique feature of the last millennium. Geophys. Res. Lett. 37(17):L17604. https://doi.org/10.1029/2010GL044771

Thomsen, J., Haynert, K., Wegner, K.M., and Melzner, F. 2015. Impact of seawater carbonate chemistry on the calcification of marine bivalves. Biogeosciences 12:4209–4220. https://doi.org/10.5194/bg-12-4209-2015

Toyofuku, T., Matsuo, M.Y., de Nooijer, L.J., Nagai, Y., Kawada, S., Fujita, K., Reichart, G.-J., Nomaki, H., Tsuchiya, M., Sakaguchi, H., and Kitazato, H. 2017. Proton pumping accompanies calcification in foraminifera. Nat. Commun. 8:14145. https://doi.org/10.1038/ncomms14145

Vargas, C.A., Cuevas, L.A., Broitman, B.R., San Martin, V.A., Lagos, N.A., Gaitán-Espitia, J.D., and Dupont, S. 2022. Upper environmental pCO_2 drives sensitivity to ocean acidification in marine invertebrates. Nat. Clim. Change 12:200–207. https://doi.org/10.1038/s41558-021-01269-2

Waldbusser, G.G., and Salisbury, J.E. 2014. Ocean acidification in the coastal zone from an organism's perspective: multiple system parameters, frequency domains, and habitats. Annu. Rev. Mar. Sci. 6:221–247. https://doi.org/10.1146/annurev-marine-121211-172238

Wallace, R.B., Baumann, H., Grear, J.S., Aller, R.C., and Gobler, C.J. 2014. Coastal ocean acidification: the other eutrophication problem. Estuar. Coast. Shelf Sci. 148:1–13. https://doi.org/10.1016/j.ecss.2014.05.027

Wang, Z.A., Wanninkhof, R., Cai, W.-J., Byrne, R.H., Hu, X., Peng, T.-H., and Huang, W.-J. 2013. The marine inorganic carbon system along the Gulf of Mexico and Atlantic coasts of the United States: insights from a transregional coastal carbon study. Limnol. Oceanogr. 58(1):325–342. https://doi.org/10.4319/lo.2013.58.1.0325

Weiss, R.F. 1974. Carbon dioxide in water and seawater: the solubility of a non-ideal gas. Mar. Chem. 2(3):203–215. https://doi.org/10.1016/0304-4203(74)90015-2

Wright-Fairbanks, E., Jewett, E.B., and Coyle, K.O. 2025. Management considerations for establishing a coastal acidification monitoring system: insights from the U.S. Coastal Acidification Networks. Environ. Monit. Assess. 197:990. https://doi.org/10.1007/s10661-025-14434-3

Xue, L., and Cai, W.-J. 2020. Total alkalinity minus dissolved inorganic carbon as a proxy for deciphering ocean acidification mechanisms. Mar. Chem. 222:103791. https://doi.org/10.1016/j.marchem.2020.103791

6. TABLES

Table 1: Overview of oceanographic sampling, including dates, vessels, regions, and number of stations sampled during high frequency monitoring and seasonal surveys conducted in 2024.

High Frequency Monitoring Station

Date in 2024	Vessel	Station Name	Station Count
May 16 - Nov. 26	*Beluga II* (+ others)	Rimouski	22

Surveys

Date in 2024	Vessel	Region / Subregion	Station Count
Jun. 6 - 29	*Coriolis II*	Estuary	7
		Northwest Gulf	8
		Magdalen Shallows	40
		Centre Gulf / Cabot Strait	15
		Northeast Gulf	11
		Total	**81**
Aug. 3 - Sep. 20	*Teleost*	Estuary	5
		Northwest Gulf	5
		Magdalen Shallows	7
		Centre Gulf / Cabot Strait	8
		Northeast Gulf	11
		Total	**36**
Oct. 16 - Nov. 3	*Coriolis II*	Estuary	8
		Northwest Gulf	8
		Magdalen Shallows	15
		Centre Gulf / Cabot Strait	11
		Northeast Gulf	11
		Total	**53**

FIGURES

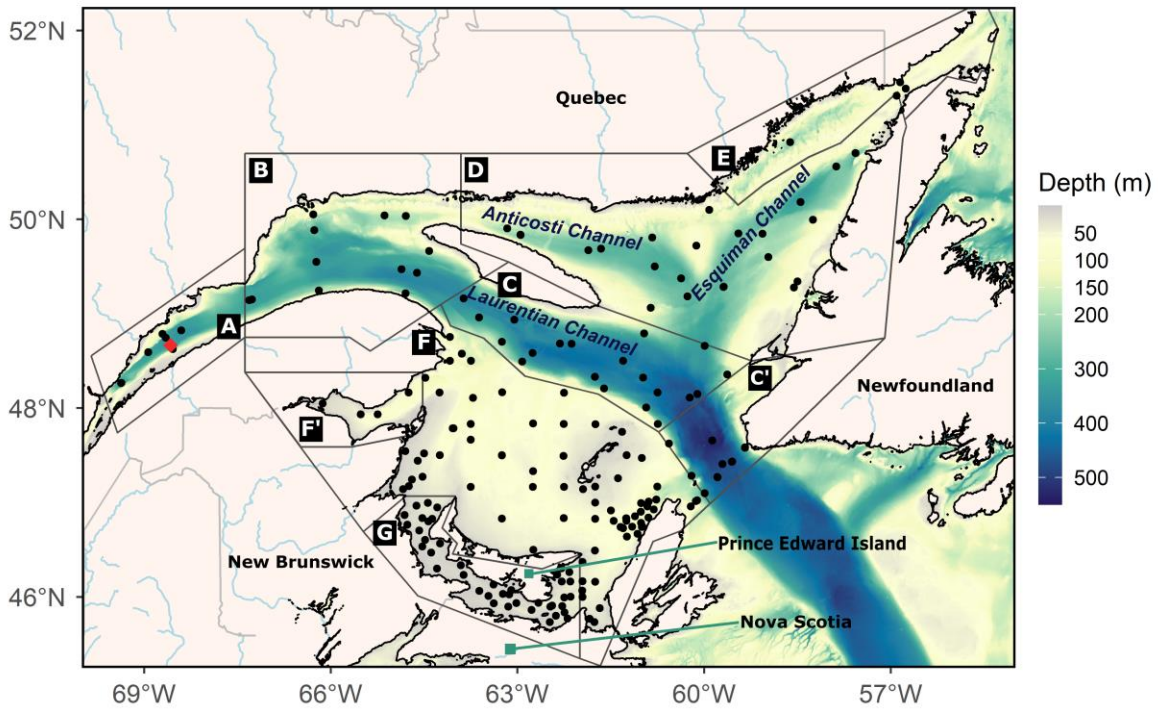

Figure 1: Bathymetric map of the Estuary and Gulf of St. Lawrence showing location of standard stations (black dots) and the high-frequency monitoring station of Rimouski (red diamond) sampled in 2024. The regional divisions can be identified as (A) Estuary, (B) Northwest Gulf, (C) Centre Gulf and Cabot Strait, (C') Cabot Strait (subregion of (C)), (D) Northeast Gulf, (E) Mécatina Trough and Strait of Belle Isle, (F) Magdalen Shallows, (F') Chaleur Bay (subregion of (F)), and (G) Northumberland Strait.

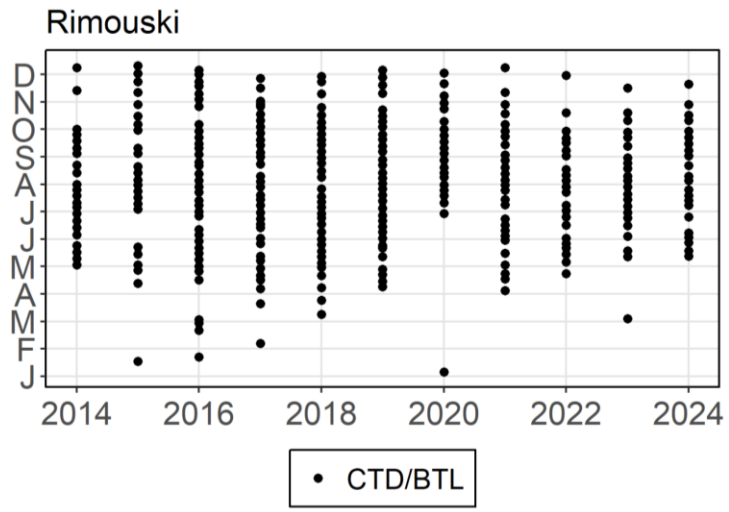

Figure 2: Annual sampling date distributions at Rimouski Station: months, from January (J) to December (D) appear on the y-axis while years, from 2014 to 2024, appear on the x-axis. The term CTD refers to Conductivity-Temperature-Depth probe deployment, and the term BTL refers to bottle sampling.

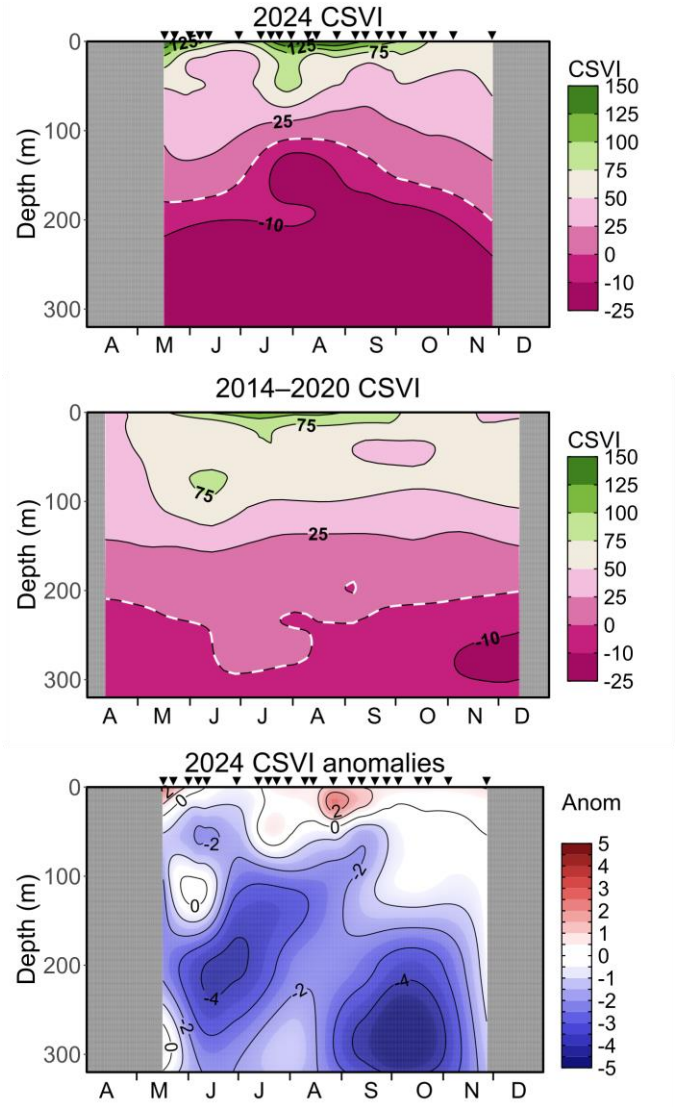

Figure 3: Vertical profiles of the carbonate system vulnerability index (CSVI = total alkalinity minus dissolved inorganic carbon ([TA] - [DIC] in µmol kg^{-1}) at Rimouski Station in 2024 (upper panel), climatology 2014–2020 (middle panel) and normalized anomalies (bottom panel). Anomaly colors convey both the direction and magnitude of deviations: white indicates normal values within ±½ standard deviation (SD) of the climatological mean, red denotes above-normal anomalies, and blue reflects below-normal anomalies. The dotted line indicates the threshold where TA = DIC ([TA] - [DIC] = 0). Station occupation dates are indicated by black triangles. Months appear on the x-axis, starting from April (A) and ending in December (D).

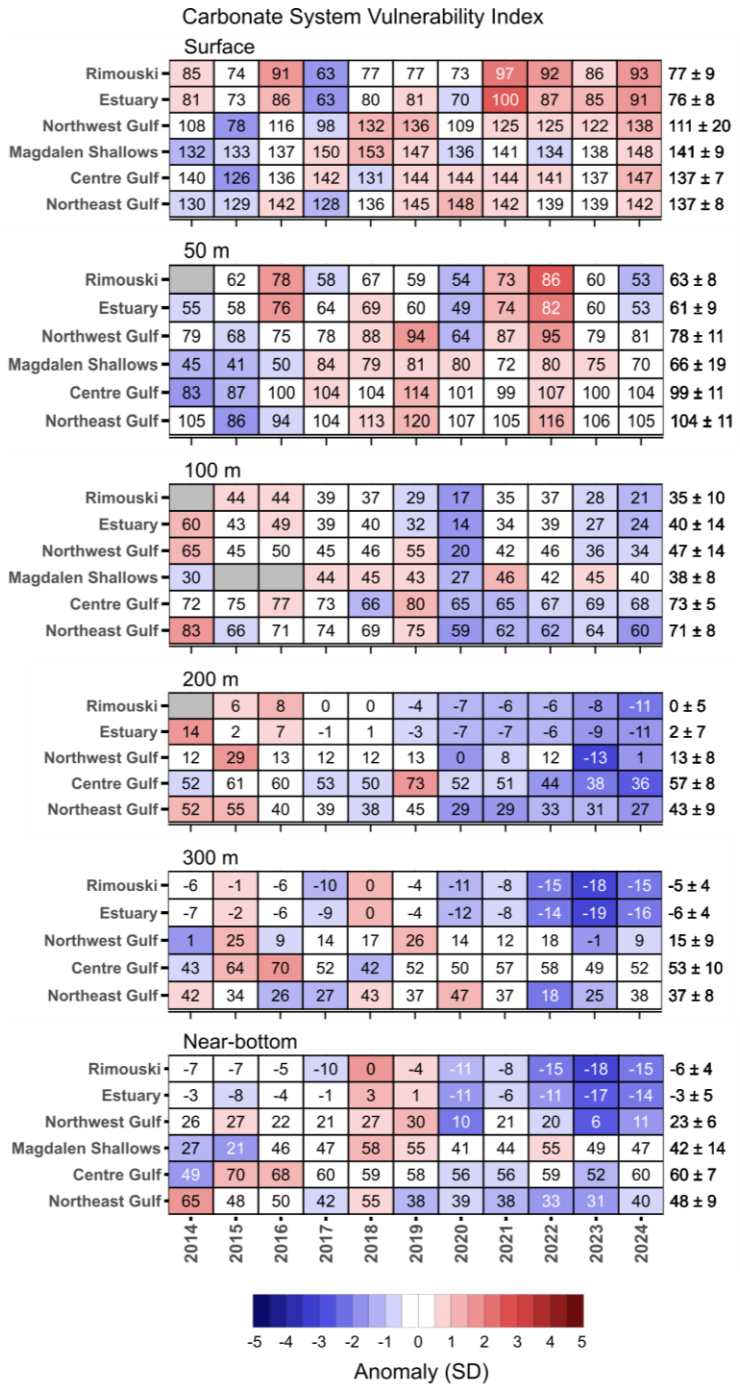

Figure 4 : Time series of annual anomalies in the carbonate system vulnerability index (CSVI = [TA] - [DIC], expressed in µmol kg^{-1}) from 2014 to 2024, calculated at six depths: surface, 50 m, 100 m, 200 m, 300 m, and near-bottom. The boxed values indicate annual CSVI averages, while the numbers aligned on the right represent the climatological means and standard deviations (SD) calculated over the period 2014–2020. Cell colors convey the direction and magnitude of anomalies: white cells indicate values within ± ½ SD of the climatological mean, red cells denote above-normal anomalies, and blue cells reflect below-normal anomalies. Grey cells mark insufficient or missing data. To enhance legibility, white text is used within cells where anomalies exceed ± 2 SD.

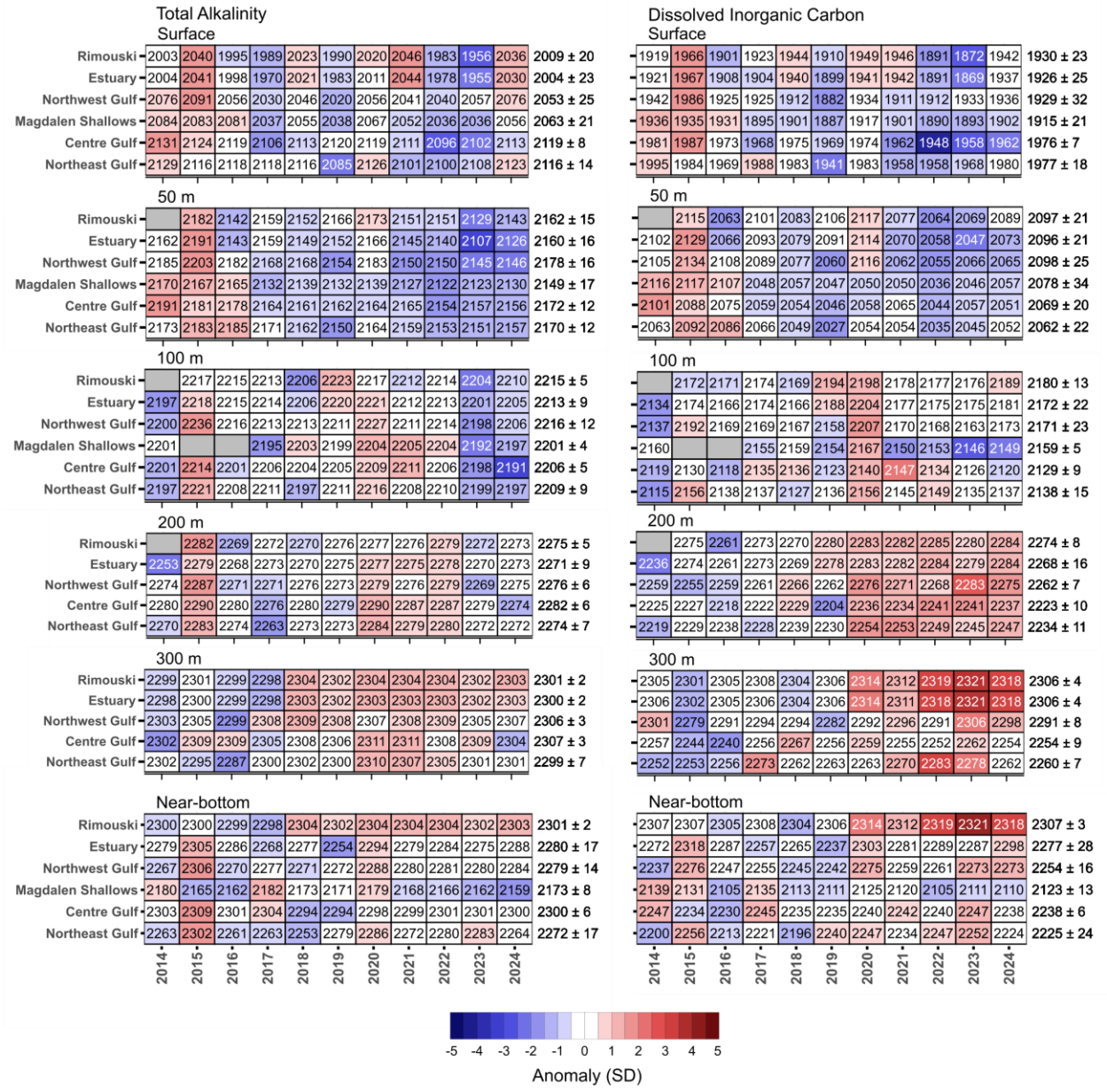

Figure 5 : Time series of annual anomalies in total alkalinity (TA, left panel, expressed in µmol kg^{-1}), and dissolved inorganic carbon (DIC, right panel, expressed in µmol kg^{-1}) from 2014 to 2024, measured at six depths: surface, 50 m, 100 m, 200 m, 300 m, and bottom. The boxed values indicate annual TA or DIC averages, while the numbers aligned on the right represent the climatological means and standard deviations (SD) calculated over the period 2014–2020. Cell colors convey the direction and magnitude of anomalies: white cells indicate values within ± ½ SD of the climatological mean, red cells denote above-normal anomalies, and blue cells reflect below-normal anomalies. Grey cells mark insufficient or missing data. To enhance legibility, white text is used within cells where anomalies exceed ± 2 SD.

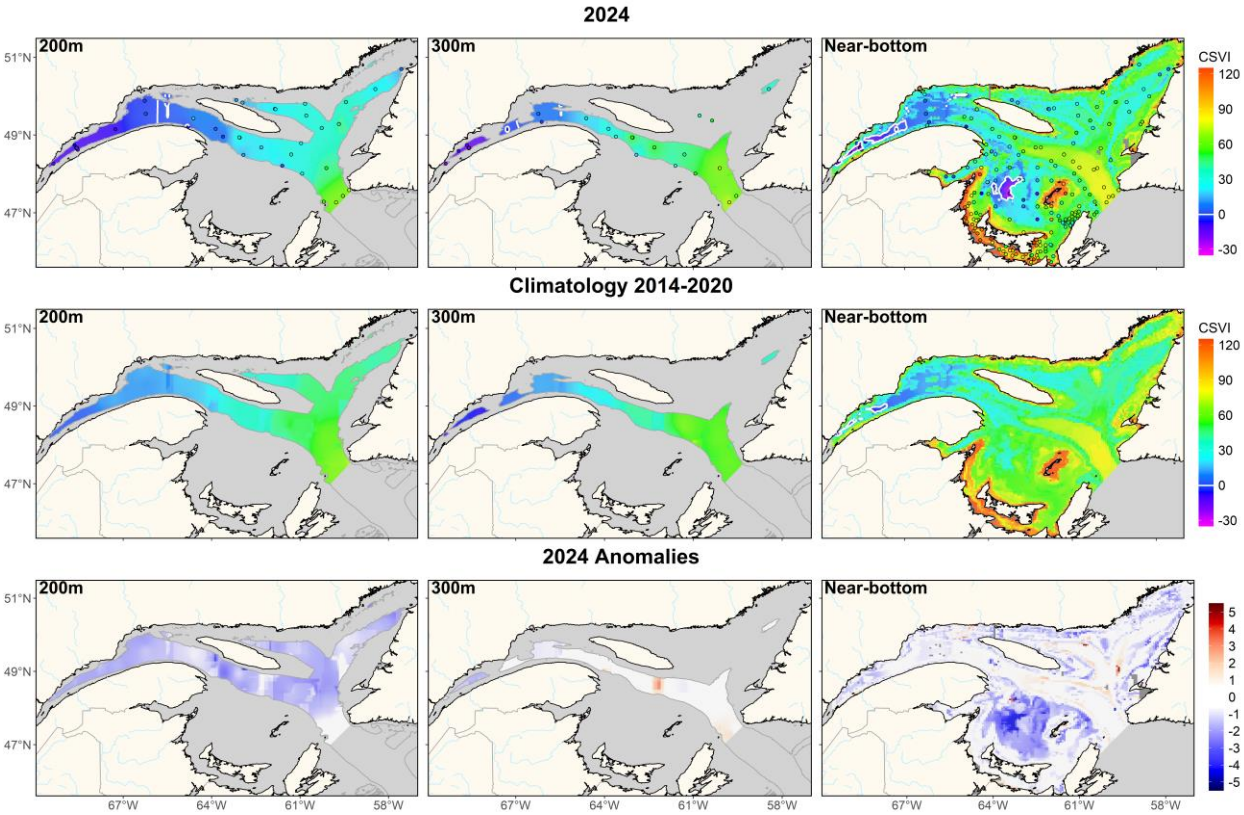

Figure 6 : Annual average distribution of carbonate system vulnerability index (CSVI in µmol kg^{-1}) at depths of 200 m and 300 m, and at the bottom in the Estuary and Gulf of St. Lawrence during 2024 (upper panels). The climatology (2014–2020; middle panels) and anomalies (lower panels) are also shown. In the bottom panels, anomaly colors convey both the direction and magnitude of deviations: white indicates normal values within ± ½ standard deviation (SD) of the climatological mean, red denotes above-normal anomalies, and blue reflects below-normal anomalies. The white contour line identifies a threshold of zero (0). Open circles (upper panel) show station locations in 2024.

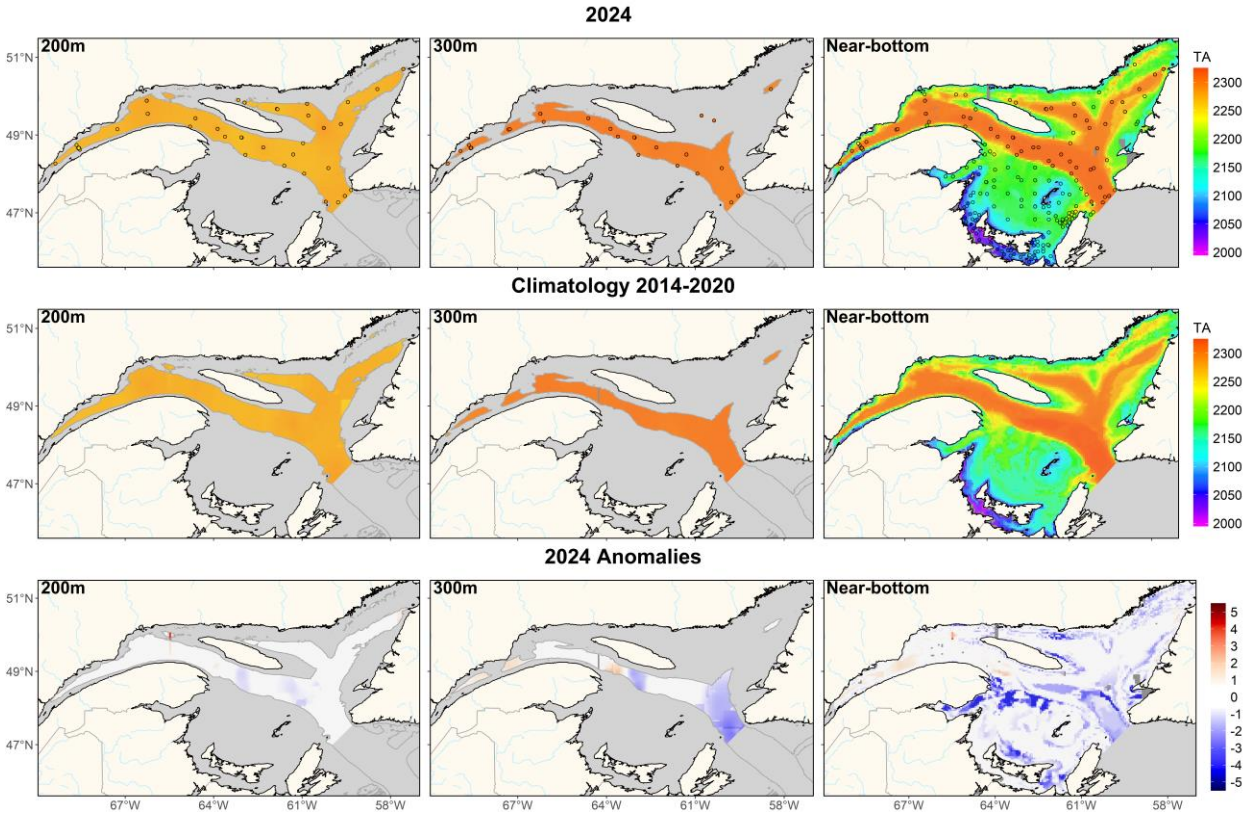

Figure 7 : Annual average distribution of total alkalinity (TA in µmol kg^{-1}) at depths of 200 m and 300 m, and at the bottom in the Estuary and Gulf of St. Lawrence during 2024 (upper panels). The climatology (2014–2020; middle panels) and anomalies (lower panels) are also shown. In the bottom panels, anomaly colors convey both the direction and magnitude of deviations: white indicates normal values within ± ½ standard deviation (SD) of the climatological mean, red denotes above-normal anomalies, and blue reflects below-normal anomalies. Open circles (upper panel) show station locations in 2024.

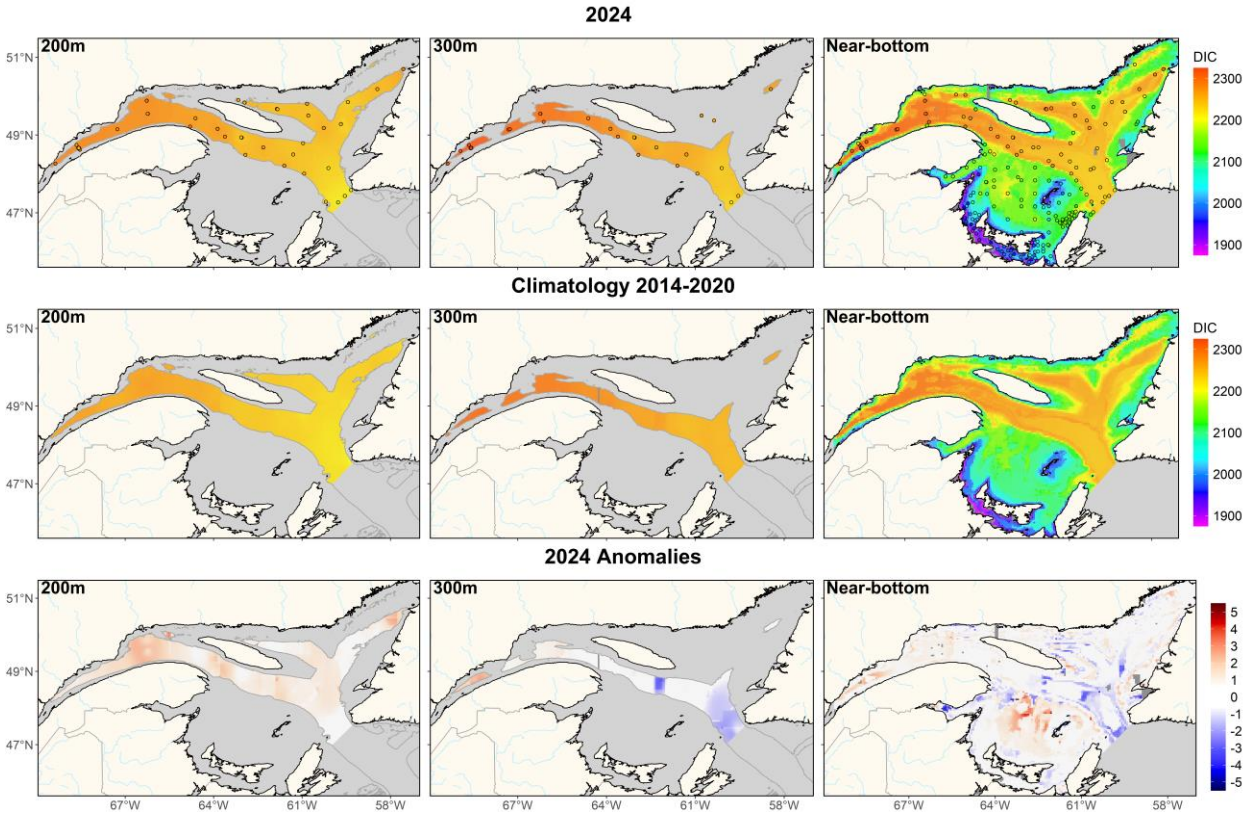

Figure 8 : Annual average distribution of dissolved inorganic carbon (DIC in µmol kg^{-1}) at depths of 200 m and 300 m, and at the bottom in the Estuary and Gulf of St. Lawrence during 2024 (upper panels). The climatology (2014–2020; middle panels) and anomalies (lower panels) are also shown. In the bottom panels, anomaly colors convey both the direction and magnitude of deviations: white indicates normal values within ± ½ standard deviation (SD) of the climatological mean, red denotes above-normal anomalies, and blue reflects below-normal anomalies. Open circles (upper panel) show station locations in 2024.

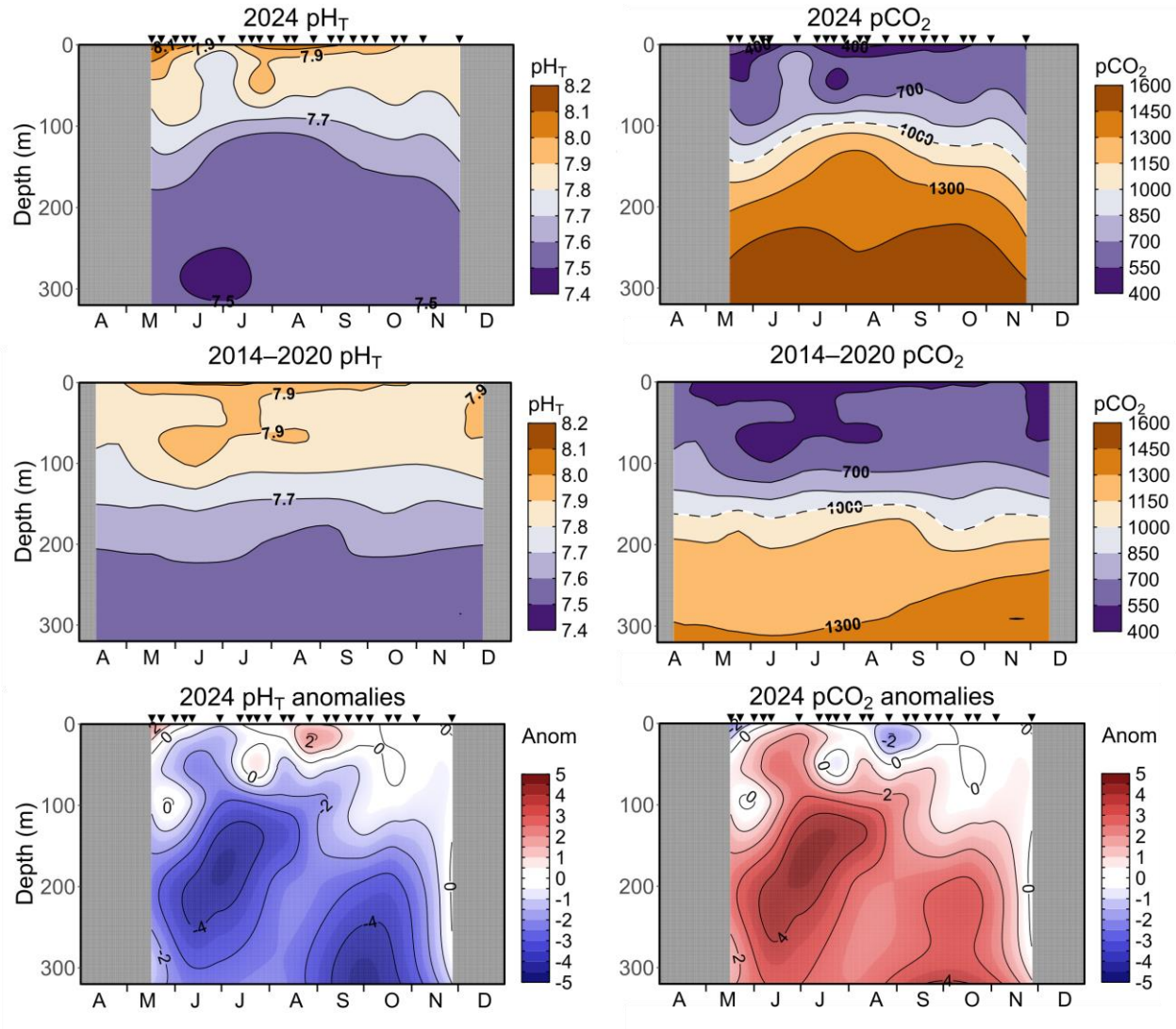

Figure 9 : Vertical profiles of pH_T (pH on the total scale; left panels) and partial pressure of CO_2 (pCO_2 in µatm, right panels) at Rimouski Station in 2024 (upper panels), climatology 2014–2020 (middle panels) and normalized anomalies (bottom panels). Anomaly colors convey both the direction and magnitude of deviations: white indicates normal values within ±½ standard deviation (SD) of the climatological mean, red denotes above-normal anomalies, and blue reflects below-normal anomalies. The dotted line in pCO_2 panels indicates the hypercapnic threshold of 1000 µatm. Station occupation dates are indicated by black triangles. Months appear on the x-axis, starting from April (A) and ending in December (D).

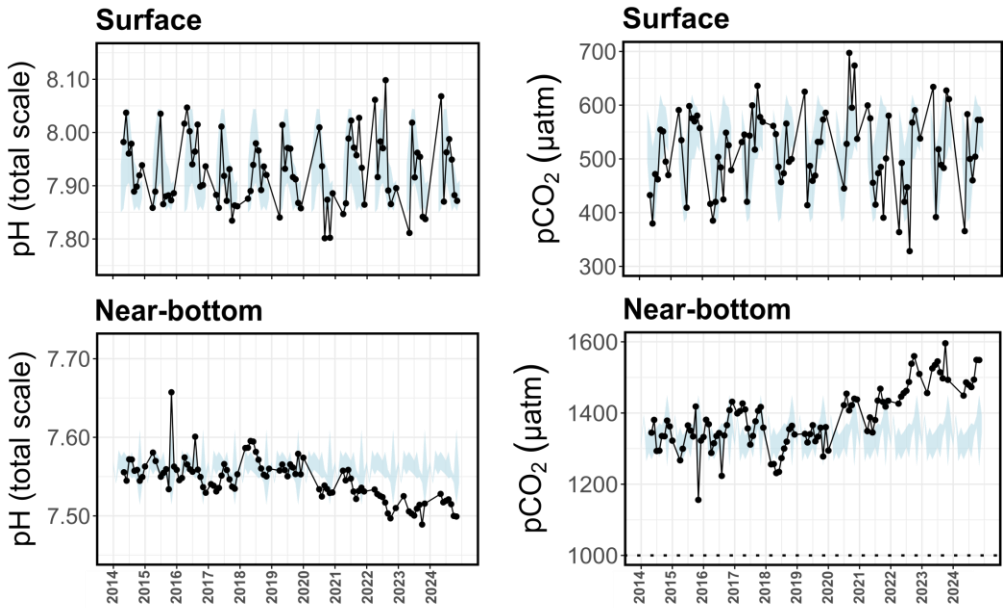

Figure 10 : Time series of the monthly average pH_T (total scale; left panels) and partial pressure of CO_2 (pCO_2 in µatm, right panels) at Rimouski Station in surface waters (top 0–15 m, upper panels), and in near-bottom waters (270–320 m, bottom panels). The blue shaded area on each panel indicates the respective monthly climatology for the 2014–2020 period. Note the different ranges in scales for pCO_2 and pH_T in different depth panels. The dotted line in the near-bottom pCO_2 panel indicates the hypercapnic threshold of 1000 µatm.

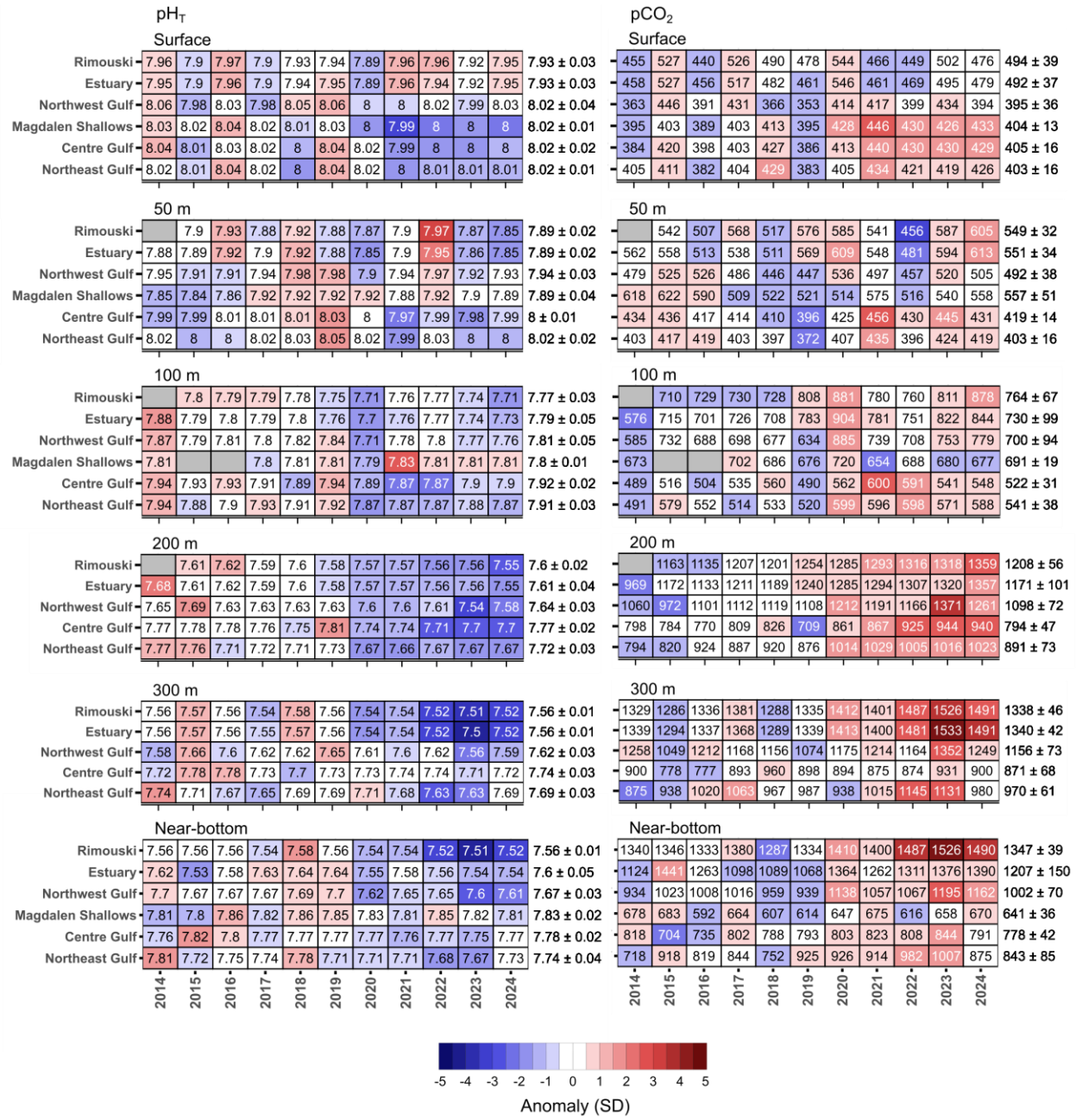

Figure 11 : Time series of annual anomalies in pH_T (left panel; pH expressed on the total scale), and partial pressure of CO_2 (right panel; pCO_2 expressed in µatm) from 2014 to 2024, respectively measured and calculated at six depths: surface, 50 m, 100 m, 200 m, 300 m, and bottom. The boxed values indicate annual pH_T or pCO_2 averages, while the numbers aligned on the right represent the climatological means and standard deviations (SD) calculated over the period 2014–2020. Cell colors convey the direction and magnitude of anomalies: white cells indicate values within ± ½ SD of the climatological mean, red cells denote above-normal anomalies, and blue cells reflect below-normal anomalies. Grey cells mark insufficient or missing data. To enhance legibility, white text is used within cells where anomalies exceed ± 2 SD.

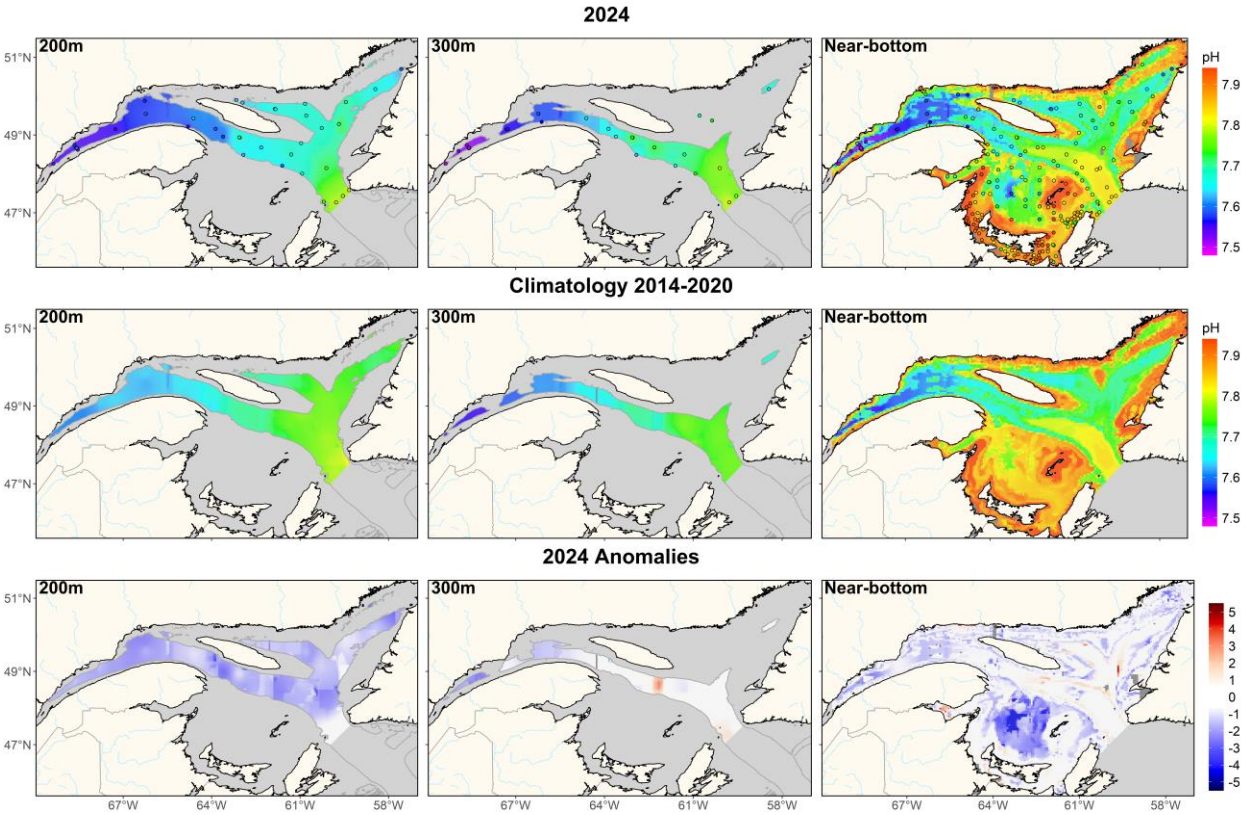

Figure 12 : Annual average distribution of *in situ* pH_T (pH on the total scale) at depths of 200 m and 300 m, and at the bottom in the Estuary and Gulf of St. Lawrence during 2024 (upper panels). The climatology (2014–2020; middle panels) and anomalies (lower panels) are also shown. In the bottom panels, anomaly colors convey both the direction and magnitude of deviations: white indicates normal values within ± ½ standard deviation (SD) of the climatological mean, red denotes above-normal anomalies, and blue reflects below-normal anomalies. Open circles (upper panels) show station locations in 2024.

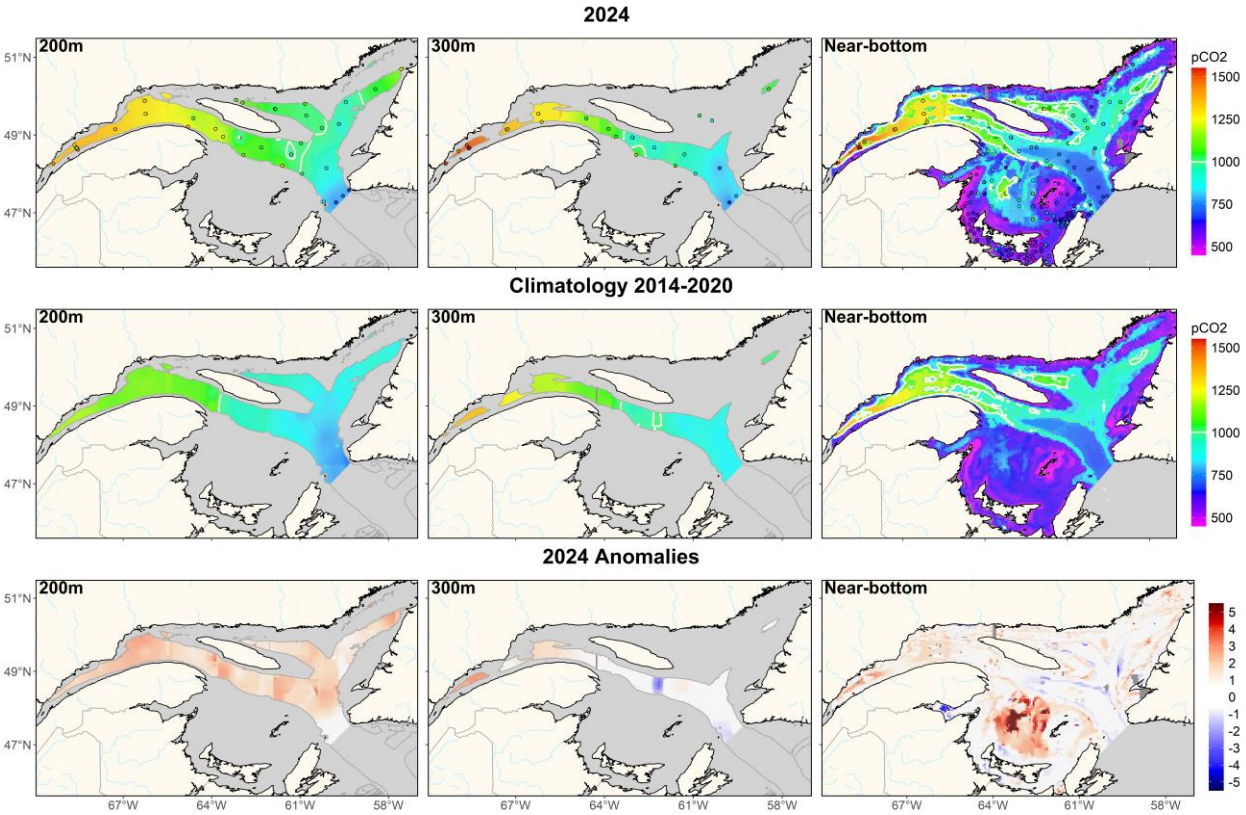

Figure 13 : Annual average distribution of partial pressure of CO_2 (pCO_2 in µatm) at the surface, at depths of 200 m and 300 m, and at the bottom in the Estuary and Gulf of St. Lawrence during 2024 (upper panels). The climatology (2014–2020; middle panels) and anomalies (lower panels) are also shown. The white contour line identifies hypercapnic areas ($pCO_2 \geq 1000$ µatm). In the bottom panels, anomaly colors convey both the direction and magnitude of deviations: white indicates normal values within ± ½ standard deviation (SD) of the climatological mean, red denotes above-normal anomalies, and blue reflects below-normal anomalies. Open circles (upper panel) show station locations in 2024.

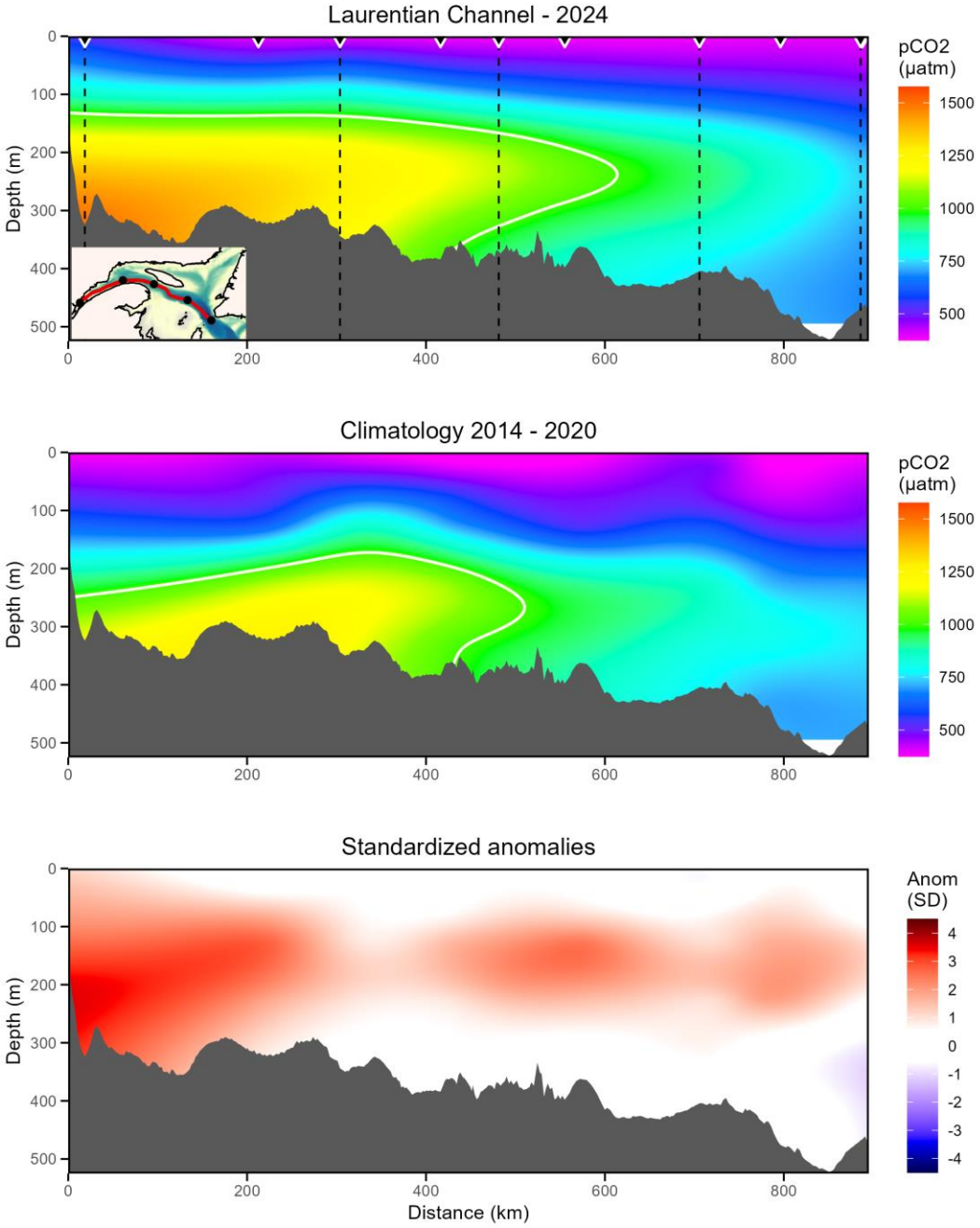

Figure 14 : Mean annual vertical distribution of pCO_2 along the Laurentian Channel in 2024 (upper panel) and for climatology (2014–2020; middle panel). Anomaly colors convey both the direction and magnitude of deviations: white indicates normal values within ± ½ standard deviation (SD) of the climatological mean, red denotes above-normal anomalies, and blue reflects below-normal anomalies. The section is presented from the head of the Laurentian Channel (Estuary) to Cabot Strait. Black triangles mark station positions in the upper panel. Dashed vertical lines align with geographic markers shown as black dots on the inset map in the lower-left corner.

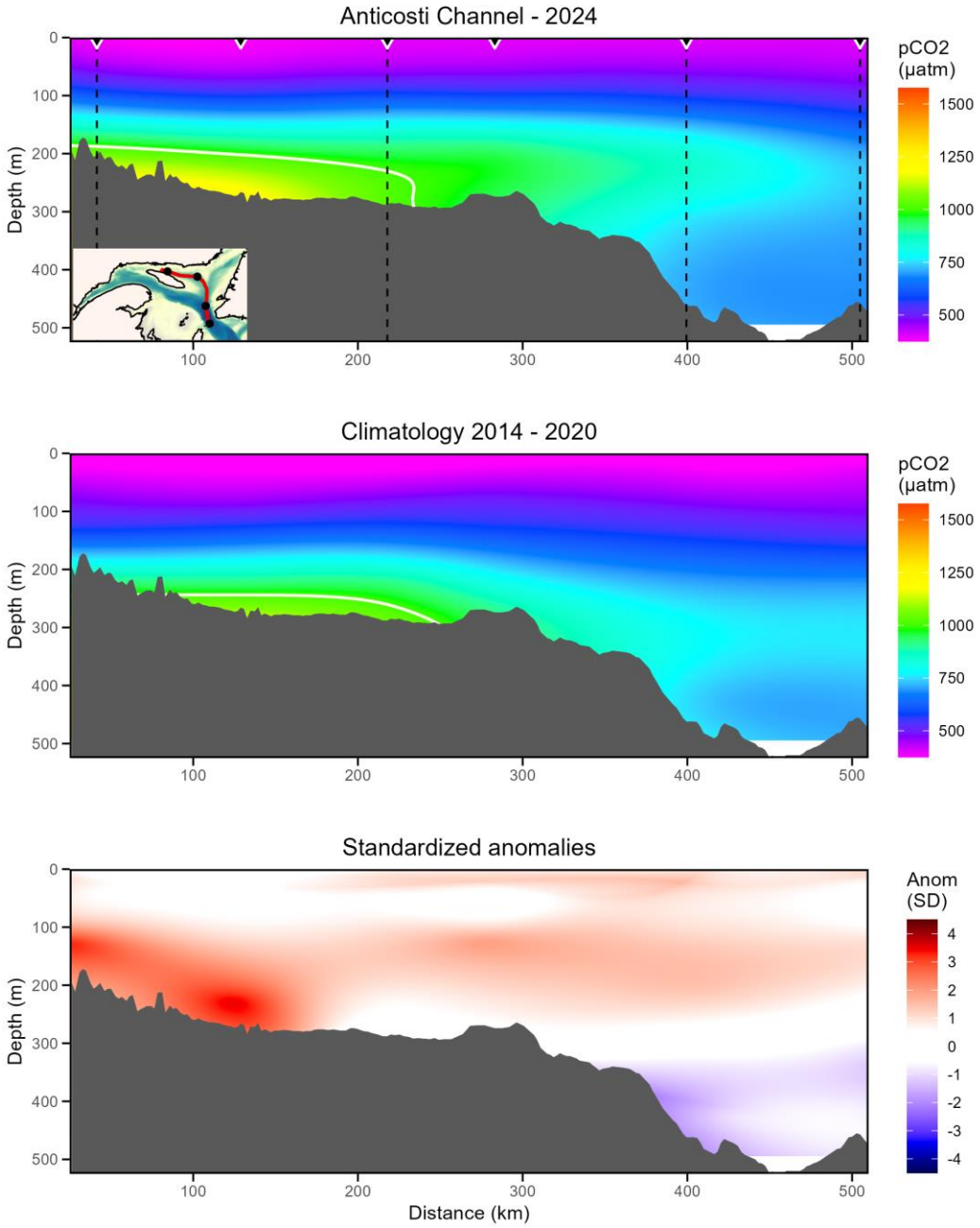

Figure 15 : Mean annual vertical distribution of pCO_2 along the Anticosti Channel in 2024 (upper panel) and for climatology (2014–2020; middle panel). Anomaly colors convey both the direction and magnitude of deviations: white indicates normal values within ± ½ standard deviation (SD) of the climatological mean, red denotes above-normal anomalies, and blue reflects below-normal anomalies. The section is presented from the head of the Anticosti Channel to Cabot Strait. Black triangles mark station positions in the upper panel. Dashed vertical lines align with geographic markers shown as black dots on the inset map in the lower-left corner.

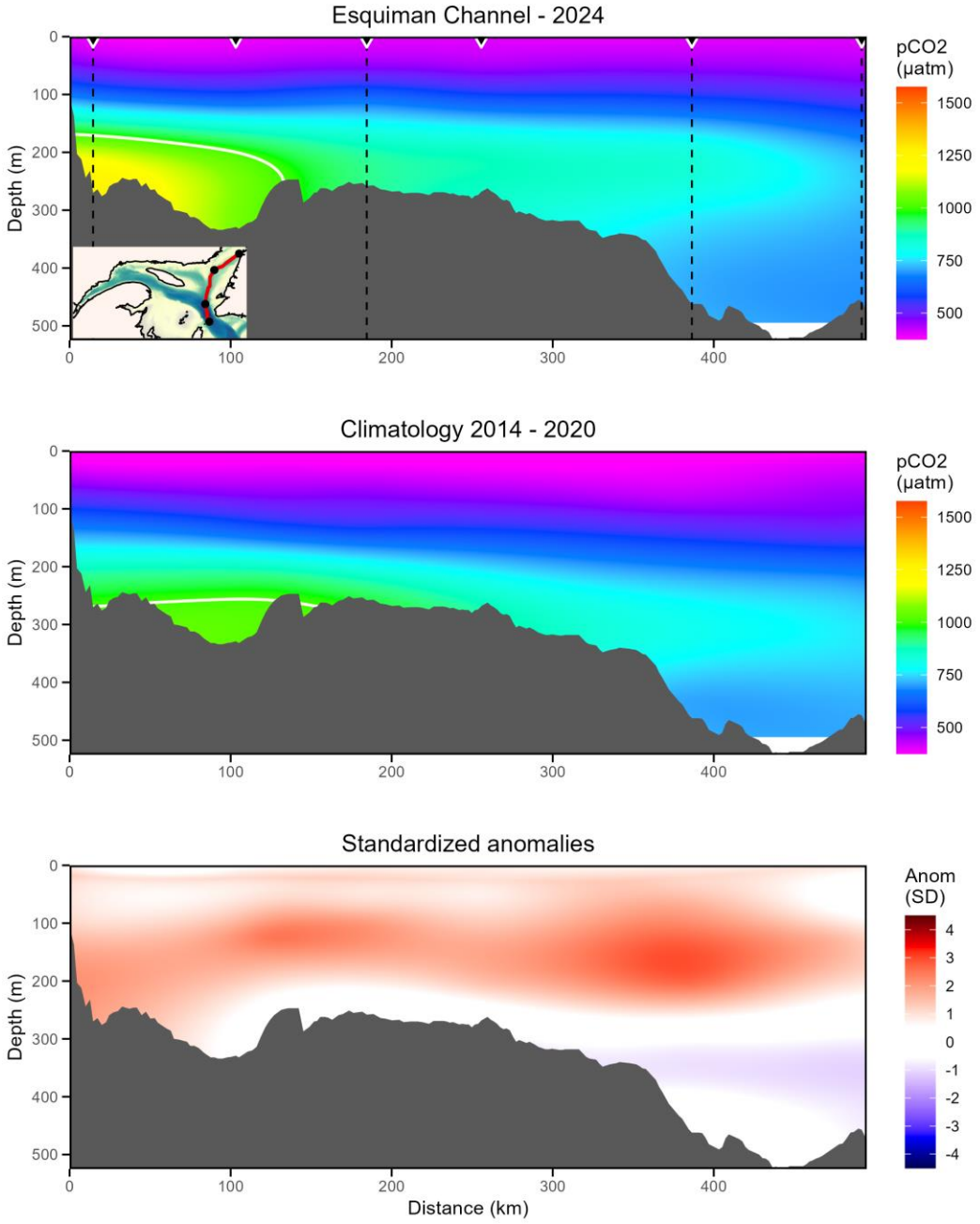

Figure 16 : Mean annual vertical distribution of pCO_2 along the Esquiman Channel in 2024 (upper panel) and for climatology (2014–2020; middle panel). Anomaly colors convey both the direction and magnitude of deviations: white indicates normal values within ± ½ standard deviation (SD) of the climatological mean, red denotes above-normal anomalies, and blue reflects below-normal anomalies. The section is presented from the head of the Esquiman Channel to Cabot Strait. Black triangles mark station positions in the upper panel. Dashed vertical lines align with geographic markers shown as black dots on the inset map in the lower-left corner.

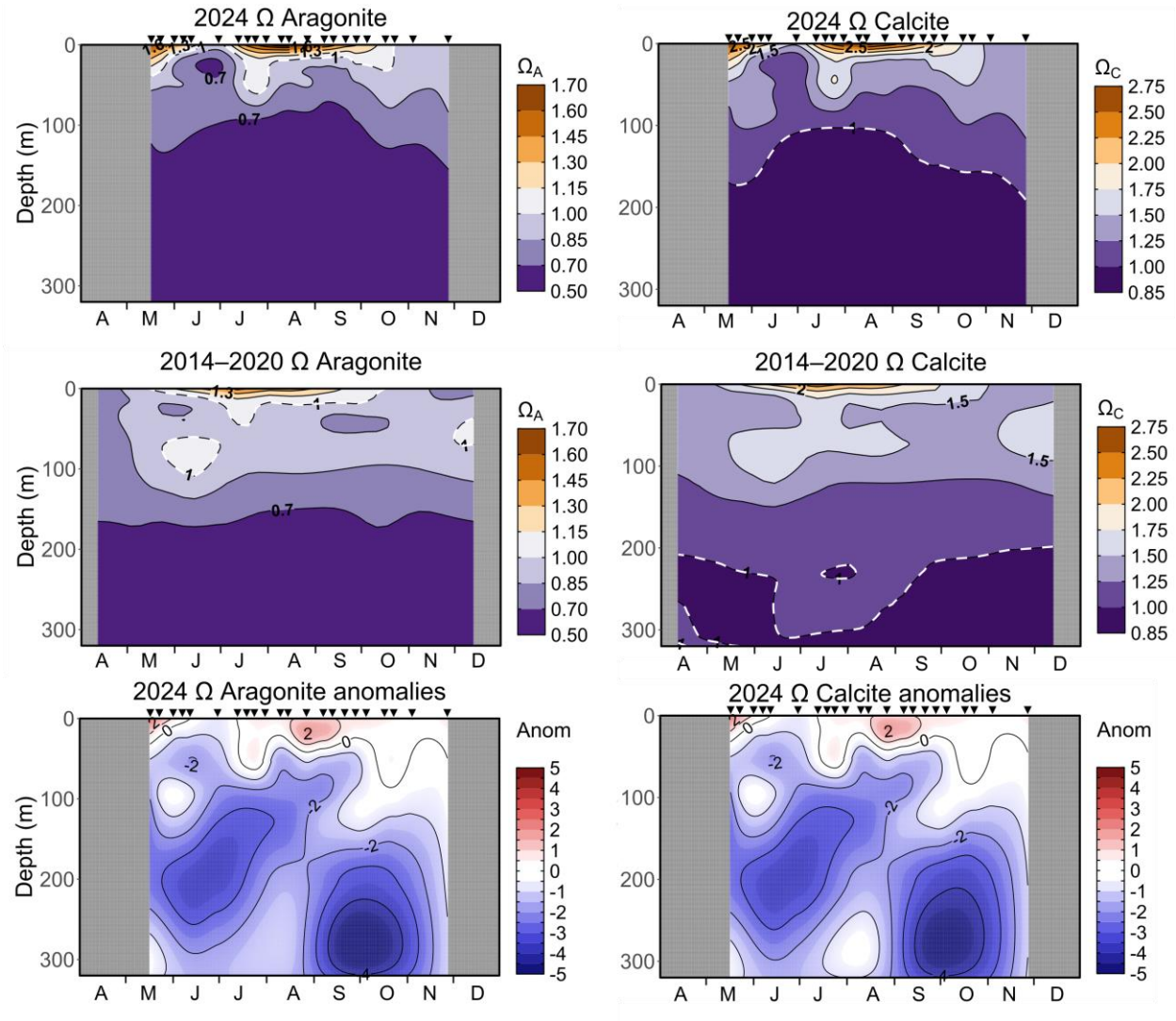

Figure 17 : Vertical profiles of saturation state of aragonite (Ω_A; unitless; left panels) and calcite (Ω_C; unitless; right panels) at Rimouski Station in 2024 (upper panels), climatology 2014–2020 (middle panels) and normalized anomalies (bottom panels). Anomaly colors convey both the direction and magnitude of deviations: white indicates normal values within ±½ standard deviation (SD) of the climatological mean, red denotes above-normal anomalies, and blue reflects below-normal anomalies. The dotted lines in panels indicate the critical thresholds of 1 for Ω_A and Ω_C. Note the different ranges in mineral saturation values for aragonite and calcite. Station occupation dates are indicated by black triangles. Months appear on the x-axis, starting from April (A) and ending in December (D).

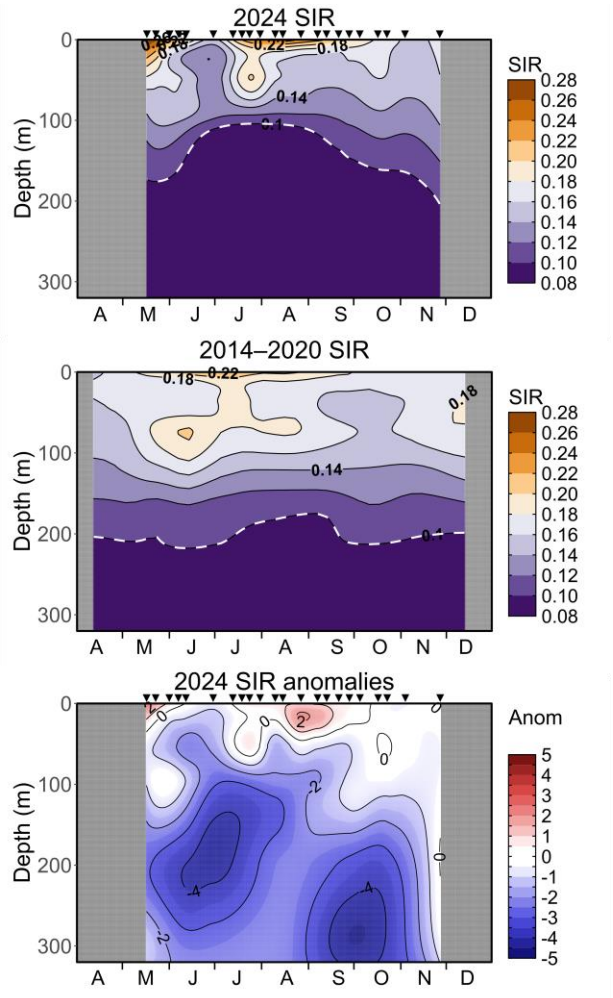

Figure 18 : Vertical profiles of the substrate-inhibitor ratio (SIR in mol µmol^{-1}) at Rimouski Station in 2024 (upper panel), climatology 2014–2020 (middle panel) and normalized anomalies (bottom panel). Anomaly colors convey both the direction and magnitude of deviations: white indicates normal values within ±½ standard deviation (SD) of the climatological mean, red denotes above-normal anomalies, and blue reflects below-normal anomalies. The dotted lines in panels indicate the critical thresholds of 0.100 for SIR. Station occupation dates are indicated by black triangles. Months appear on the x-axis, starting from April (A) and ending in December (D).

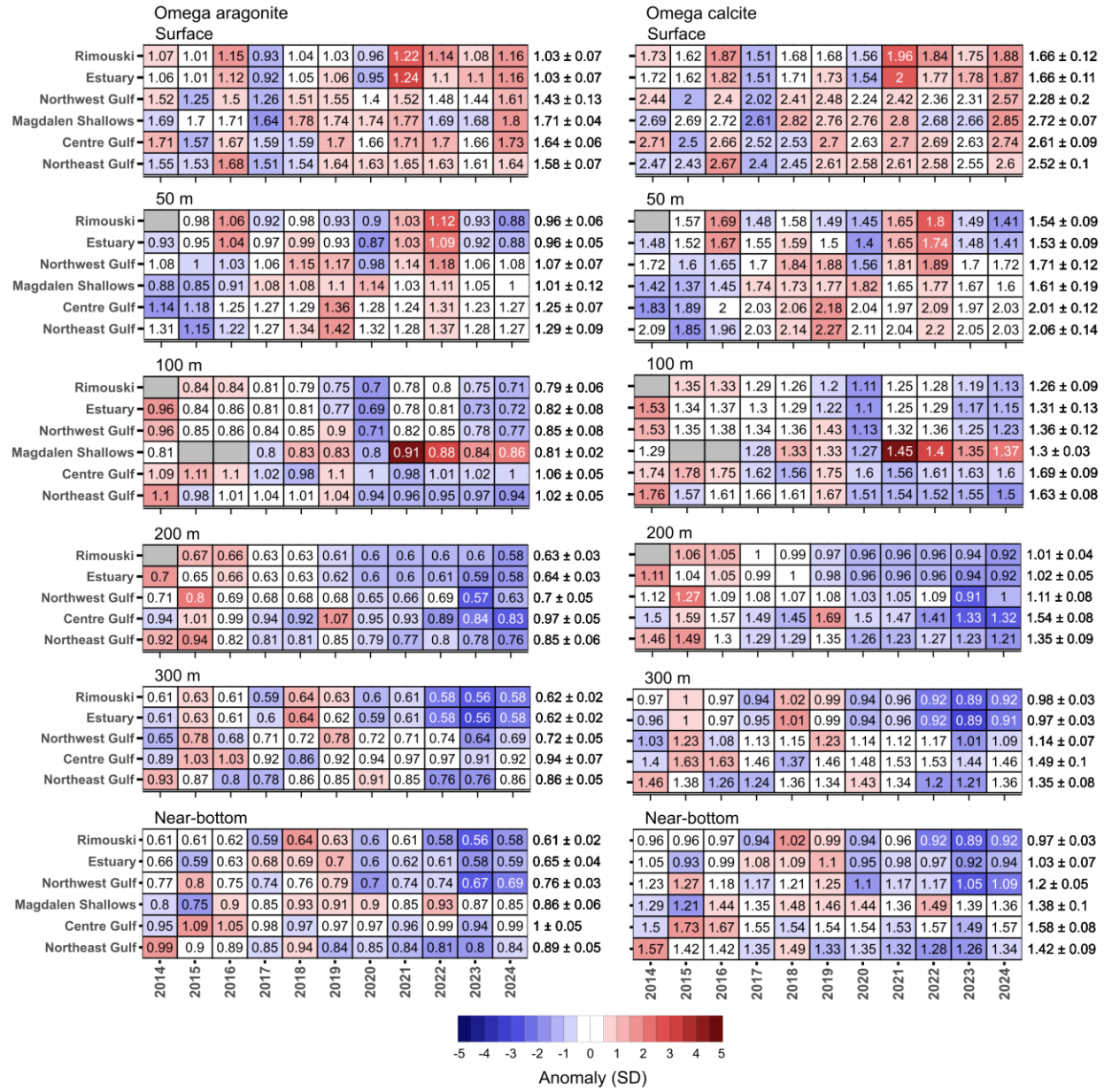

Figure 19 : Time series of annual anomalies in omega aragonite (Ω_A; unitless; left panel), and omega calcite (Ω_C; unitless; right panel), and from 2014 to 2024, calculated at six depths: surface, 50 m, 100 m, 200 m, 300 m, and bottom. The boxed values indicate annual Ω_A or Ω_C averages, while the numbers aligned on the right represent the climatological means and standard deviations (SD) calculated over the period 2014–2020. Cell colors convey the direction and magnitude of anomalies: white cells indicate values within ± ½ SD of the climatological mean, red cells denote above-normal anomalies, and blue cells reflect below-normal anomalies. Grey cells mark insufficient or missing data. To enhance legibility, white text is used within cells where anomalies exceed ± 2 SD.

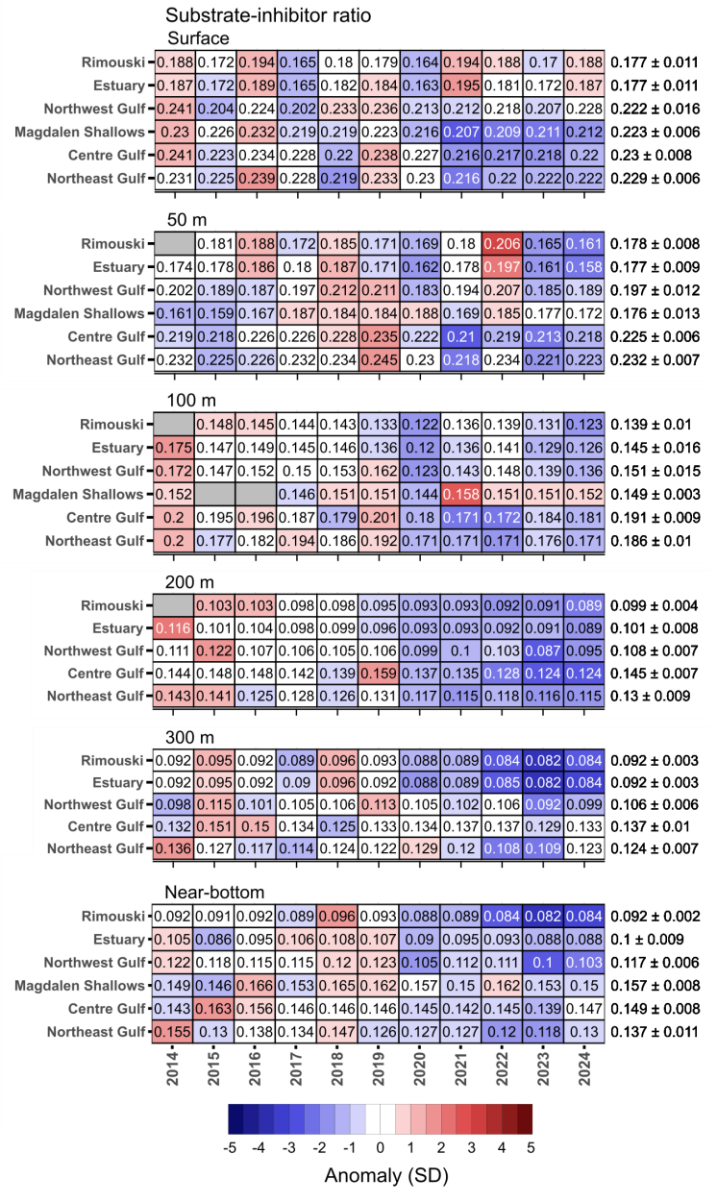

Figure 20 : Time series of annual anomalies in the substrate-inhibitor ratio (SIR; expressed in mol µmol^{-1}) from 2014 to 2024, calculated at six depths: surface, 50 m, 100 m, 200 m, 300 m, and bottom. The boxed values indicate annual SIR averages, while the numbers aligned on the right represent the climatological means and standard deviations (SD) calculated over the period 2014–2020. Cell colors convey the direction and magnitude of anomalies: white cells indicate values within ± ½ SD of the climatological mean, red cells denote above-normal anomalies, and blue cells reflect below-normal anomalies. Grey cells mark insufficient or missing data. To enhance legibility, white text is used within cells where anomalies exceed ± 2 SD.

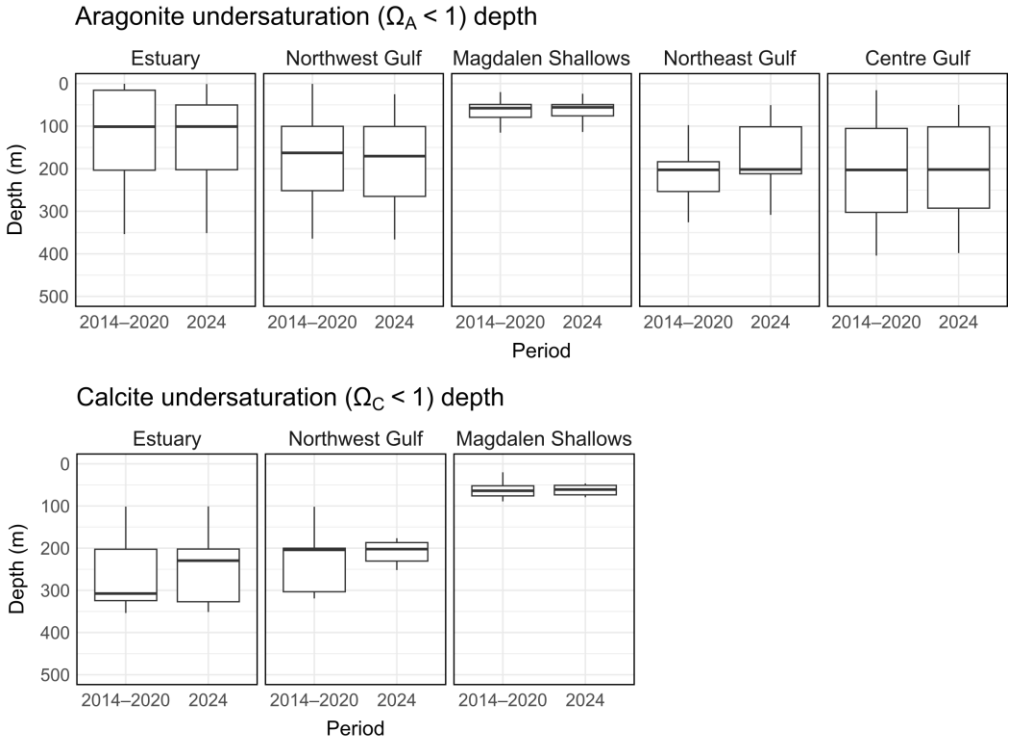

Figure 21 : Boxplots of aragonite undersaturation (Ω_A < 1; top panels) and calcite undersaturation (Ω_C < 1; bottom panels) depth distribution in the EGSL regions for the reference period (2014–2020) and the year 2024. The median (bold horizontal line) represents the central value of the data, indicating the depth at which half of the observations are shallower and half are deeper. The interquartile range (IQR, box) spans from the first quartile (25th percentile) to the third quartile (75th percentile). The whiskers (lines protruding from the box) extend to the lowest and highest values within 1.5 times the IQR from the first and third quartiles, respectively. Outliers that fall outside the range of whiskers are not shown in this plot.

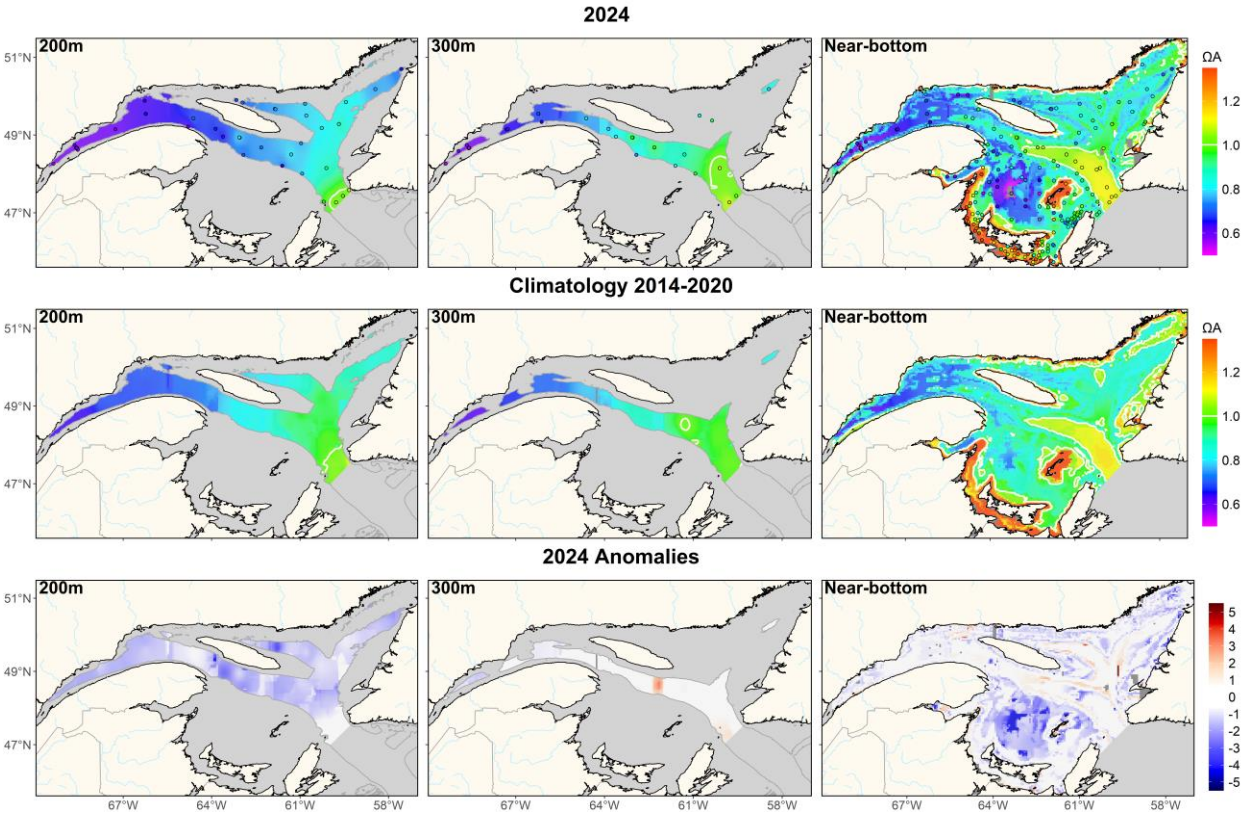

Figure 22 : Annual average distribution of the saturation state of aragonite (Ω_A; unitless) at depths of 200 m and 300 m, and at the bottom in the Estuary and Gulf of St. Lawrence during 2024 (upper panels). The climatology (2014–2020; middle panels) and anomalies (lower panels) are also shown. In the bottom panels, anomaly colors convey both the direction and magnitude of deviations: white indicates normal values within ± ½ standard deviation (SD) of the climatological mean, red denotes above-normal anomalies, and blue reflects below-normal anomalies. The white contour line identifies a threshold of 1. Open circles (upper panels) show station locations in 2024.

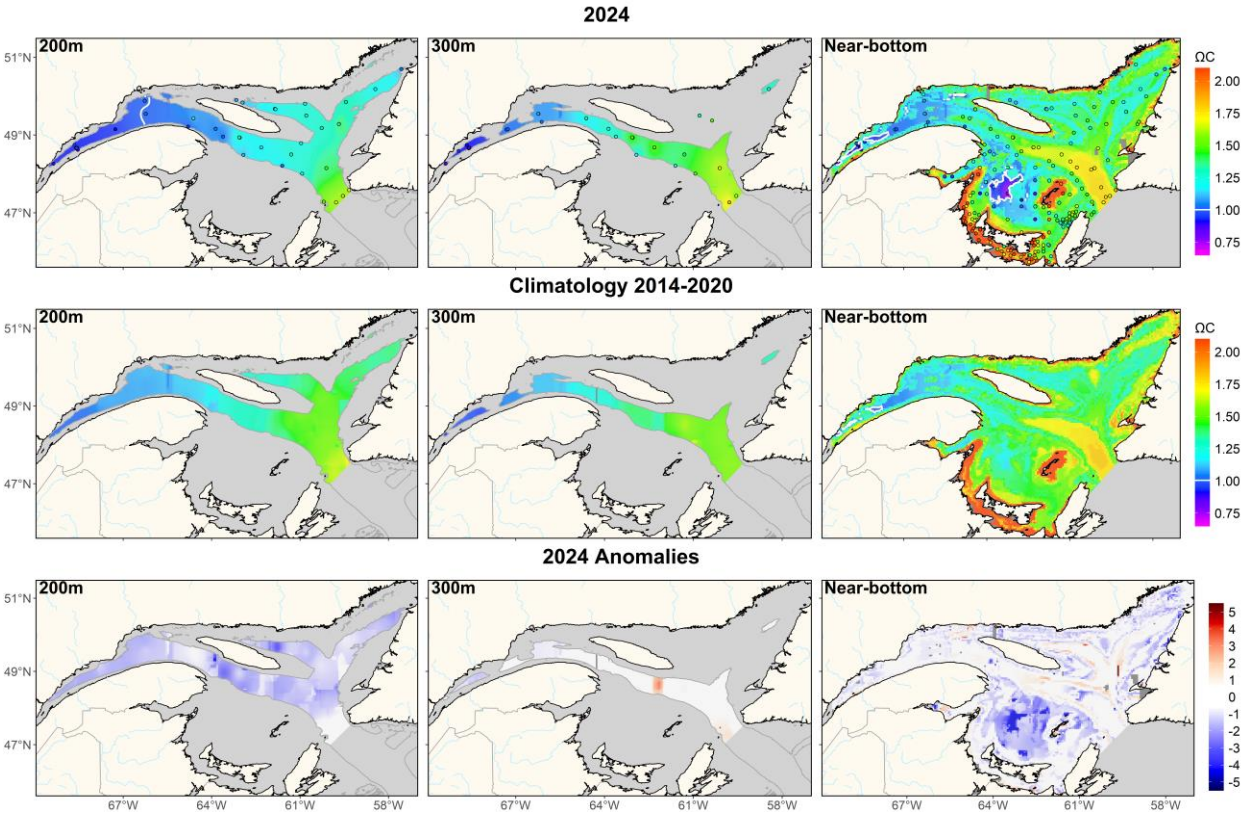

Figure 23 : Annual average distribution of the saturation state of calcite (Ω_C; unitless) at depths of 200 m and 300 m, and at the bottom in the Estuary and Gulf of St. Lawrence during 2024 (upper panel). The climatology (2014–2020; middle panel) and anomalies (lower panel) are also shown. In the bottom panels, anomaly colors convey both the direction and magnitude of deviations: white indicates normal values within ± ½ standard deviation (SD) of the climatological mean, red denotes above-normal anomalies, and blue reflects below-normal anomalies. The white contour line identifies a threshold of 1. Open circles (upper panel) show station locations in 2024.

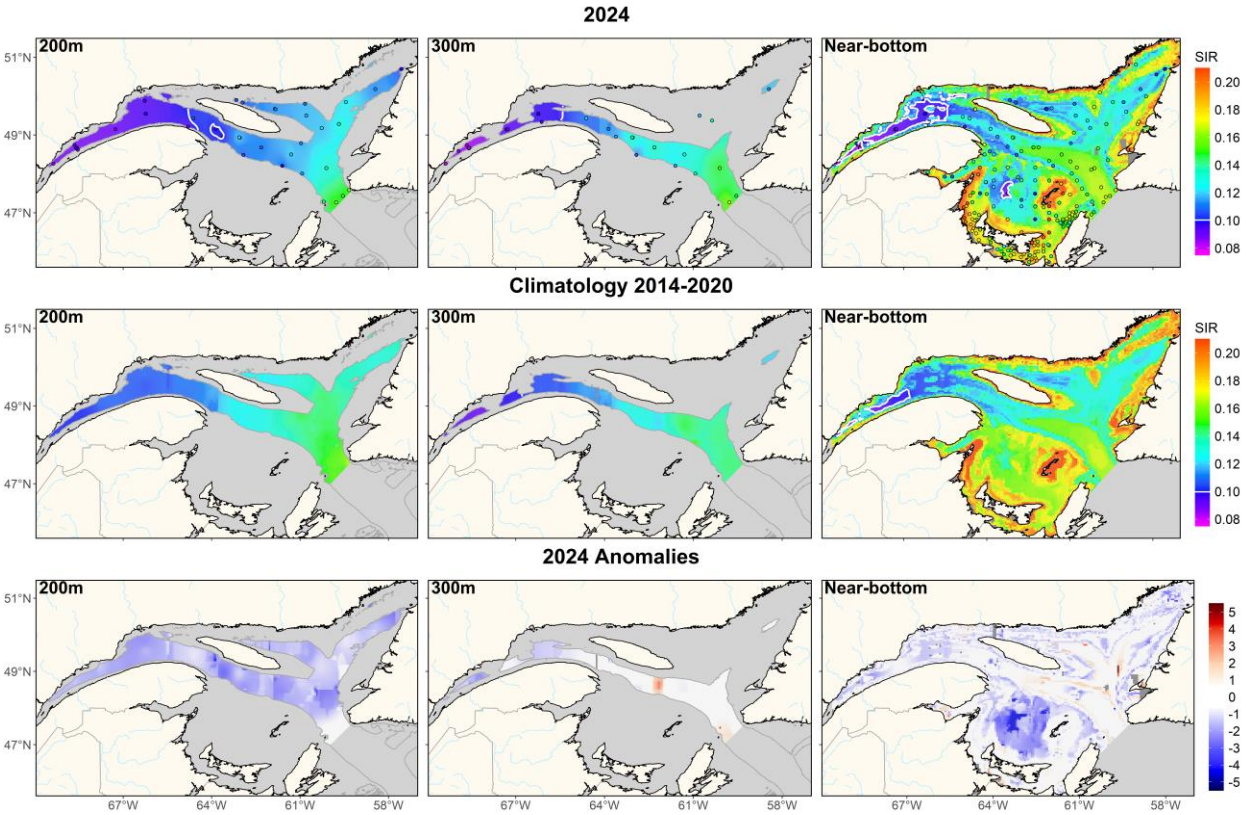

Figure 24 : Annual average distribution of the substrate-inhibitor ratio (SIR in mol µmol^{-1}) at depths of 200 m and 300 m, and at the bottom in the Estuary and Gulf of St. Lawrence during 2024 (upper panel). The climatology (2014–2020; middle panel) and anomalies (lower panel) are also shown. In the bottom panels, anomaly colors convey both the direction and magnitude of deviations: white indicates normal values within ± ½ standard deviation (SD) of the climatological mean, red denotes above-normal anomalies, and blue reflects below-normal anomalies. The white contour line identifies a threshold of 0.100. Open circles (upper panel) show station locations in 2024.

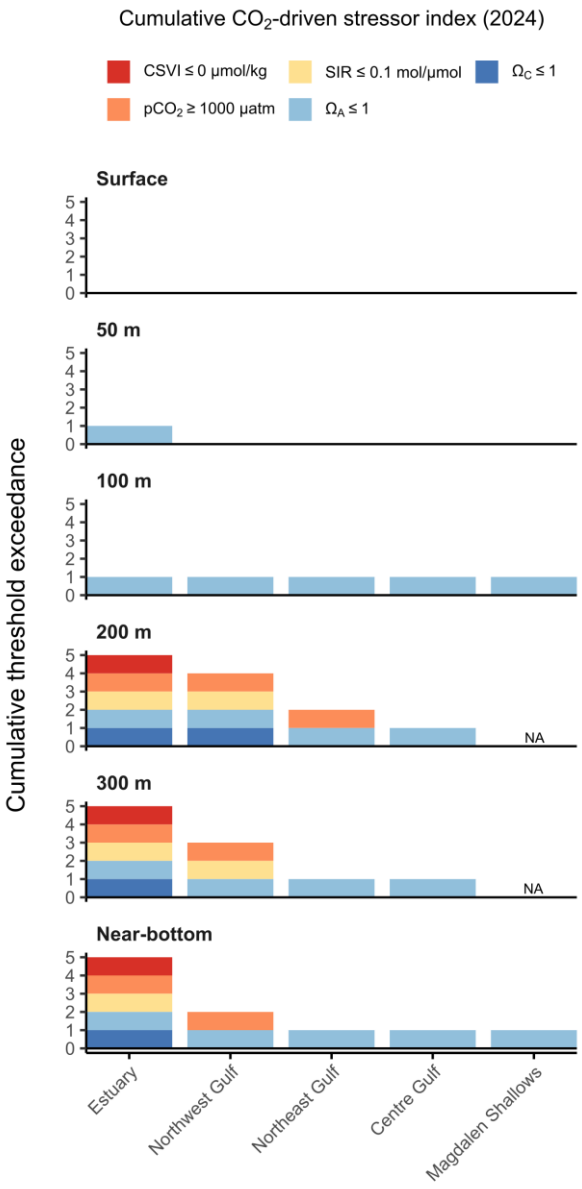

Figure 25 : Cumulative CO_2-driven stressor index for 2024, showing threshold exceedance across five variables at multiple depths and EGSL regions. Bars represent the number of stressors exceeding defined thresholds at each depth, based on annual averages. “NA” marks depths that are not present in the Magdalen Shallows.
CSVI = carbonate system vulnerability index, pCO_2 = partial pressure of CO_2, SIR = substrate-inhibitor ratio, Ω_A = saturation state of aragonite, and Ω_C = saturation state of calcite.

APPENDICES

Appendix 1: General linear model results for Rimouski Station. The significance of the year and month effects as well as the adjusted coefficients of determination (R^2) of the regression for carbonate system metrics are presented.

Station	**Index**	**Year (*p*)**	**Month (*p*)**	**R^2**
Rimouski	TA	0.023	<0.0001	0.47
	DIC	0.037	<0.0001	0.49
	CSVI	<0.0001	0.001	0.55
	pH_T	0.064	0.002	0.32
	pCO_2	0.012	0.002	0.42
	Ω_A	<0.0001	<0.0001	0.62
	Ω_C	<0.0001	<0.0001	0.59
	SIR	0.013	0.003	0.35

Appendix 2: General linear model results for EGSL regions. The significance of the year, season, and station effects as well as the adjusted coefficients of determination (R^2) of the regression for carbonate system metrics are presented.

Region	Index	Year (*p*)	Season (*p*)	Station (*p*)	R^2
Estuary	TA	0.058	<0.0001	0.095	0.29
	DIC	0.017	<0.0001	0.086	0.25
	CSVI	<0.0001	0.001	0.085	0.44
	pH_T	0.019	0.002	0.067	0.18
	pCO_2	0.047	0.002	0.082	0.16
	Ω_A	<0.0001	<0.0001	0.087	0.51
	Ω_C	<0.0001	<0.0001	0.099	0.48
	SIR	0.001	0.002	0.032	0.23
Northwest Gulf	TA	0.049	0.06	<0.0001	0.3
	DIC	0.059	0.011	<0.0001	0.24
	CSVI	0.076	0.029	<0.0001	0.2
	pH_T	0.014	<0.0001	<0.0001	0.35
	pCO_2	0.018	<0.0001	<0.0001	0.37
	Ω_A	0.063	0.006	0.015	0.17
	Ω_C	0.07	0.005	0.013	0.17
	SIR	0.057	<0.0001	<0.0001	0.32
Centre Gulf	TA	0.014	0.014	0.071	0.15
	DIC	0.047	0.007	0.1	0.14
	CSVI	0.086	0.012	<0.0001	0.25
	pH_T	0.09	0.026	0.097	0.1
	pCO_2	0.091	0.038	0.099	0.1
	Ω_A	0.077	0.018	0.012	0.15
	Ω_C	0.079	0.017	0.016	0.14
	SIR	0.078	0.005	0.076	0.14
Northeast Gulf	TA	0.032	0.093	<0.0001	0.22
	DIC	0.081	0.041	0.015	0.13
	CSVI	0.093	0.027	0.007	0.15
	pH_T	0.085	0.086	0.018	0.11
	pCO_2	0.085	0.087	0.016	0.12
	Ω_A	0.098	0.058	0.034	0.11
	Ω_C	0.098	0.055	0.034	0.11
	SIR	0.075	0.04	0.024	0.12
Magdalen Shallows	TA	0.045	0.019	0.046	0.13
	DIC	0.082	0.029	0.07	0.11
	CSVI	0.027	<0.0001	0.09	0.32
	pH_T	<0.0001	<0.0001	0.01	0.68
	pCO_2	<0.0001	<0.0001	0.009	0.71
	Ω_A	0.001	<0.0001	0.008	0.39
	Ω_C	0.058	<0.0001	0.1	0.29
	SIR	<0.0001	<0.0001	0.099	0.67

Appendix 3: List of acronyms used in this report.

Acronym	Word or series of words
ACCASP	Aquatic Climate Change Adaptation Services Program
AZMP	Atlantic Zone Monitoring Program
Ca^{2+}	Calcium ion
$CaCO_3$	Calcium carbonate
CIL	Cold Intermediate Layer
CO_2	Carbon dioxide
CO_3^{2-}	Carbonate ion
CSVI	Carbonate system vulnerability index
CTD	Conductivity-Temperature-Depth
DFO	Department of Fisheries and Oceans Canada
DIC	Dissolved inorganic carbon
DOM	Dissolved organic matter
EGSL	Estuary and Gulf of St. Lawrence
GLM	General linear model
H^+	Hydrogen ion
H_2CO_3	Carbonic acid
HCO_3^-	Bicarbonate ion
IQR	Interquartile range
LCW	Labrador Current waters
Mg	Magnesium
NACW	North Atlantic Central waters
OA	Ocean acidification
pCO_2	Partial pressure of carbon dioxide
pH	Potential of hydrogen
pH_T	Potential of hydrogen on the total scale
SD	Standard deviation
SIR	Substrate-inhibitor ratio
TA	Total alkalinity
TRIS	Tris(hydroxymethyl)aminomethane
Ω_A	Saturation state of aragonite
Ω_C	Saturation state of calcite